Modeling and Control of Capacitive Wireless Power Transfer Systems

Thesis submitted in partial fulfillment

of the requirements for the degree of

"DOCTOR OF PHILOSOPHY"

By

Eli Abramov

Submitted to the Senate of Ben-Gurion University

of the Negev

15.08.2021

Beer-Sheva

Modeling and Control of Capacitive Wireless Power Transfer Systems

Thesis submitted in partial fulfillment

of the requirements for the degree of

"DOCTOR OF PHILOSOPHY"

By

Eli Abramov

Submitted to the Senate of Ben-Gurion University

of the Negev

Approved by the advisor:
Prof. Mor Mordechai Peretz 

Approved by the Dean of the Kreitman School of Advanced Graduate Studies:
Prof. Dudy Bar-Zvi

15.08.2021

Beer-Sheva

This research was carried out under the supervision of:

Prof. Mor Mordechai Peretz

The Center of Power Electronics and Mixed-Signal IC (PEMIC)

Department of Electrical and Computer Engineering

Faculty of Engineering.

Research-Student's Affidavit when Submitting the Doctoral Thesis for Judgment

I___Eli Abramov_____, whose signature appears below, hereby declare that

(Please mark the appropriate statements):

_✓_ I have written this Thesis by myself, except for the help and guidance offered by my Thesis Advisors.

_✓_ The scientific materials included in this Thesis are products of my own research, culled from the period during which I was a research student.

___ This Thesis incorporates research materials produced in cooperation with others, excluding the technical help commonly received during experimental work. Therefore, I am attaching another affidavit stating the contributions made by myself and the other participants in this research, which has been approved by them and submitted with their approval.

Date: ___15.08.2021____ Student's name: ___Eli Abramov___

Signature: 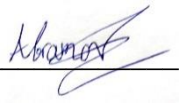

Acknowledgements

Life is full of journeys, and over the last 12 years in academia, I went through a challenging, meaningful, and satisfying journey. The knowledge, skills, and most importantly, the friendships I gained over my academic years are priceless.

First and foremost, I would like to express my sincere gratitude to my supervisor for the last 7 years, ***Prof. Mor Mordechai Peretz***. Thank you for giving me the opportunity to learn from you and work with you. Thank you for being the role model I needed to excel and succeed in my academic and personal life. Thank you for being a supportive tutor, true friend, and great partner. Your invaluable insights and advice will remain with me for all my years.

I would also like to thank to Dr. Alon Cervera, my colleague, partner, and a dear friend. We have traveled a long way together, full of great achievements through mutual support, respect, and a lot of patience. Thank you for helping me to improve in many aspects. Further, I would like to thank Dr. Ilya Zeltser for his advice, ideas, collaboration, and participation in my research throughout my PhD studies.

Many thanks to the PEMIC staff, Dr. Michael Evzelman and Mr. Azrikam Yehieli, who are responsible for the excellent work and social conditions at PEMIC. I have learned many practices from each of you, which I am taking with me today. And I must not forget my colleagues: Mr. Yevgeny Lazarev, Mr. Or Kirshenboim, Mr. Tom Urkin, Mr. Bar Halivli, Mr. Guy Sovik, Mr. Erez Sarig, Mr. Doodi Dayan, Mr. Yotam Schultz, Mr. Erzol Masnandilov, Mrs. Hagit Perets Habany, and Mr. Ron Vaizman.

Most importantly, I thank my dear wife, Natasha♥, for her tremendous loving support, patience, and care. Last, but not least, I would like to express my profound gratitude to my parents and brothers, who have always supported and believed in me along this wonderful journey.

Many thanks,

Eli Abramov

Abstract

Over the last decade, wireless power transfer (WPT) technology has been investigated at a much faster pace, developing it to the point where it can be integrated into various appliances from milliwatts to kilowatts such as: biomedical systems, portable electronics, in-track moving systems, LED drivers, electric vehicles, and many more. WPT is the main enabler that reduces the significant dependency of volume-sensitive portable applications on embedded bulky batteries as a reliable main source of energy.

In the context of near-field WPT methods, magnetic-based approaches such as inductive power transfer (IPT) and magnetic resonance have been well studied over the years. IPT is a well-known method, and it is the most adopted technique in commercial WPT applications due to its simplicity, reliability, and safety. Significant research advancements as well as some commercial trials have been pursued with IPT, reporting efficient transfer of a few kilowatts for static applications. However, magnetic-based WPT systems tend to be complex due to bulky magnetic elements. In addition, the sensitivity to metal debris within the medium and losses associated with metals nearby the system limit the robustness in performance that can be achieved.

An alternative near-field method is capacitive power transfer (CPT), which typically utilizes high-frequency resonant electric fields to transfer energy. One of the more attractive advantages of capacitive WPT is the avoidance of undesired eddy currents and electromagnetic interfaces (EMI) that come with magnetic-based WPT methods. In addition to efficiency improvements, CPT technology offers low-cost, low-weight, and simpler end-to-end system construction. This makes CPT technology an attractive candidate for various applications.

The main challenge of general near-field WPT systems, and in a capacitive approach, in particular, is that the power transfer capability and efficiency depend on the distance and alignment between the transmitting and receiving sides. In addition, the coupling coefficient of the transfer medium and load conditions are sensitive to changes in the environment, component aging, and temperature drifts, which drastically decrease the power transfer capabilities of the system. These introduce some practical limitations on dynamic wireless power applications.

The objective of this PhD research was to provide and detail a framework for wireless CPT systems, which provides the knowledge and tools to analyze the cross-coupling relationship between the input and output parameters, and enables changes to be accounted for in the coupling medium, resonant frequency and reactive components. This knowledge is then translated into design guidelines for efficient multi-loop control algorithms and analysis dedicated for general near-field WPT systems, and for wireless CPT technology in particular. A further objective of this research was to design and develop a high-performance controller on-chip for RWPT.

The outcome of this research was published in four papers [1]-[4] in *IEEE Transactions on Power Electronics* (TPEL), the *Journal of Emerging and Selected Topics in Power Electronics* (JESTPE), and *IET Power Electronics*. In addition, seven leading conference papers [5]-[11] were presented at the IEEE Applied Power Electronics Conference (APEC) and at the Control and Modeling for Power Electronics (COMPEL).

***Keywords**:* behavioral modeling, capacitive power transfer, control for wireless power systems, controller IC, digital control, wireless power transfer

Table of Contents

List of Figures

List of Tables

Acronyms and Abbreviations

ADC – Analog to digital converter
ARMA – Auto-regressive moving average
ASIC – Application specific integrated circuit
CC – Capacitive coupler
CPT – Capacitive power transfer
DCO – Digital controlled oscillator
DL – Delay line
DPLL – Digital phase locked loop
DPWM – Digital pulse width modulation
EMI – electromagnetic interference
FEA – Finite element analysis
HR – High resolution
IC – Integrated circuit
IoT – internet of things
IPT – Inductive power transfer
LCO – Limit-cycle oscillations
PVT – Process, voltage, and temperature
OCP – Over current protection
OVP – Over voltage protection
RWPT – Resonant wireless power transfer
SPI – Serial communication unit
SD-ADC – Sigma-delta analog to digital converter
TDC – Time to digital conversion
WPT – Wireless power transfer
ZVS – Zero voltage switching

Inline References Legend

X.XX – Chapter / Section number
(X.XX) – Equation
[XX] – Reference
Fig. X.XX – Figure

CHAPTER 1: Introduction

1.1 Wireless Power Transfer

Energy transfer is the primary factor that determines the connectivity type of a wide range of electronic equipment, starting from a fraction of a watt to several kilowatts. Although many features have been enabled by wireless media (such as broadband communication, data and signal transfer, and user interfaces), many applications still require a plug-in cable to sustain their energy status. The primary reason is the lack of an efficient and safe method that is comparable to, or better than, corded transfer of electrical energy.

The idea of wireless power transfer has been around since the inception of electricity. In the late 19th century, Nikola Tesla described the freedom to transfer energy between two points without the need for a physical connection to a power source [12]. A truly wireless device, i.e., with 3-dimensional movement and capable of being remotely powered, not only allows obvious freedom of movement, but also enables devices to be more compact by removing the necessity of a large battery. Wireless power technology is evolving rapidly, with an increasing number of applications that have reach the market in the last few years [13]-[22]. The growth in mobile computing has led to slimmer and more stylish and compact devices without connectors. Most of the data transfer in mobile devices is done wirelessly through Wi-Fi and mobile data networks. It is only natural to eliminate the bulky cords needed to power these devices to make them truly wireless.

Although wired power delivery is less expensive and can be used at any power level, the use of cables always requires human intervention to plug and unplug them. At higher power levels, cables/power cords are heavy and expensive. Another problem with them is that they can be damaged by manhandling, tripping, etc. The possibility of an electrical hazard caused due to rain, snow, or humidity is eminent. Therefore, wireless power transfer is a major enabler to transfer electric power to an appliance without the use of power cords. With the advent of more pervasive mobile computing technologies, the need to keep these power-hungry devices charged without wires has initiated the next wave of innovation in wireless power transfer. Wireless power can be very beneficial in a variety of fields such as: the internet of things (IoT), consumer electronics, electric vehicles, smart mobility, home appliances, and more.

1.2 Near-Field WPT Methods

For better understanding of the power levels, efficiency, and application constraints of existing technologies, this section briefly surveys several methods of WPT. Wireless power technologies can be classified into two main categories: near-field and far-field. Far-field is employed by RF or laser beams. Typically, such approaches are used to transmit lower power [23]. On the other hand, near-field WPT can be employed by a magnetic field using simple inductive coupling or by resonant-operating inductive coupling, which is also known as magnetic resonance. CPT which is based on electric fields has been investigated in recent years as an alternative near-field power transfer method to well-known magnetic field-based approaches. The different categories of WPT systems are summarized in Fig. 1.1 The following subsections survey magnetic and electric field-based approaches.

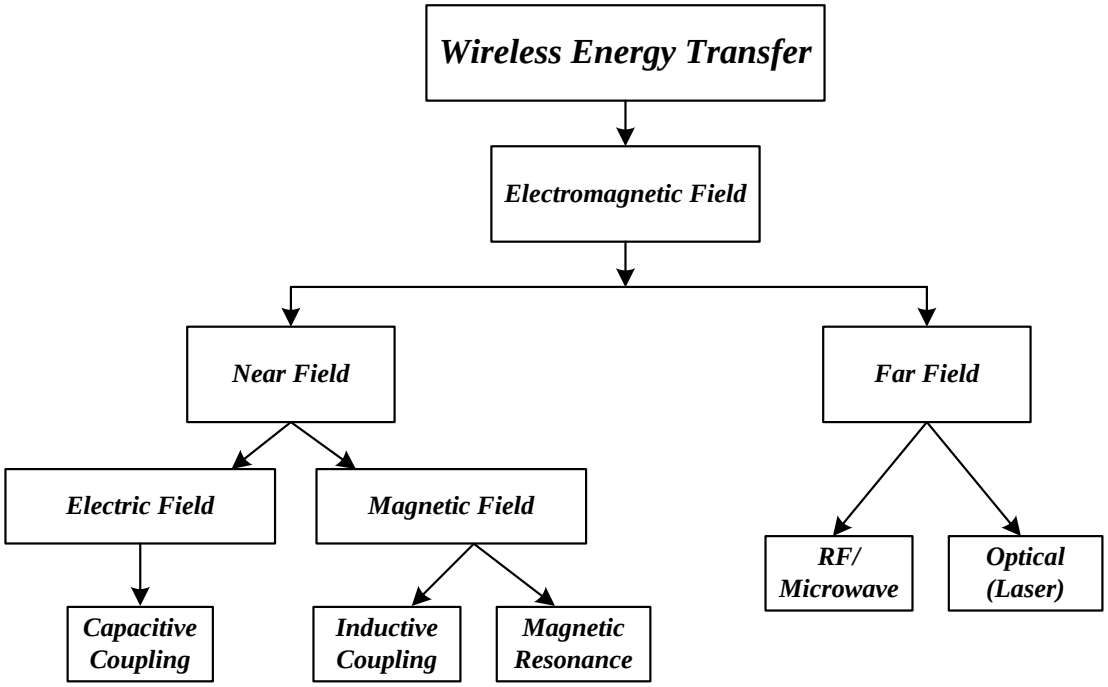

Fig. 1.1 Wireless power transfer classification.

1.2.1 Magnetic-Based WTP

For nearly a century, the conventional practice for WPT was the inductive coupling approach [24]-[37]. Inductive systems are the simplest approach for WPT, and they are used in many fields such as roadway lighting, transportation, consumer electronics, and high-power transmission [28]-[31]. Fig. 1.2 shows the typical structure of an IPT system. Based on the number of turns, *N*, magnetic fluxes are interchanged between the coupling inductors. IPT systems operate on the principle of electromagnetic induction,

thus, their structure can be essentially analyzed as a transformer. A major difference from an ideal transformer, however, is relatively large leakage inductances on both the primary and secondary sides because of magnetically uncoupled inductors

One significant drawback of the IPT is its short transmission distance, since it relies on source-load proximity in order to establish high coupling. Moreover, when the transmitter coil and the receiver coil are not well aligned, the power transfer efficiency significantly drops. Another major issue with the IPT systems is the magnetic field, which may affect any electronics placed in its vicinity, causing electromagnetic interference (EMI) issues. Due to the EMI, the electronics in the environment would require additional shielding and go through rigorous electromagnetic compatibility testing. In addition, the final structure requires large, heavy, and bulky coupling elements. Furthermore, ferromagnetic materials are sensitive to vibrations and to undesirable metal debris in the medium, limiting the system's ability to concentrate the magnetic field [32][33]. Another undesirable phenomenon of the use of a magnetic field is the eddy currents [21],[34], formed by the undesirable metal found in the magnetic field, resulting in significant power loss.

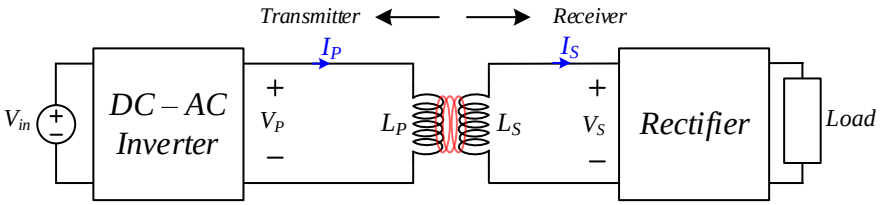

Fig. 1.2 Simplified schematic diagram of an IPT system

Another magnetic-based WPT method is magnetic resonance (Fig. 1.3). This technique uses two or more tuned resonant tanks, resonating at the same frequency to enhance power transfer efficiency and extend transfer range [34]-[45]. Its merit is that high transmission efficiency can be obtained even when the coupling coefficient is low [35]. Typically, magnetic resonance is employed by using a high frequency power supply to pass the change in the high frequency magnetic field from the power transmission coil to the power pick-up coil.

In the magnetic resonance method, maximum transmission efficiency can be obtained when the transmitting coil and receiving coil are placed at an optimum distance from each other. Unlike the IPT method, reducing this distance may cause transmission efficiency to drop instead of increase. This is because when there is a deviation from the optimum distance, the mutual inductance changes, causing the coupling coefficient and the resonance frequency to change. Additionally, the stray

capacitance from objects around the coils also affects the resonance frequency, resulting in an untuned non-optimized system. Thus, this method typically requires more sophisticated control methods to automatically track and tune the circuit for maximum efficiency, which makes this system more complicated than the IPT method. There are various techniques to compensate for the variations in the resonance frequency, but this is the most important design consideration, along with the coil design technology. Although magnetic resonance offers some significant advantages, it still produces undesired EMI and suffers from an efficiency drop due to the losses introduced by the eddy currents [35],[46].

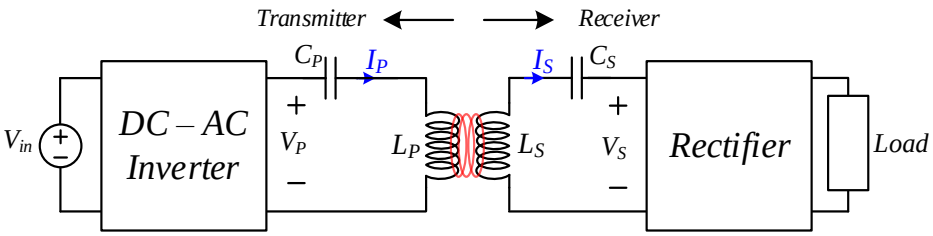

Fig. 1.3 Simplified schematic diagram of a magnetic-resonance WPT system.

1.2.2 Electric-Based WTP

CPT technology is an effective near-field alternative to conventional IPT and magnetic resonance methods [32],[35],[46]-[48]. It utilizes electric fields to transfer electric power, which has several distinguishing advantages: no EMI issues, negligible eddy-current loss, relatively low cost and weight, and reasonable misalignment performance.

The core element of CPT systems is the capacitive coupler (CC), through which energy is transferred by an electric field from the transmitter to the receiver. There are several metal-based geometries used for the CC such as parallel plates, matrix arranged plates, cylindrical, and disk [32],[36]-[39],[46]-[53]. Typically, the CC is formed by a parallel plate configuration which is divided into two types:

1. Unipolar (Fig. 1.4a) – comprises two parallel plates, one for the transmitter and one for the receiver as the power pick-up antenna. The mutual capacitance between the two active plates provides a path for the current to flow toward the load, and a low impedance path between the transmitter and receiver (such as earth ground or another conductive path) is required to allow the current to flow back to the transmitting side. Such a configuration

basically generates an electric field by the coupling of the two sets of asymmetric dipoles.

2. Bipolar (Fig. 1.4b) – the most common configuration to form a CC. The coupler constructed by two pairs of coupling plates creates an equivalent to a two-wire current path, enabling bidirectional current to flow through the coupling element from the transmitter side to the receiver side and vice-versa.

   If an inverter drives the transmitter plates with a 180° phase difference by a high alternating voltage, an alternating electric field is generated in return; thus, power is delivered to the load. Usually, when the plates are well-aligned and the air-gap is small, the main coupling capacitances dominate, and other capacitances can be neglected to simplify the end-to-end system analysis. However, when the plates are misaligned and the air-gap is relatively large, the cross-coupling capacitances become relatively large, and this should be properly considered in system analysis.

It should be noted that different structures of the CC result in different coupling models. The resulting coupling capacitances primarily depend on the plates' area and distance, and the dielectric material between the plates [32],[37],[54]-[56], which in turn are chosen according to the application requirements. In addition, typically, the coupling capacitances in practical applications are usually in the pF range, which requires either multi-MHz operation or high voltages for mid-to-high power levels [32],[36]-[39],[46]-[56]. From safety and electrical standards perspectives, these should be taken into consideration when designing wireless CPT systems.

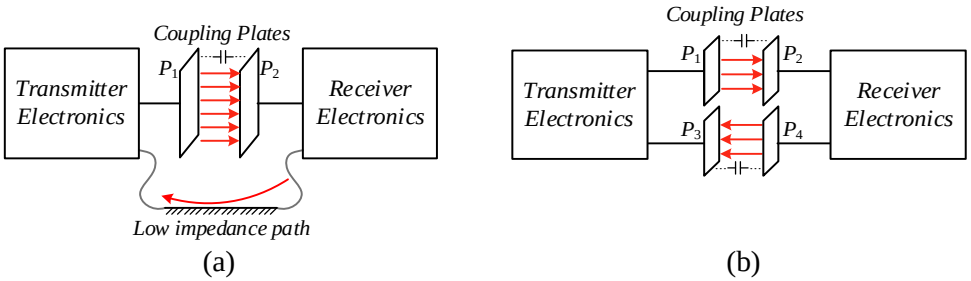

Fig. 1.4 Parallel plate CCs: (a) Unipolar configuration, (b) Bipolar configuration.

A simplified block diagram of a bipolar CPT system is shown in Fig. 1.5. It consists of a power driver that excites resonant operation of a matching network to achieve minimum impedance, i.e., maximum power transfer [57]. Thus, most of the CPT systems utilized are resonant in nature. In the case that the drive frequency is within the

vicinity of the network resonant frequency, the voltage between the plates of the coupling element is virtually sinusoidal [37],[39],[58],[59]. Due to the potential difference, an electrical field is developed between the transmitter side plates, resulting in a potential difference between the plates in the receiver of the coupling device, which in turn powers the receiver side. To provide dc values to the output load, a diode bridge rectifier is used on the receiver side.

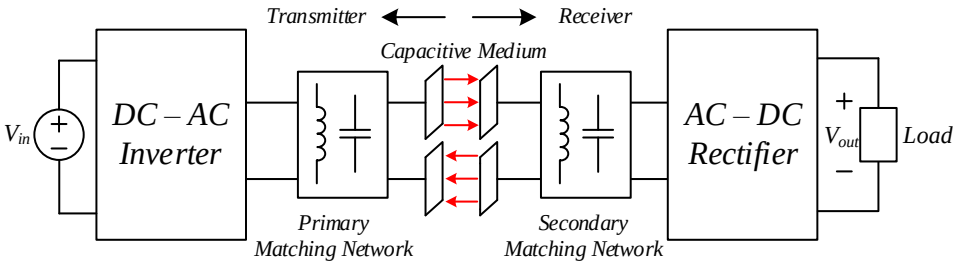

Fig. 1.5 Simplified schematic diagram of a capacitive WPT system.

1.3 Survey of Selected Matching Network Configurations and Their Primary Features

As shown in Fig. 1.5, a fundamental building block of CPT systems is a matching network [57],[60]-[63]. It typically is composed of a second or higher order impedance that connects a sourcing circuit to a loading one. The use of these networks serves many design objectives such as reducing circulating energy in the converter [64], lower voltage and current stresses of the switches [65], assuring soft-switching over a wide range [57], etc. Particularly in WPT systems, matching networks provide additional degrees of freedom to interact between the primary and secondary circuits and to compensate for: resonant frequency, volt-ampere ratings, constant voltage/current output (load-independent operation), output power, and system efficiency [37],[57],[62], [63]. In the following section, some of the basic matching networks are characterized as energy transfer elements.

Fig. 1.6 shows several popular matching networks that are mostly used in capacitive WPT systems [32],[35],[46]-[48]. A well-known and simple option is depicted in Fig. 1.6a in which a series inductance connects to the coupling capacitance of the wireless medium and forms a resonator [32]. By this, operation in the vicinity of the resonant frequency results in an efficient power transfer to the load. However, a significant drawback of this configuration is that even a slight change either in the capacitive medium or the load parameters results in a different operating point and a significant deterioration in the system's ability to transfer power. This is somewhat alleviated by

the configuration in Fig. 1.6b, in which both the primary and secondary sides of the coupling element include series-parallel L-type resonators (also referred as double-sided *LC*). Here, the operating frequency is near the matching network's resonance; therefore, the system is less sensitive to variations in the coupling capacitance (due to distance or misalignment variations). At the cost of a slightly higher component count, the power transfer capabilities are higher than in series compensation, but still depend on the coupling for efficiency and delivered power [37] [48].

The structure in Fig. 1.6c is a combination of the *LC* matching network with an additional series inductor on both sides of the system (double-sided *LCL*). By proper design of the inductors (L_P, L_{P1}, L_S, L_{S1}), this setup provides several degrees of freedom to adjust the power transfer of the system. However, as in the case of the *LC* matching network, the power transfer capabilities of the *LCL* structure are inversely proportional to the coupling capacitance [32],[47]. A more complex matching network is shown in Fig. 1.6d, which consists of a greater number of reactive elements, both primary and secondary (double-sided *LCLC*). There, the coupling capacitance in this case does not directly influence the resonance of the matching networks. However, it still limits the amount of power transfer of the system, i.e., the maximum power that the system is able to transfer is proportional to the coupling capacitance [46].

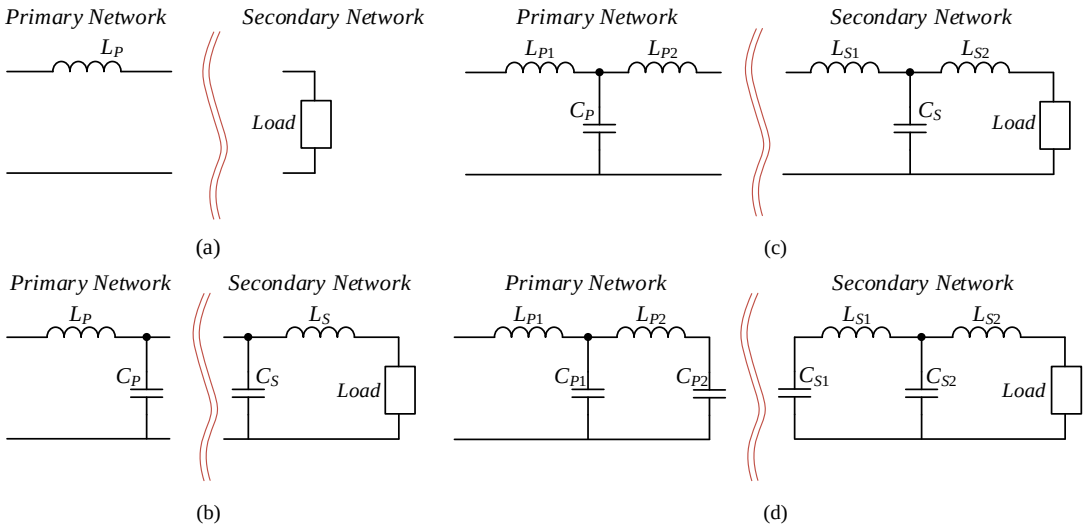

Fig. 1.6 Matching networks for capacitive WPT systems: (a) Series L, (b) Double-sided *LC*, (c) Double-sided *LCL*, (d) Double-sided *LCLC*.

1.4 Challenges in Near-Field WPT Systems

1.4.1 Distance and misalignment variations

The major challenges in any WTP system are the significant variations in the energy transfer capabilities because of orientation changes between the coupling elements of the transmitter and the receiver. Power transfer degradation due to medium changes impacts both electric and magnetic field-based systems [53]-[66]. Placement variations are be divided into two types: distance change between the coupling elements (Fig. 1.7a), and misalignment (Fig. 1.7b).

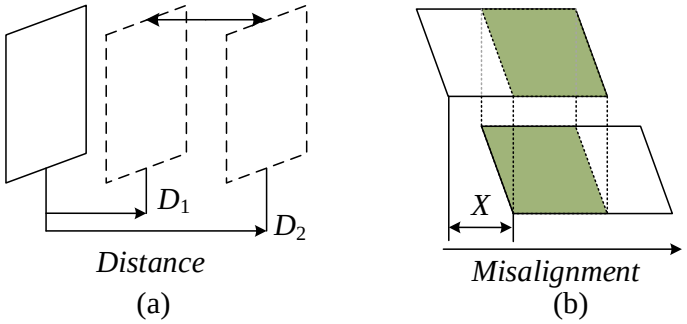

Fig. 1.7 Coupling plate placement challenges: (a) distance changes, (b) non-symmetrical alignment.

Distance changes are the horizontal increase/decrease in the gap between coupling plates along the normal axis of both plates. The plates in this case are in parallel and directed toward one another. In CPT systems, distance changes or misalignment manifests in different effective capacitance between the plates, as illustrated in Fig. 1.8. Either growing distance or non-parallel alignment between the plates lowers the effective area that is coupled, which translates in lower capacitance. It is apparent that a reduction in coupling capacitance between the plates directly affects the amount of potential power that can be transferred to the output (Fig. 1.8b). It should be noted, however, that the variation of the medium capacitance is the core problem (rather than just lower value) which may be manifested by either an increase or decrease in the capacitance value. The reason for this is that in conventional and state-of-the-art practice, the source and load are tuned to a specific medium impedance, and their power transfer capabilities are extremely sensitive to variations in the system parameters.

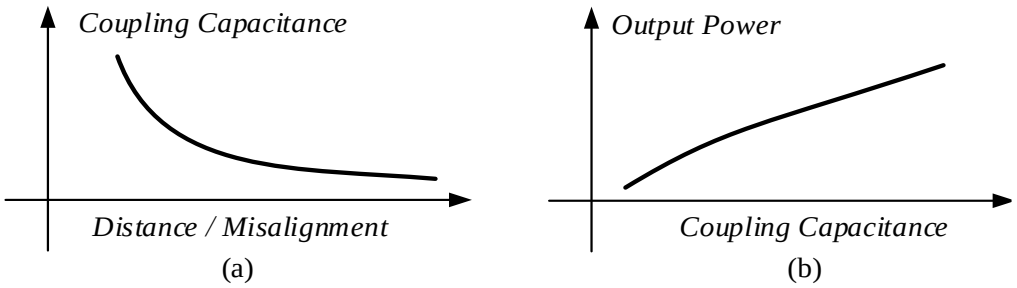

Fig. 1.8 Non-symmetrical alignment and non-idealities of capacitive coupling: (a) distance/ misalignment, (b) output power.

1.4.2 Modeling an end-to-end WPT system

Several explorations and remedies for an extended range power transfer are covered in the literature [58],[60]-[62],[66] for general and CPT systems. An important step in the development of both uniform and specific solutions for extended range WPT systems is a generalized description of the energy transfer mechanism. This requires a description of the transfer medium, circuit behavior, and their interaction. In particular, in the case where active compensation is added, a description of the system's dynamic response is essential. On the topic of magnetic field-based WPT, several models can be found based on circuit and system analyses; however, a generic behavioral model and modeling methodology for CPT has seldom been addressed.

Analysis of such high-order networks can be quite complex and tedious. As a result, the complex interaction between the system parameters and characteristics may be overlooked. Several approaches have been employed to decipher the operation of high-order resonant structures such as analytical multivariable matrix manipulations, geometrical representations [67],[68], and averaging [67]-[70]. Circuit derivation of CPT based on the superposition theorem [48],[71] provides clear closed-form expressions of the power delivery and other important relationships. However, since some approximations are involved, accurate overall description is not always obtained, in particular, for the description of the dynamic characteristics. Numerical simulations are also a strong tool to evaluate and characterize different resonant circuits. This approach, however, loses generality and may be time consuming in cases where a time domain cycle-by-cycle simulation for high-frequency drive signals (several MHz) is carried out [72]-[77]. It would be extremely beneficial if a simple and unified generic averaging behavioral modeling methodology for capacitive-based WPT systems could be utilized, which was one of the goals of this thesis. Furthermore, a practical approach

for describing and evaluating the behavior of CPT systems establishes the core fundamentals for overall closed-loop analysis and controller design for capacitive-based WPT.

1.4.3 Controllers and compensation for CPT

As previously discussed, a main bottleneck of both magnetic and electric WPT methods is that the power transfer capability and efficiency highly depend on the distance and alignment between the transmitter and receiver [35],[47],[48],[78]-[81]. Reducing the sensitivity of the WPT system to variations can be alleviated by designing matching networks that provide loose coupling between the transmitting and receiving sides [37],[46]-[48]. To achieve better power transfer characteristics, resonant high-frequency operation, typically in the range of multi-MHz, is utilized in WPT systems [52] [60]-[63] [66] [78] [82]-[89]. This is essential to compensate for the relatively low coupling of the wireless medium, enhance the transmission range, and achieve reasonable efficiency. In addition to improved spatial freedom, resonant wireless power transfer (RWPT) systems can provide energy to multiple devices with different power requirements simultaneously [43],[90],[91]. Typically, RWPT systems rely on fixed-frequency operation combined with *LC*-based matching networks [37],[44],[57],[63][91],[92]. This alone however, is not sufficient since, in practice, the resonant characteristics are affected by the medium interface (even for loosely coupled systems), changes in environment, component aging, and temperature drifts which dramatically decrease the power transfer capabilities and stability of the system. Adding the fact that, typically, such RWPT systems consist of a high-Q resonator, frequency mismatch results in a large drop in the system's performance [41],[93]. To fully disengage the system's characteristics from any drifts, changes, and variations, multi-loop active compensation is essential.

To address the above issues, new advanced control schemes must be established for CPT systems. However, from a commercialization perspective, capacitive WPT technology is still considered in its infancy stage. To establish best suited control methodologies, CPT topologies also need to be comprehensively studied, modeled, and optimized with respect to system efficiency, power flow, capacitive coupling, and matching networks.

1.5 Thesis Outline

The introduction above provides the background for the following chapters, as well as the motivation for this research. The rest of the chapters detail the following:

Chapter 2 introduces a two-port network-based behavioral modeling approach for resonant-operated capacitive wireless power transfer (WPT) systems. A simple, generic, and unified modeling approach is developed to describe the behavior of WPT systems under changes of the source and load circuits, variations in the coupling interface, and drifts of the components in the matching networks. The resultant model provides insight into the electrical cross-coupling relationships between input and output parameters of capacitive power transfer (CPT) systems, including the effect of distance and alignment of the coupling plates. Regardless of circuit complexity, it is demonstrated that the model core can be reduced to a basic gyrator relationship with added coefficients when required, thus, obtaining a compact, closed-form relationship between the input and output.

Chapter 3 overviews and compares several electrical representations of capacitive couplers (CCs), the wireless power link between the transmitter and receiver, which is a fundamental unit in capacitive power transfer (CPT) systems. To provide a through simulation framework for the CPT, this chapter emphasizes simulation compatibility of the models for static evaluation, as well as for dynamic variations of the medium, which are harder to describe using conventional approaches. Furthermore, implementation techniques in common simulation environments are presented. The models are comprehensively compared, validated, and extended onto particular case studies to highlight the electrical cross-coupling relationships between input and output parameters of the CC.

Chapter 4 details the conditions for soft-switching in capacitively-coupled resonant converters that are compensated with *LCLC* matching networks. The analysis reveals that by designing the compensation networks' parameters according to the highest expected coupling capacitance, zero voltage switching (ZVS) conditions are achieved over the entire operation range. The results of the analysis further outline the way to control the current at switching events so that soft-switching is obtained for all the operating conditions, while the load is resistive on the receiving side. This provides a significant potential enhancement of the power transfer and processing efficiency, in

particular, for applications of wireless energy where the operating frequency is very high.

Chapter 5 introduces an adaptive multi-loop controller for capacitive wireless power transfer (WPT) systems. The new control approach combines continuous frequency tracking and matching network tuning on both the transmitter and receiver to regulate a target current/power to the receiving side at the optimal power transfer conditions. This enables effective disengagement of the power delivery capabilities from the cross-coupling interactions between the transmitting and receiving sides, and compensates for variations in the electrical circuits and capacitive medium. This chapter highlights the complex functional relationships of the multi-mixed signal controller and provides theoretical, as well as practical insights on the dynamics and implementation of a closed-loop capacitive power transfer (CPT) system.

Chapter 6 introduces an adaptive self-tuned controller IC for resonant wireless power transfer (RWPT) systems. The controller IC comprises an on-the-fly very-high frequency tracking hardware with high resolution and an independent high-resolution digital PWM-based (HR-DPWM) current programmed control. These facilitate precise frequency generation, as well as adaptive tuning of the reactive components in the matching network, which translate into tight current/power regulation capabilities, while retaining optimized power transfer conditions on the transmitting side. The controller IC enables effective disengagement of the power delivery capabilities from variations in the resonators, electrical circuits, and wireless medium. The controller core is based on a fully synthesizable digital architecture that has been realized through HDL tools, and several key building blocks have been developed and described in-detail: a delay-line (DL)-based phase detector, high-resolution digital frequency synthesizer, and HR-DPWM. To fully exploit the benefits of digital electronics, reduce power consumption, and save area, the digital core of the controller was designed through asynchronous architecture, eliminating the need for a high-speed clock and its related hardware.

Chapter 7 concludes the thesis.

1.6 Contributions of this Research

Chapter 2 summarizes content that was published in a paper titled “Analysis and behavioral modeling of matching networks for resonant-operating capacitive wireless

power transfer" in *The Institution of Engineering and Technology* (IET Power Electronics, Special Issue: Advanced Technologies Utilized in Wireless Power Transfer Systems) [1], presented at the IEEE Applied Power Electronics Conference (APEC) [6] under the title "Behavioral modeling of resonant power transfer systems with capacitive coupling: two-port network approach", **winning the best presentation award.**

Chapter 3 summarizes content that has been submitted to APEC 2022 under the title "Simulation-compatible capacitive-coupler modeling and analysis for wireless power transfer applications" [7].

Chapter 4 summarizes content that is published in a paper titled "Soft-switching in capacitive-coupled wireless power transfer with *LCLC* compensation networks", presented in APEC [8].

Chapter 5 summarizes content that is published in a paper titled "Multi-loop control for power transfer regulation in capacitive wireless systems by means of variable matching networks" in the *IEEE Journal of Emerging and Selected Topics in Power Electronics* (JESTPE) [3], presented at APEC [9] under the title "Regulated power transfer using self-tuned networks for capacitive wireless systems", **winning the best presentation award.**

Chapter 6 summarizes content that is published in a paper titled "Adaptive self-tuned controller IC for resonant-based wireless power transfer transmitters" in the *IEEE Transactions on Power Electronics* (TPEL) [4], presented at APEC [10] under the title "Adaptive self-tuned mixed-signal controller IC for resonant wireless power transfer".

CHAPTER 2:
Analysis and Behavioral Modeling of Matching Networks for Resonant-Operating Capacitive Wireless Power Transfer

2.1 Introduction

As discussed in Section 1.3, for both magnetic- and electric-field approaches, reactive networks on the transmitting and receiving sides are used for impedance matching between the source and load [57],[60]-[63]. To achieve suitable degrees of freedom in terms of design, performance, and overall input−output relationships in any WPT system, high-order matching networks are used [46],[57],[60]-[63],[94].

This chapter introduces a network-based approach to describe the behavior of capacitive WPT systems that operate in resonant conditions, under variations of the source and load circuits, coupling interface, and matching networks. The modeling methodology results in a compact, closed-form model for CPT that provides insights into the cross-coupling relationship between the input and output parameters and enables to account for changes in the distance and alignment of the coupling plates. A further objective of this chapter is to present a simulation-compatible model of the capacitive coupling by a continuous-time variable capacitor representation. This provides a simulation platform to further analyze and examine wireless CPT.

2.2 Equivalent Two-Port Representations of Matching Networks

Matching L-type structures such as series inductor combined with parallel capacitor (series-parallel *LC*, Fig. 1.6b) and parallel capacitors combined with series inductors (parallel-series *LC*, Fig. 1.6b) can be described as a two-port network with gyrator characteristics [95]. A gyrator is a passive, lossless, linear two-port transformation network in which the output and input currents depend on the input and output voltages, respectively, with respect to its transconductance gain *G*. In circuit theory, gyrators are often used to reflect inductance using capacitance and impedance into admittance, and vice versa [96]-[100]. The input–output relationship of an ideal gyrator as a two-port network can be expressed as:

$$\begin{bmatrix} I_1 \\ I_2 \end{bmatrix} = \begin{bmatrix} 0 & -G \\ G & 0 \end{bmatrix} \begin{bmatrix} V_1 \\ V_2 \end{bmatrix}. \tag{2.1}$$

In the context of the above discussion, voltage and current relationships of a series-parallel *LC* matching structure Fig. 2.1a can be derived as follows:

$$\begin{cases} V_{P1} = j\omega L_P I_{P1} + V_{P2} \\ V_{P2} = \dfrac{1}{j\omega C_P}\left(I_{P1} - I_{P2}\right) \end{cases} \Rightarrow \begin{cases} I_{P1} = \dfrac{\left(V_{P1} - V_{P2}\right)}{j\omega L_P} \\ V_{P1} = j\omega L_P I_{P1} + \dfrac{1}{j\omega C_P}\left(I_{P1} - I_{P2}\right) \end{cases}. \tag{2.2}$$

Assuming operation at the resonant frequency, the currents I_{p1} and I_{p2} are given by:

$$\begin{cases} I_{P1} = -j\omega_0 C_P \left(V_{P1} - V_{P2}\right) \\ I_{P2} = -j\omega_0 C_P V_{P1} \end{cases} \quad ; \quad \omega_0 L_P = \frac{1}{\omega_0 C_P}, \tag{2.3}$$

where ω_0 is the resonant angular frequency.

Employing a few configurational modifications to the L-type network of Fig. 2.1a, an equivalent representation can be obtained. As can be seen in Fig. 2.1b, by the addition of a series resonator (whereas $L_P^* = L_P$ and $C_P^* = C_P$), the network is transformed into a T-type one *(L_P-C_P-L_P^*)*, with an output series capacitance C_P^*. The resultant voltage and current relationships have two-port gyrator characteristics as follows:

$$\begin{aligned} V_{P1} &= j\omega_0 L_P I_{P1} + \frac{1}{j\omega_0 C_P}\left(I_{P1} - I_{P2}\right) = \frac{1}{-j\omega_0 C_P} I_{P2} \\ V_{P2}{}^* &= -j\omega_0 L_P I_{P2} + \frac{1}{j\omega_0 C_P}\left(I_{P1} - I_{P2}\right) = \frac{1}{j\omega_0 C_P} I_{P1} \end{aligned}, \tag{2.4}$$

and in matrix representation, this can be written as:

$$\begin{bmatrix} I_{P1} \\ \\ I_{P2} \end{bmatrix} = \begin{bmatrix} 0 & \underbrace{j\omega_0 C_P}_{-G} \\ \underbrace{-j\omega_0 C_P}_{G} & 0 \end{bmatrix} \begin{bmatrix} V_{P1} \\ \\ V_{P2}{}^* \end{bmatrix}, \tag{2.5}$$

where the transconductance gain is $G = -j\omega_0 C_P$. It should be noted that while assuming operation in resonance, the addition of the series branch is effectively short circuited and does not change the behavior of the circuit.

Following the above observations, the series output capacitance C_P^* can be reflected to an input parallel inductance L_P^*, as shown in Fig. 2.1c. Finally, the original L-type network can be represented as a gyrator element (Fig. 2.1d) with parallel input inductance L_P (full mathematical derivations have been omitted here for clarity and are detailed in Appendix-A).

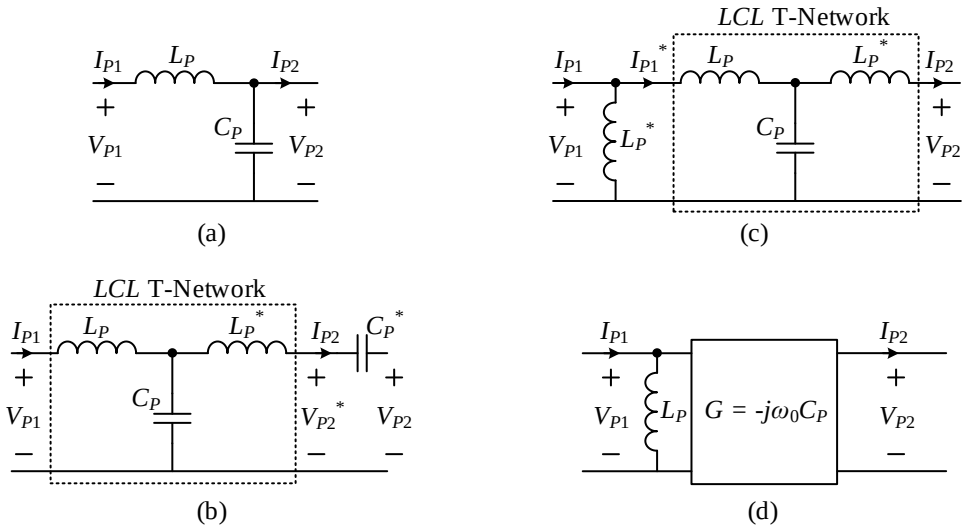

Fig. 2.1 Equivalent representations of series-parallel *LC* matching network: (a) L-type series-parallel resonant *LC* circuit; (b) Series resonator connected to the L-type circuit for T-type network arrangement; (c) Modified T-type series-parallel *LC* resonant circuit; (d) Two-port representation of the original L-type network.

In analogy to the above practice for the series-parallel *LC* matching network, the parallel-series *LC* structure in Fig. 2.2a can also be defined by a gyration ratio. This is facilitated by the addition of a parallel resonator (whereas $L_P^* = L_P$ and $C_P^* = C_P$), as shown in Fig. 2.2b. Similar to the case of the series branch, the parallel resonator is effectively an open circuit when operating at resonance and does not change the original characteristics of the circuit. The L-network is transformed into a π-type one (C_S-L_S-C_S^*) with parallel output inductor L_S^*. The parallel-series *LC* structure can be described as a gyrator element with parallel output inductor L_S, as shown in Fig. 2.2c.

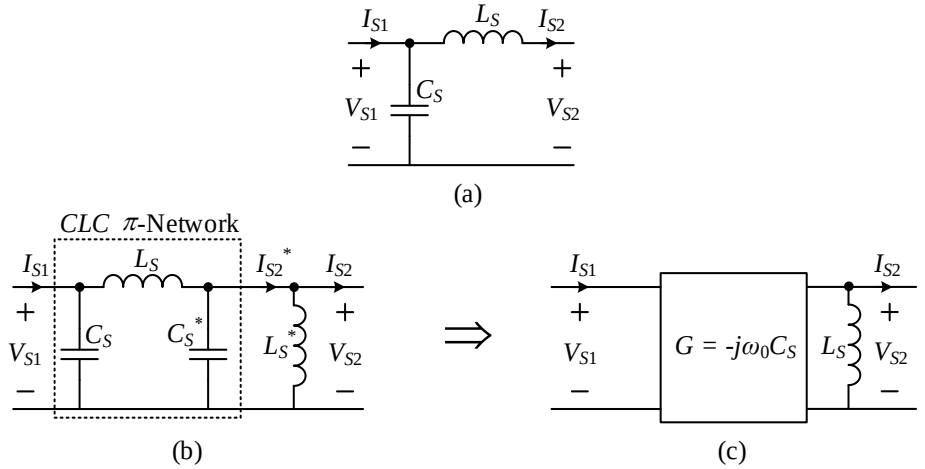

Fig. 2.2 Equivalent representations of parallel-series *LC* matching network: (a) L-type parallel-series resonant *LC* circuit; (b) Parallel resonator connected to the L-type circuit for π-type network arrangement; (c) Two-port network with gyrator characteristics.

A π-type network can also be constructed in an *LCL* configuration, as depicted in Fig. 2.3a. Under resonant operating conditions, the *LCL* π-type configuration is directly

represented as a pure gyrator (Fig. 2.3b). It should be emphasized that for the case of an *LCL* π-type matching network, the transconductance gain *G* is positive, as opposed to the analysis of the circuits in Fig. 2.1 and Fig. 2.2.

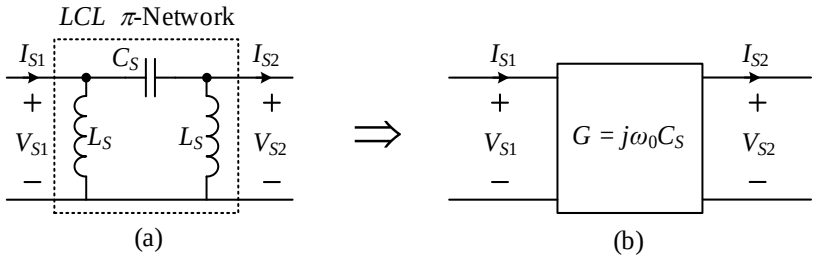

Fig. 2.3 Two-port network: (a) *LCL* π-type, (b) As a gyrator model.

2.3 Case Study: Double-Sided L-Type Capacitive Wireless Power Transfer System

Following the observations and derivations made in the previous section, a capacitively-coupled power transfer system with double-sided L-type matching networks was analyzed. The schematic diagram of the full system is shown in Fig. 2.4. This configuration was selected for the case study demonstration since it can be employed in a variety of medium-power level CPT applications [37],[48]. As can be seen in Fig. 2.4, the matching networks are a series-parallel *LC* circuit at the primary side and a parallel-series *LC* at the secondary side. The capacitive medium is modeled by a π-network, such that C_M is the equivalent mutual capacitance and C_{M1} and C_{M2} are the self-capacitances of the coupling plates [47],[48]. The system is driven by a full-bridge inverter on the primary side, and the load is fed via a diode rectifier that is connected to the secondary's network. Due to the structural constraints of the coupling plates, as a general practice, it is assumed that the coupling capacitance C_M is significantly lower than the total parallel capacitance. Consequently, the driving frequency is near the matching networks' resonant frequency (i.e., $f_0=1/((2\pi(\sqrt{L_P C_P}))$ $=1/((2\pi(\sqrt{L_S C_S}))$. Since high-Q operation is naturally facilitated because of the high output impedance of the primary's network, the currents as well as voltages of the reactive elements are virtually sinusoidal.

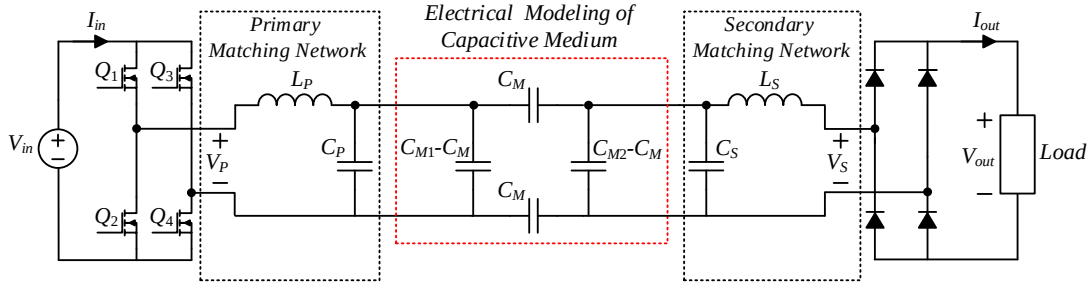

Fig. 2.4 Schematic diagram of a double-sided L-type capacitive WPT system.

For the derivations of the model, the circuit of Fig. 2.4 is simplified by separating the parallel capacitances of the medium from the model self-capacitances, as shown in Fig. 2.5a. This forms a π-network constructed by the mutual capacitance C_M, which can be analyzed similarly to the *LCL* π-matching network from Section 2.2. This enables use of a gyrator element to represent the coupling behavior, as depicted in Fig. 2.5b. In the context of the overall system, Fig. 2.4 is simplified as delineated in Fig. 2.5c. Applying the network dualities that have been established earlier, the entire system is represented by three gyrators connected in series, as shown in Fig. 2.5d, where $C_P^*=C_P+C_{M1}$ and $C_S^*=C_S+C_{M2}$; $C_P, C_S >> C_{M1}, C_{M2}$. This is further reduced to a single gyrator, as illustrated in Fig. 2.5e, with a total transconductance gain that can be expressed as:

$$G_{total} = \frac{j\omega_0 C_P^* C_S^*}{C_M} . \qquad (2.6)$$

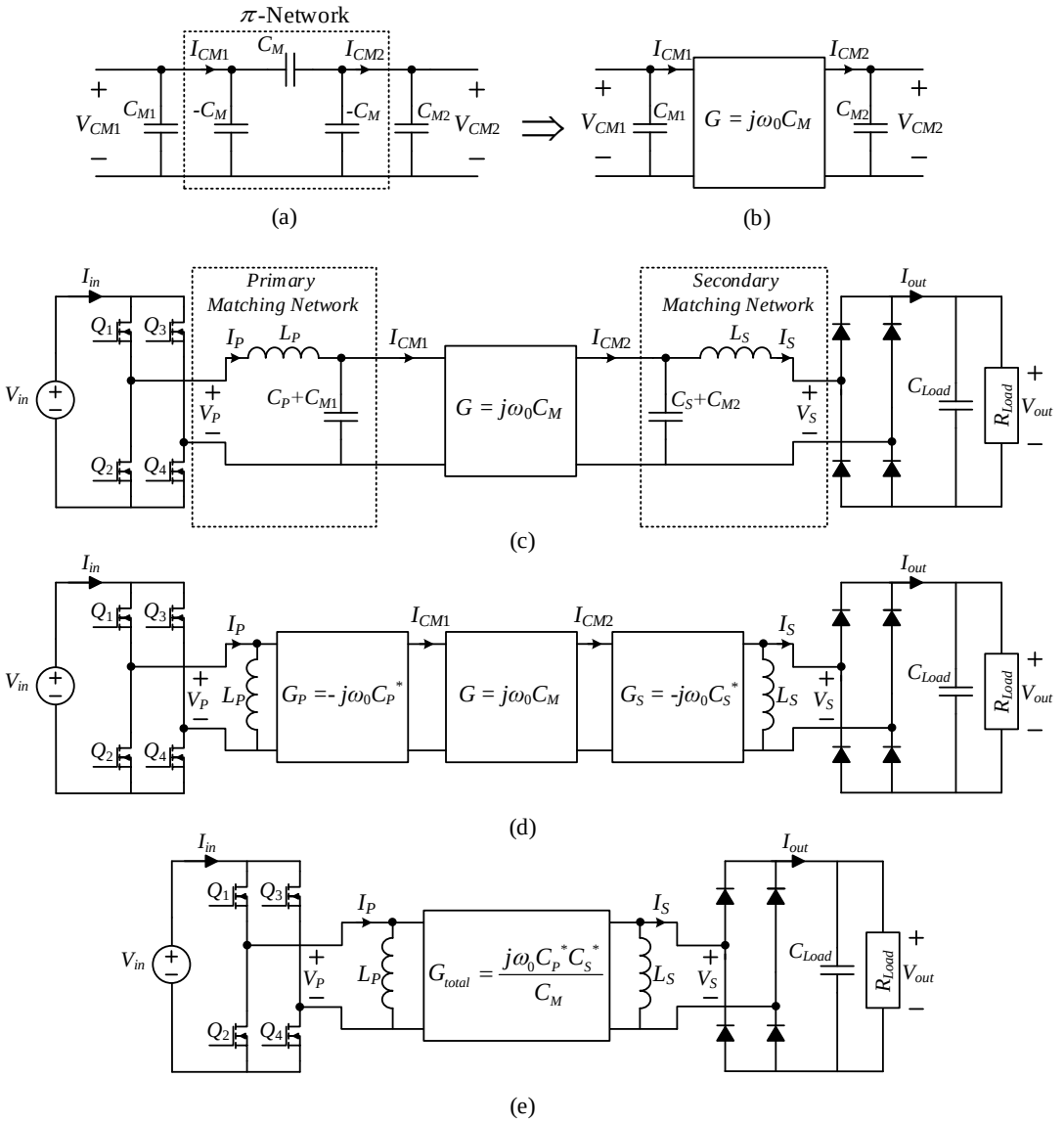

Fig. 2.5 Equivalent two-port network-based models of the capacitive WPT system: (a) Electrical equivalent model of a four-plate capacitive medium; (b) Representation of the capacitive medium with a two-port network; (c) Representation of a double-sided L-type capacitive WPT system with a gyrator as the capacitive medium; (d) Equivalent circuit of a double-sided L-type capacitive WPT system with three series gyrators; (e) Equivalent simplified circuit of a double-sided L-type capacitive WPT system with a single gyrator.

The simplified circuit of the double-sided L-type capacitive WTP system in Fig. 2.5e can now be analyzed as a two-port network with gyrator characteristics, such that the current–voltage relationships are expressed as follows

$$\begin{aligned} I_P &= \frac{V_P}{j\omega_0 L_P} - \frac{j\omega_0 C_P^* C_S^*}{C_M} V_S = -j\left(\frac{V_P}{\omega_0 L_P} + \frac{\omega_0 C_P^* C_S^*}{C_M} V_S\right) \\ I_S &= -\frac{V_S}{j\omega_0 L_S} + \frac{j\omega_0 C_P^* C_S^*}{C_M} V_P = j\left(\frac{V_S}{\omega_0 L_S} + \frac{\omega_0 C_P^* C_S^*}{C_M} V_P\right) \end{aligned} . \tag{2.7}$$

From (2.7), the current–voltage relationships of the system are distinguished for different scenarios of: (a) asymmetrical WPT system with voltage ratings and matching

network components with different values; (b) a system with equal voltage ratings; and (c) a complete symmetrical WPT system.

For an asymmetrical system, i.e., $V_P \neq V_S$, $L_P \neq L_S$ and $C_P^* \neq C_S^*$, the absolute values of current–voltage relationships can be expressed in a matrix representation as follows:

$$\begin{bmatrix} I_P \\ \\ I_S \end{bmatrix} = \begin{bmatrix} \dfrac{1}{\omega_0 L_P} & \dfrac{\omega_0 C_P^* C_S^*}{C_M} \\ \dfrac{\omega_0 C_P^* C_S^*}{C_M} & \dfrac{1}{\omega_0 L_S} \end{bmatrix} \begin{bmatrix} V_P \\ \\ V_S \end{bmatrix}. \tag{2.8}$$

It should be noted that although the passive matching components are different, the resonant frequency is identical for both the primary and secondary sides.

Next, in the case that some symmetry in the form of $V_P = V_S$ is incorporated, however, still with different values for the matching components, then the relationship simplifies to:

$$\begin{bmatrix} I_P \\ \\ I_S \end{bmatrix} = \begin{bmatrix} 0 & \dfrac{1}{\omega_0 L_P} + \dfrac{\omega_0 C_P^* C_S^*}{C_M} \\ \dfrac{1}{\omega_0 L_S} + \dfrac{\omega_0 C_P^* C_S^*}{C_M} & 0 \end{bmatrix} \begin{bmatrix} V_P \\ \\ V_P \end{bmatrix}. \tag{2.9}$$

Finally, in the particular case of a full symmetrical system, i.e., $V_P = V_S$, $L_P = L_S = L$ and $C_P^* = C_S^* = C$, the relationship renders down to a pure gyrator which can be expressed as:

$$\begin{bmatrix} I_P \\ \\ I_S \end{bmatrix} = \begin{bmatrix} 0 & \underbrace{\dfrac{1}{\omega_0 L} + \dfrac{\omega_0 C^2}{C_M}}_{G} \\ \underbrace{\dfrac{1}{\omega_0 L} + \dfrac{\omega_0 C^2}{C_M}}_{G} & 0 \end{bmatrix} \begin{bmatrix} V_P \\ \\ V_S \end{bmatrix}. \tag{2.10}$$

In a typical application of this system, the operating frequency is in the MHz range, the network parallel capacitance values are in the range of hundreds of pFs, inductances are tens to hundreds of µHs, and the mutual coupling capacitance, C_M, is on the order of a few pFs. As a result, the transfer relationship of the system can be simplified to generic expressions as follows:

$$\begin{aligned} I_P &= \frac{\omega_0 C_P^* C_S^*}{C_M} V_S \\ I_S &= \frac{\omega_0 C_P^* C_S^*}{C_M} V_P \end{aligned} \quad ; \quad \begin{cases} \dfrac{\omega_0 C_P^* C_S^*}{C_M} >> \dfrac{1}{\omega_0 L_{P/S}} \\ G \approx G_{total} = \dfrac{\omega_0 C_P^* C_S^*}{C_M} \end{cases}, \tag{2.11}$$

which is in excellent agreement with [47] and [48].

The implication of this analysis is that the double-sided L-type capacitive WPT system can be modeled as a voltage-dependent current source, I_{out}, which represents the rectified current of I_S, as illustrated in Fig. 1.4. Employing the fundamental harmonic approximation [99],[100], the peak values of the currents in (2.11) can be found with the aid of the transconductance gain, and input and output voltages as:

$$I_{P,pk} = \frac{4}{\pi}\frac{\omega_0 C_P^{*} C_S^{*}}{C_M} V_{out}$$
$$I_{S,pk} = \frac{4}{\pi}\frac{\omega_0 C_P^{*} C_S^{*}}{C_M} V_{in} \quad , \tag{2.12}$$

and therefore the average value of the output current $I_{out,AVG}$ is:

$$I_{out,AVG} = \frac{8}{\pi^2}\frac{\omega_0 C_P^{*} C_S^{*}}{C_M} V_{in} \quad . \tag{2.13}$$

It should be noted that not all CPT systems can be simplified into a voltage-dependent current source. However, the presented network-based modeling approach significantly simplifies the input–output relationships of any L-type-based capacitive WPT system by using the gyrator characteristics.

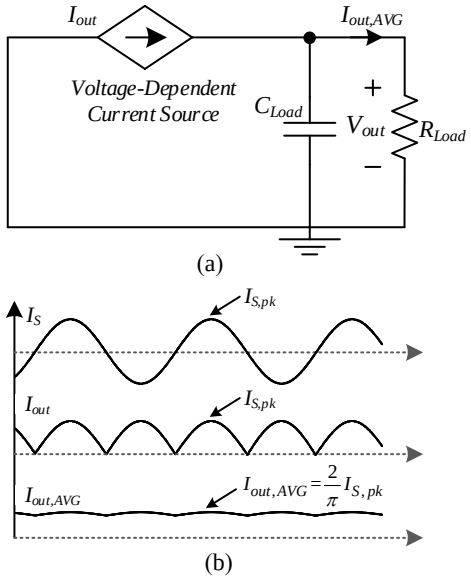

Fig. 2.6 (a) Behavioral model of the analyzed capacitive WPT system for the output side, (b) Secondary side current waveforms.

To verify and show a proof-of-concept of the behavioral model, a cycle-by-cycle simulation test bench for the analyzed CPT system was constructed in PSIM (PowerSim, Inc.). The input voltage was 70 V, and the medium mutual capacitance was C_M =6 pF, at a resonant frequency of $f_0 \approx$1.55 MHz for a load resistance of R_{Load} =15 Ω and output capacitor of C_{Load}=200 pF. The first set of simulations was carried out for

symmetrical matching parameters: L_P=L_S=67 µH, C_P^*≈C_P =C_S^*≈C_S=156 pF. The simulation results of the currents and voltages of the primary and secondary sides are shown in Fig. 2.7, where the dashed lines show the behavioral model predictions. The obtained peak values of the currents are in good agreement with the theoretical predictions in (2.12), which further implies that the average output current, $I_{out,AVG}$, is as expected from (2.13).

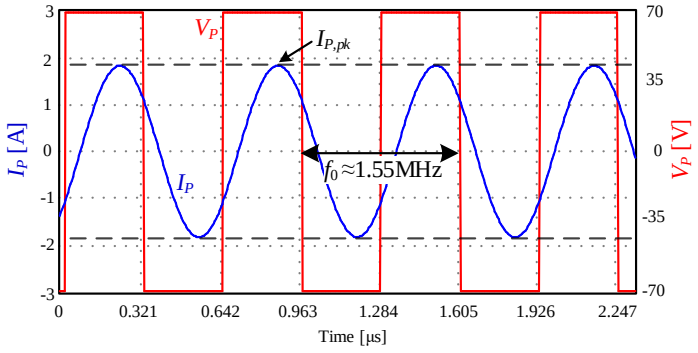

Fig. 2.7 Simulated waveforms of the currents and voltages for symmetrical matching parameters (dashed lines are the behavioral model predictions): (a) Primary, (b) Secondary.

The second set of simulations was carried out for asymmetrical matching parameters: L_P=67 µH, C_P^* ≈C_P =156 pF for the primary side, and L_S=90 µH, C_S^*≈C_S=116 pF for the secondary side. Fig. 2.8 depicts simulation waveforms of the currents and voltages of the primary and secondary sides. As can be seen, the obtained results match the model predictions. It can also be seen that the resulting output current is lower than that in the symmetrical case shown in Fig. 2.7. This is due to the lower transconductance gain in the case with a lower value of C_S.

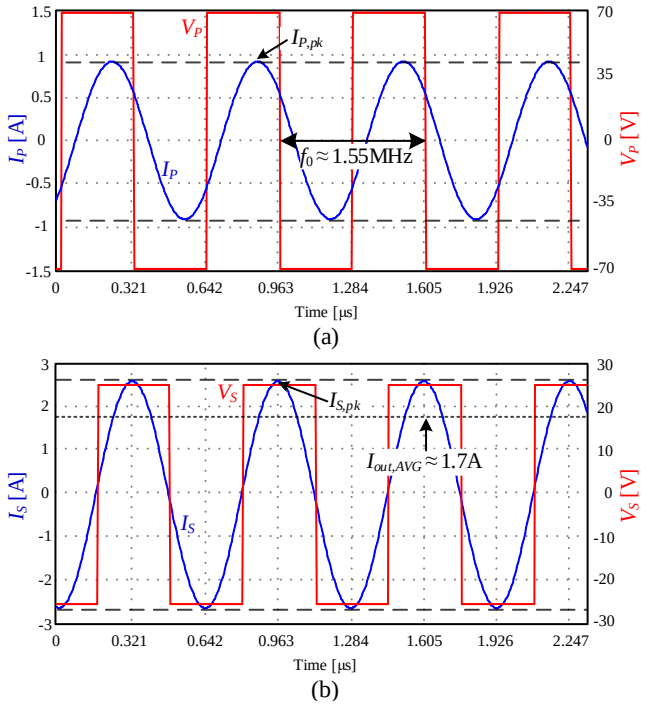

Fig. 2.8 Current and voltage simulation results for asymmetrical matching parameters (dashed lines are the behavioral model predictions): (a) Primary, (b) Secondary.

Finally, the calculated results for the average output current of an asymmetrical case were plotted against the results obtained from the simulation. These are depicted in Fig. 2.9, where Fig. 2.9a shows the current as a function of the input voltage, and Fig. 2.9b shows the current as a function of the coupling capacitances. A very good agreement is obtained throughout these simulations. As can be seen in Fig. 2.9b, as predicted by the model in (2.12), the output current is inversely proportional to the mutual coupling capacitance C_M. Therefore, the output power will follow a similar trend.

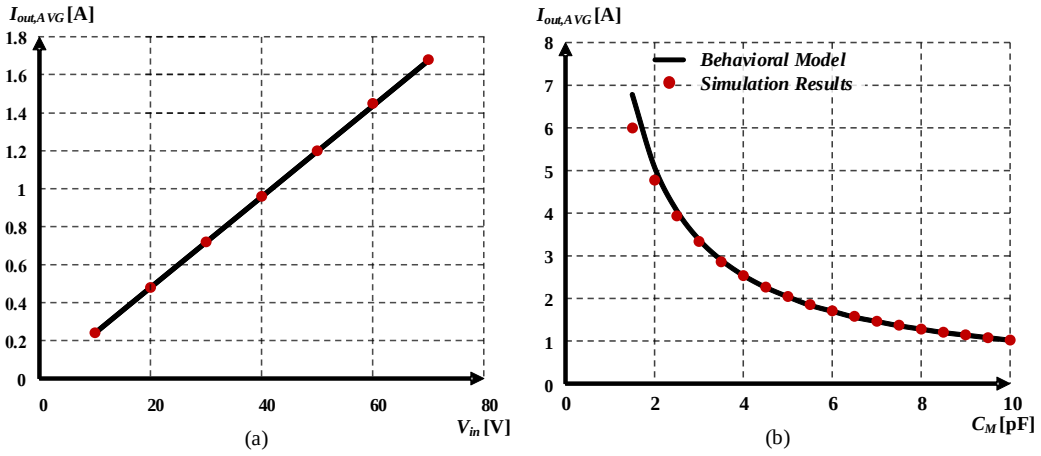

Fig. 2.9 Behavioral model and simulated average output current, $I_{out,AVG}$. Curves are an asymmetrical setup: (a) As a function of the input voltage V_{in},. (b) As a function of the mutual coupling capacitance C_M.

2.4 Simulation–Compatible Capacitive Medium Modeling

The coupling capacitance of the medium depends on various factors such as conductors, dielectric material, alignment, and distance between the coupling plates. Evaluation of a WPT system in a simulation environment for these variables over time or frequency is a major challenge since continuous variable capacitance is required. To date, this element is generally absent from common simulation software packages. Methods to obtain the medium characteristics either involve rigorous and tedious experiments and/or a finite element analysis [78]. However, even in cases in which these characteristics are obtained, the analysis of their interaction with the electrical circuit is still required. To this end, a continuous-time model for variable capacitors, which can be extended to a variable-capacitance network model, has been developed and implemented in a PSIM platform.

In this study, the methodology to model a continuous-time variable inductance, as described previously in [65],[101], was employed and adapted to describe a variable capacitance. As illustrated in Fig. 2.10 , the model comprises two dependent voltage and current sources, which emulate a non-linear transformer and a capacitor with a reference capacitance. The characteristics of the non-linear transformer are defined by the following relationships:

$$\begin{aligned} V_2 &= K_{cap} V_1 \\ I_2 &= I_1 \end{aligned} \quad , \tag{2.14}$$

where K_{cap} is the transformer's scale factor between the primary and secondary sides, and C_{ref} is the constant reference capacitance. From (2.14), the capacitive impedance reflected to the primary side, Z_C, with respect to the capacitive impedance at the secondary, Z_{Cref} is:

$$\begin{cases} Z_C = \dfrac{1}{j\omega C} = \dfrac{V_1}{I_1} = \dfrac{V_2}{K_{cap} I_2} \\ Z_{Cref} = \dfrac{1}{j\omega C_{ref}} = \dfrac{V_2}{I_2} \end{cases} \Rightarrow Z_C = \frac{1}{K_{cap}} Z_{Cref} \quad , \tag{2.15}$$

and therefore, the capacitor value reflected to the primary side is obtained as:

$$C = K_{cap} C_{ref} \quad . \tag{2.16}$$

For the sake of simplicity, C_{ref} has been set to 1F. In this case, the effective capacitance that is reflected across the capacitor terminals equals the scale factor K_{cap}. To evaluate a WPT system for continuous operation, K_{cap} can be made dependent on system

parameters such as changes in distance and/or coupling capacitance, matching network variations and mistuned resonant frequency. Thus, a voltage-dependent variable capacitor is emulated between nodes *C*+ and *C*-, as shown in Fig. 2.10.

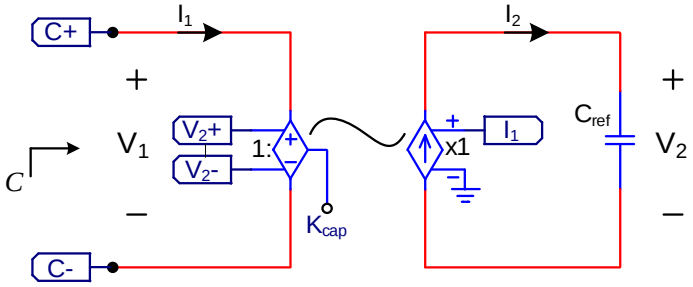

Fig. 2.10 Continuous variable capacitor model implemented in PSIM platform.

Now, having a continuous-time behavioral model of a variable capacitor, the variable capacitive medium π-model of Fig. 2.11a can be created by means of three voltage-dependent voltage sources, as illustrated in Fig. 2.11b, where the reference capacitances are not depicted for clarity.

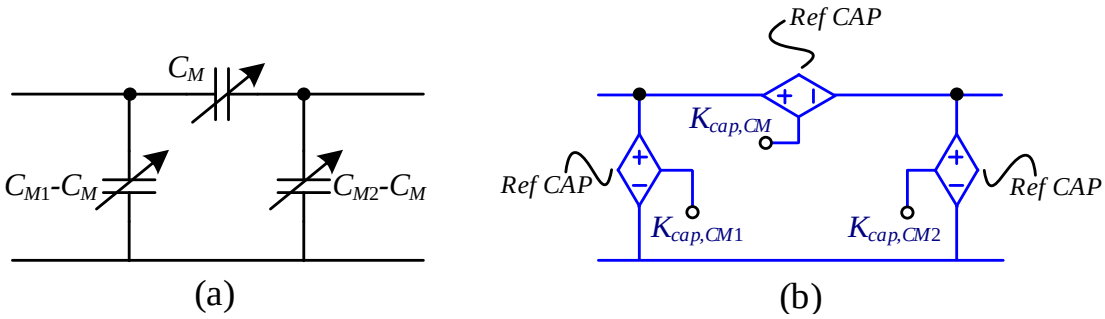

Fig. 2.11 Variable capacitive medium π-model. (a) Electrical model, (b) Representation of the variable medium by three voltage-dependent voltage sources for simulation purposes.

In order to evaluate the performance of a double-sided L-type system for continuous medium (distance) variations, based on the above-presented modeling technique, a simulation test bench with variable capacitors was constructed as shown in Fig. 2.13. There, for convenience, the capacitive medium is illustrated by variable capacitor symbols. Simulations were carried out under nominal operating conditions and matching networks that were identical to those of the asymmetrical case study in Section 2.3, whereas the initial coupling capacitance was 3.5 pF.

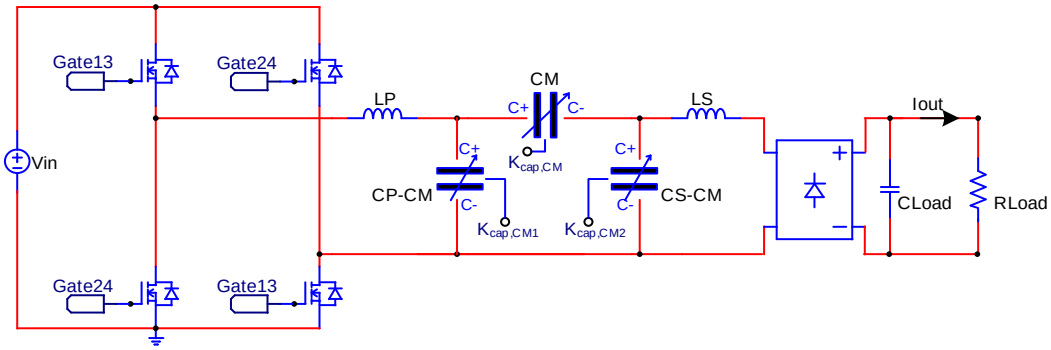

Fig. 2.12 Schematic simulation test bench of the WPT system with variable capacitor symbol illustrations for the capacitive medium.

Fig. 2.13a shows the result of the average value of I_{out} for a 1.5 pF variation of the mutual capacitance, such that the final coupling capacitance is C_M =5 pF. The solid red line shows the simulation result, whereas the dashed blue markers show the behavioral model outcome. It can be observed that the results of the cycle-by-cycle simulation and behavioral model are in very good agreement. It can be further noticed that when C_M increases, the output current decreases as expected from the theoretical analysis. Fig. 2.13b shows the output current for a medium step-down variation of 1.5 pF such that the final coupling capacitance is C_M=2 pF. The output current settles on approximately 5 A for both the model and cycle-by-cycle simulation, which well suits the theoretical predictions, as shown in detail in Fig. 2.9b. It should be noted that since the resonant tank is operated at a significantly higher frequency than the output filter time constant (R_{Load} and C_{load}), it is assumed to be instantaneous from a dynamic perspective. This is exemplified in Fig. 2.13, where it can be observed that the system response to step variation of C_M can be well approximated to the output filter time constant.

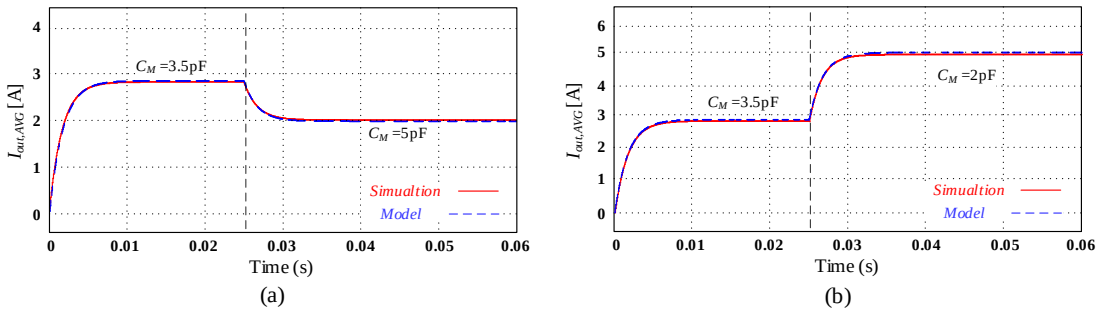

Fig. 2.13 Average output current, I_{out}, for capacitive medium variations with initial mutual capacitance C_M = 3.5 pF; (a) Step-up of 1.5 pF, (b) Step-down of 1.5 pF.

2.5 General Model Validation

To further validate and examine the behavioral modeling approach, an experimental double-sided L-type capacitive WPT prototype with four copper plates that form the capacitive coupling was constructed, as shown in Fig. 2.14. The coupling plates were designed symmetrically such that each plate was 25x25 cm. Thus, the matching networks were also designed to be symmetrical, with $L_P = L_S \approx 67$ µH and $C_P = C_S = 156$ pF. The gate drive signals of the full-bridge inverter were generated with a Cyclone IV FPGA [102] at an operating frequency slightly above a resonance of $f_0 \approx 1.558$ MHz, guaranteeing soft-switching operation. The full-bridge inverter was implemented with GaN modules that were operable at several MHz [103]. To reduce the limitations due to magnetic and skin-effect losses in the MHz range [104],[105], the matching inductors, L_P and L_S, were constructed with an AWG 48 litz wire wrapped on an air core. It should be noted that the actual litz wire resistance at the operation frequency of the MHz range may be different than the manufacturer-specified resistance, typically at 100 kHz. High-voltage multilayer SMD ceramic capacitors were used in parallel to form the desired matching capacitors C_P and C_S.

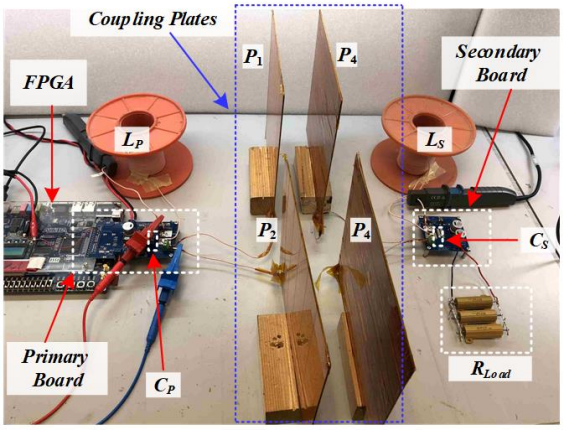

Fig. 2.14 Experimental setup of a capacitive WPT prototype.

To facilitate a reliable estimation of the capacitive coupler for the experimental measurements, estimation of the plate capacitance was carried out by a Maxwell (Ansys) finite element analysis tool. A rigorous simulation procedure of various dimensions and geometries was conducted to determine the mutual capacitance, C_M, for the given coupling plates under various air gaps.

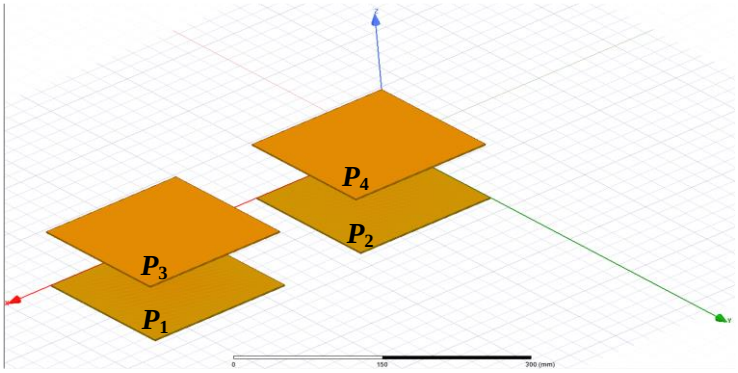

Fig. 2.15 Maxwell (Ansys software) simulation test bench for the capacitive coupler design.

Fig. 2.16 shows experimental waveforms of the system for input voltage V_{in}=70 V and a load resistance of R_{Load} =15 Ω, whereas the distance between the plates is 50 mm resulting in a coupling capacitance of C_M ≈6 pF. Fig. 2.16a shows the primary sinusoidal current I_P. As can be seen, the current is slightly lagging in the primary voltage V_P , validating a soft-switching operation. The sinusoidal current at the secondary I_S is shown in Fig. 2.16b. The obtained peak value (3.4 A), as well as the resulting average value (~2.2 A) at the secondary, are similar to the simulation results shown in Fig. 2.7b with a small error of 4%. It should be noted that although the matching network on the secondary side is not perfectly tuned to the resonant frequency due to small system parasitics, the experimental measurements tightly follow the behavioral model predictions. The overall operating conditions and parameters of the experimental prototype are summarized in Table I.

TABLE I EXPERIMENTAL CPT PROTOTYPE VALUES AND PARAMETERS

Parameter	***Value/Type***
Input voltage V_{in}	70V
Output current $I_{out,AVG}$	up to 4 A
Load resistance R_{Load}	15 Ω
Coupling plates	250x250 mm
Coupling capacitance C_M / air-gaps	3-10 pF / 25-100 mm
Full-bridge transistors	LMG5200, 80 V, 15 mΩ, Dual
Rectifier diodes	5 A/200 V, VSSC520S-M3
Inductors L_P and L_S	~67 µH
Capacitors C_P and C_S	156 pF, AVX MLLC 5 kV
Output capacitor C_{Load}	200 µF, EEV-FK2A101M
Resonant frequency f_0	~1.558 MHz

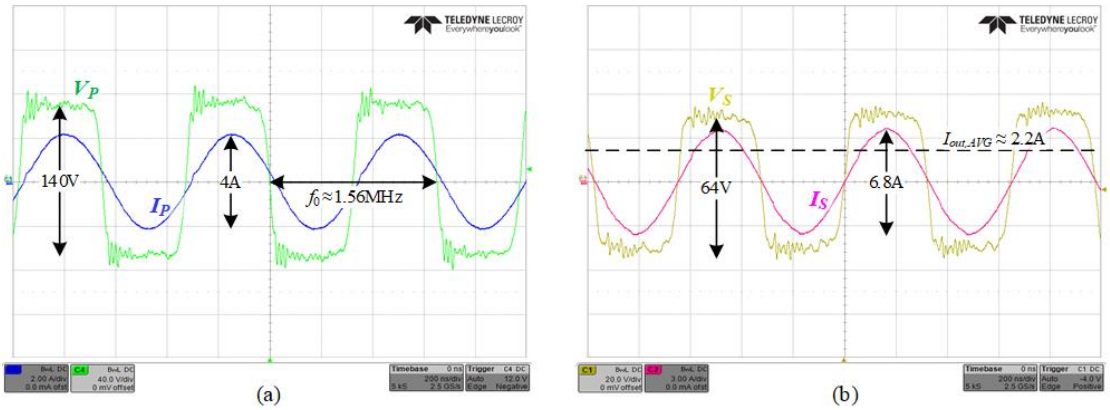

Fig. 2.16 Experimental waveforms with operating conditions: V_{in}=70 V, R_{Load} =15 Ω, coupling capacitance C_M ≈6 pF: (a) Primary side V_P 40V/div, I_P 2A/div, (b) Secondary side V_S 20V/div, I_S 3A/div; Time scale 200ns/div.

To further verify the strength of the behavioral model, the average output current was measured for various input voltages for a constant C_M of 6 pF; the results are summarized in Fig. 2.17. The experimental measurements tightly follow the results obtained by the simulations, as well as the model predictions. It can be noticed that the output current (as well as the output power) increases with the input voltage, as predicted from the gyrator current–voltage relationships obtained in Section 2.3. Fig. 2.18 depicts the output current comparison between experimental, simulated, and behavioral models for various air gaps between 25 mm and 100 mm, which corresponds to a mutual capacitance range of 3-to-10 pF approximately, thus, demonstrating variations in distance and/or displacement (while V_{in}=70 V). This way, the inversely proportional behavior between the capacitive coupling and the output current is well validated by the experimental measurements. It can be seen that for relatively small C_M, the measured current is lower than predicted. This discrepancy can be explained by the fact that beyond a certain distance, the system goes from a near-field to a far-field operation, and it behaves as an antenna rather than a coupling system. This implies that some assumptions that have been made for the behavioral model analysis are not satisfied.

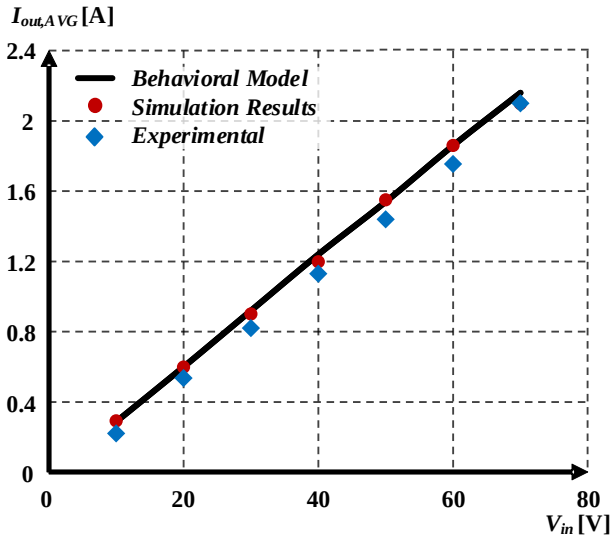

Fig. 2.17 Average output current, $I_{out,AVG}$, curve as function of the input voltage V_{in}, for 50 mm air gap.

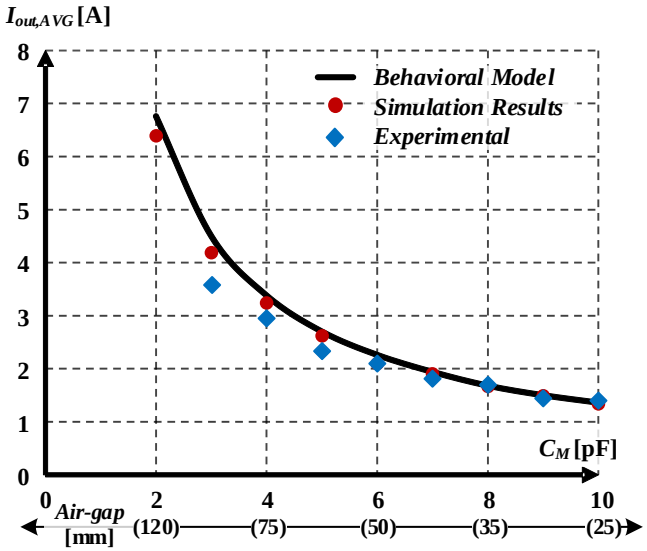

Fig. 2.18 Average output current, $I_{out,AVG}$, curve as a function of the mutual coupling capacitance C_M /air-gaps for V_{in}=70 V.

CHAPTER 3: Simulation-Compatible Capacitive-Coupler Modeling and Analysis for Wireless Power Transfer Applications

3.1 Introduction

The analysis and design of CPT systems strongly relies on a through representation of the CC's behavior. A basic model of the CC is by a pair of capacitors in series [32] , [50],[85],[107],[108]. However, this model is limited for specific, well-aligned plates, with strict constraints on their geometry and distance. Advanced approaches to model the coupler in the context of WPT, covering scenarios of CPT system variations such as misalignment, displacement, and cross-coupling interactions between the transmitter and receiver have been reported in the literature [47],[52],[55],[84]. Still lacking, however, is evaluation of the different models, benefits, and drawbacks oriented toward design requirements. A comprehensive understanding of CC modeling. combined with a suitable realization simulation platform, are beneficial for CPT design and optimization, and assist in a smoother transition toward practical implementations.

Therefore, the objective of this chapter is to overview and compare several electrical representations of the CC, along with simulation-compatible models, that enable visualization and evaluation of the CPT system under (and through) variations of the system parameters. It is shown that proper choice of a CC model enables significant simplification of the static and dynamic analyses of an entire capacitive WPT. It is a further objective of this study to utilize a "series" (Thevenin) model on a CC, while highlighting its benefits through a CPT case study.

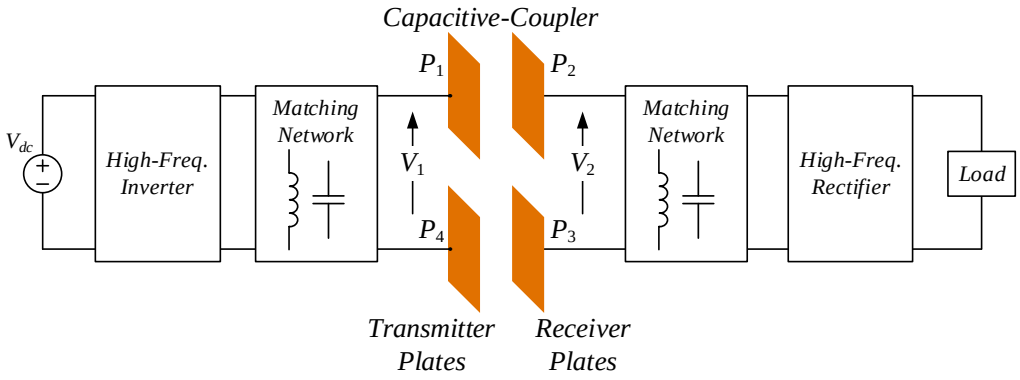

Fig. 3.1 Simplified block diagram of a wireless CPT system with a conventional two pair capacitive-coupler arrangement.

3.2 Review: Capacitive-Coupler Modeling

Various arrangements of the CC have been thoroughly discussed in prior articles [32], [37],[49],[84]. To establish definitions that are used throughout this chapter and for the sake of clarity, the essential details are briefly reviewed. A typical CC

configuration is shown in Fig. 3.1, whereas its simplified equivalent electrical circuit is depicted in Fig. 3.2. The circuit comprises of six lumped capacitors [37],[52],[55], such that each represents the coupling between the corresponding plates of the CC (Fig. 3.2).

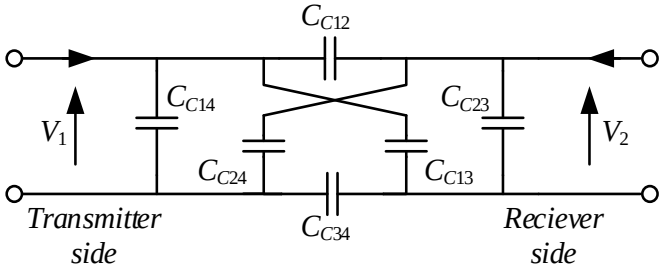

Fig. 3.2 Equivalent capacitance model of the CC.

Generally, the CC can be treated as a 2-port network with two inputs on the transmitter side and two outputs on the receiver side, as shown in Fig. 3.3. The capacitors "seen" at the input and at the output of the coupler are denoted in Fig. 3.3 as C_p and C_s, respectively. Hence, the current and voltage relationships at the input and the output can be expressed as follows:

$$\begin{cases} I_1 = C_p \dfrac{dV_1}{dt} + C_{ps} \dfrac{dV_2}{dt} \\ I_2 = C_{sp} \dfrac{dV_1}{dt} + C_s \dfrac{dV_2}{dt} \end{cases}, \tag{3.1}$$

where I_1, I_2, V_2, and V_2 are input and output currents and voltages, and $C_m = -C_{ps} = -C_{sp}$ is the mutual capacitance. Solving the Kirchhoff equations at the input and at the output yields [37],[52],[55]:

$$\begin{cases} C_p = C_{C12} + \dfrac{(C_{C12} + C_{C13})(C_{C42} + C_{C43})}{C_{C12} + C_{C13} + C_{C42} + C_{C43}} \\ C_s = C_{C23} + \dfrac{(C_{C12} + C_{C42})(C_{C13} + C_{C43})}{C_{C12} + C_{C13} + C_{C42} + C_{C43}} \\ C_m = \dfrac{C_{C43}C_{C12} - C_{C13}C_{C42}}{C_{C12} + C_{C13} + C_{C42} + C_{C43}} \end{cases}. \tag{3.2}$$

Similarly to an inductive-based coupler, the coupling coefficient between the input and the output is expressed as:

$$k_{CC} = \frac{C_m}{\sqrt{C_p C_s}}. \tag{3.3}$$

According to (3.1), a few possible CC models are devised and detailed in the following subsections.

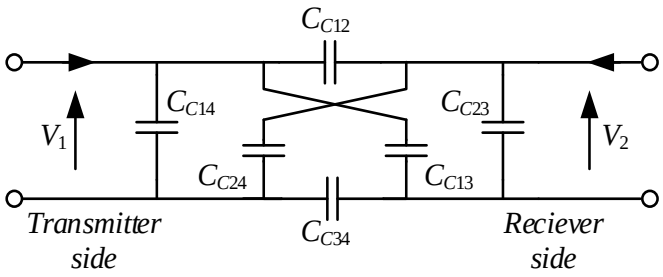

Fig. 3.3 CC as a 2-port network.

3.2.1 π-model

Equation (3.1) can be rewritten in the following form:

$$\begin{cases} I_1 = \left(C_p - C_m\right)\dfrac{dV_1}{dt} + C_m \dfrac{d}{dt}(V_1 - V_2) \\ I_2 = C_m \dfrac{d}{dt}(V_2 - V_1) + \left(C_s - C_m\right)\dfrac{dV_2}{dt} \end{cases}, \tag{3.4}$$

which can be further represented as a π-model, as shown in Fig. 3.4 [37],[47],[49]. This model can be applied to any circuit simulation platform without modifications. It should be emphasized that the transmitter and receiver sides are not separated in this model (i.e., without isolation, as in the practical system). Then, in the context of a complete CPT system and considering all other system circuits (e.g. matching networks), its overall analytical analysis can be rather complex.

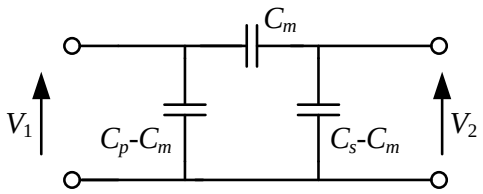

Fig. 3.4 π-model representation of the CC.

3.2.2 Parallel (Norton) model

The input and the output currents in (3.1), are given by the sum of two capacitors' currents, which can be translated to electrical circuitry representation, as delineated in Fig. 3.5.

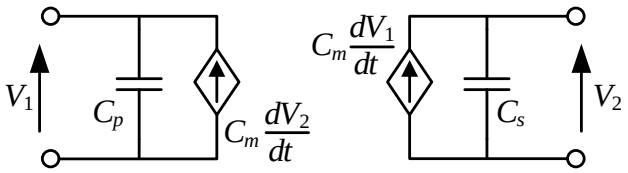

Fig. 3.5 Norton model of the CC.

The voltage-dependent current sources in Fig. 3.5 can be implemented, for instance, by a behavioral model (such as EVALUE in SPICE) where {*expression*} is defined as

a derivative of V_1 or V_2 times C_m. This is demonstrated in Fig. 3.6 for SPICE-compatible simulators, where the derivatives of V_1 and V_2 are calculated by applying SPICE's built-in function DDT. It should be emphasized, however, that due to the use of the function "DDT", the implementation of this simulation-compatible model is only valid for time-domain analysis. An alternative method to facilitate the derivative function is by a passive RC network or differentiator using an active amplification stage. These methods are compatible with SPICE's ac analysis, however, an additional root at relatively low frequency is introduced to the system dynamics.

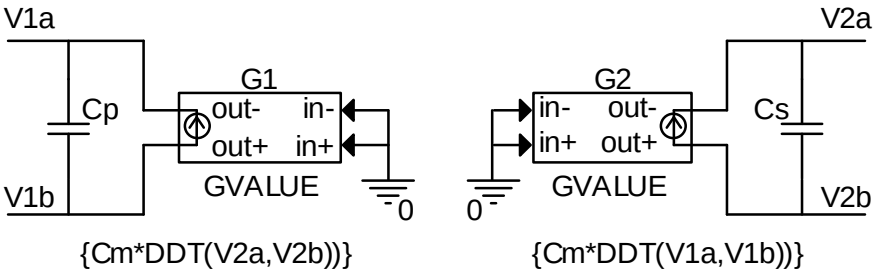

Fig. 3.6 SPICE-compatible implementation of the Norton model.

Another simulation-compatible approach for the parallel (Norton) modeling approach is depicted in Fig. 3.7. There, the voltage-dependent current sources of the transmitter and receiver sides are generated by replicating the current of two auxiliary capacitors, C_{aux1} and C_{aux2} (which are equal in value to C_m) and are exposed to the voltages V_2 and V_1, accordingly [8]. The modeling approach is applicable in both frequency and time domain analyses.

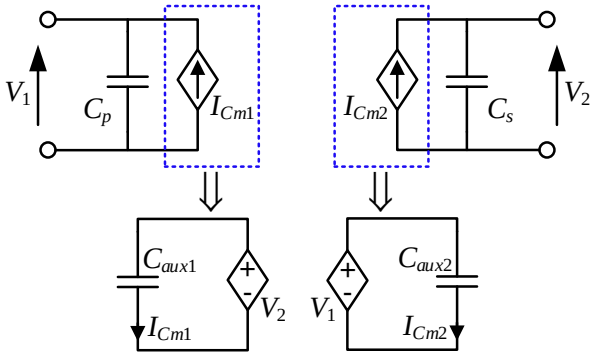

Fig. 3.7 Simulator-compatible implementation of the Norton model by using auxiliary capacitors.

3.2.3 Series (Thevenin) model

A further modification of the circuit model presented earlier is facilitated by applying the Thevenin theorem to the left and to the right parts of Fig. 3.5. This yields dependent voltage sources in series with capacitors $C_{p/s}$, as shown in Fig. 3.8. In this case, the derivative action is eliminated, the outputs of the dependent voltage sources

are determined by a simple expression with basic arithmetic operators; thus, the series model can be implemented as-is in any simulation platform.

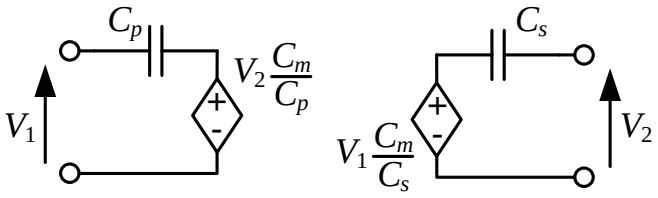

Fig. 3.8 Thevenin model of the CC.

3.2.4 Capacitive-coupler model comparison

The π-model (Fig. 3.4) is straightforward and can be easily applied to every circuit simulator without modifications. However, the capacitance on both the input and output sides depend on the mutual capacitance, C_m, which is highly dependent on the coupler's variations, i.e., displacement and misalignment of either the transmitter, receiver, or both. Consequently, unless all three capacitors of the π-model are represented by their behavioral counterparts, emulating variable capacitances [1],[65],[109], this approach is not valid for the system's dynamic medium behavior evaluation. In addition, since C_m is connected to both the input and output of the CC, the equations describing the overall CPT system are expected to be more complex. This complicates the overall analytical analysis of the system, forcing a rigorous super-positioning procedure for evaluation of the circuit, and as a result, extracting insights of the system's intricate operation is quite challenging.

From an analytical complexity perspective, the parallel (Norton) approach (Fig. 3.5) is simpler to derive when compared to the π-model. Here, too, varying C_m during the simulation run-time is impossible, unless C_{aux1} and C_{aux2} are implemented as behavioral model capacitances [1],[65],[109]. Utilization of variable capacitance is worked around in the series modeling approach (Fig. 3.8), where C_m appears as a parameter in the dependent voltage sources' expressions. This implies that unlike the other two precursor models, C_m can be emulated by any voltage or current in the circuit. For example, creating a voltage node denoted as "C_m", which is set by a dc source (detailed in Section 3.4). By doing so, the mutual capacitance can be varied on-the-fly during the simulation run-time. This enables designers to examine the system's dynamics, variations in the medium, and more.

3.3 Applying the "Series" Thevenin Model to Analytical Analysis of a CPT System

All the CC models described above can be utilized for an analytical analysis of a CPT system. In some cases, selection of one model or another can significantly simplify or complicate the derivations and the overall design procedure. While the π-model and "parallel" model are well known to designers, and have established a track record, the series model which has a significant potential for simplification, has been somewhat overlooked. The following sections discuss and demonstrate the applicability of this modeling approach to different aspects of a CPT design.

Following the observations made in the previous section, a capacitively-coupled power transfer system with a double-sided *LC* matching network [36],[37] was analyzed. The schematic diagram of the full system is shown in Fig. 3.9. The system comprises a full-bridge inverter at the front end (Q_1-Q_4), which is operated at a switching frequency, f_{SW}; *LC* matching networks L_{m1}, C_{m1}, and L_{m2}, C_{m2}; a capacitive coupler; an output rectifier D_1-D_4; and a load R_L. It is assumed that both of the matching networks are tuned to f_{SW}.

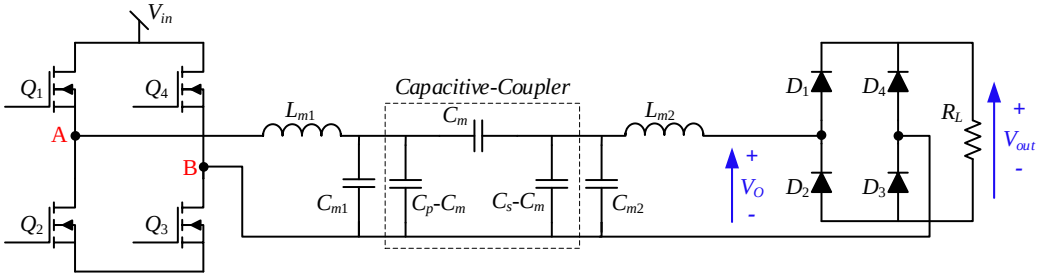

Fig. 3.9 Schematic diagram of capacitively-coupled WPT system with *LC* matching networks.

The matching networks are usually designed to have a high-quality factor implying that the system's behavior can be analyzed using a first harmonic approximation [99], as depicted in Fig. 3.10. V_p and V_s represent the first harmonics of the square waves V_{AB} and V_O; $Z_O = \frac{8}{\pi^2} R_L$; $C_1 = C_{m1} + C_p - C_m, C_2 = C_{m2} + C_s - C_m$. The magnitudes of V_p and V_s are $V_{pm} = 4V_{in}/\pi$ and $V_{sm} = 4V_{out}/\pi$, respectively.

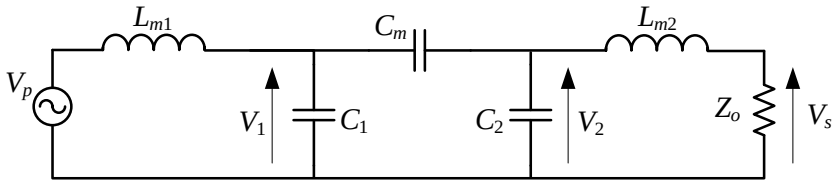

Fig. 3.10 First harmonic approximation of the double-sided *LC* CPT system.

It should be noted that in many practical designs, the capacitances C_p and C_s are very low, on the order of several pFs [46]-[48]. Thus, to obtain a resonant operation at frequencies even as high as in the megahertz range, very high matching network inductances are needed [37]. Therefore, to stay at reasonable switching frequencies, while still operating at resonance, C_{m1} and C_{m2} are chosen to be much higher than C_p and C_s, and, consequently, $C_1 \approx C_{m1}$ and $C_2 \approx C_{m2}$. The capacitive coupler and the matching capacitors can be then replaced with the series Thevenin model as discussed in Section 3.2.3, and the resultant circuit is delineated in Fig. 3.11.

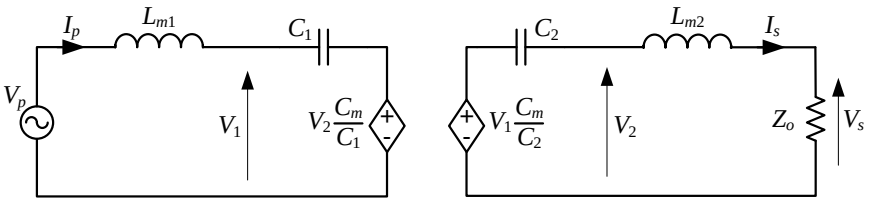

Fig. 3.11 Simplified equivalent circuit of the double-sided *LC* system using the Norton model.

Now, both the transmitter and receiver sides are represented by a single branch, which significantly simplifies the analysis. For example, the output-to-input voltage ratio can be found intuitively by inspection. Taking into consideration that such systems are operated at resonance [37],[48],[54],[63], the relationship between V_p and V_2 is obtained as follows:

$$V_p = V_2 \frac{C_m}{C_1}. \tag{3.5}$$

V_2 can be found from the right branch (Fig. 3.11) as follows:

$$V_2 = V_s + \frac{V_s}{Z_O} Z_{Lm2} = V_s \left(1 + \frac{Z_{Lm2}}{Z_O} \right), \tag{3.6}$$

where $Z_{Lm2} = j \cdot 2\pi f_{sw} L_{m2}$. Substituting (3.6) into (3.5) yields:

$$\frac{V_s}{V_p} = \frac{C_1}{C_m} \cdot \frac{1}{1 + jQ}, \tag{3.7}$$

where $Q = \frac{2\pi f_{sw} L_{m2}}{Z_0}$. The obtained result is in excellent agreement with the results of the analyses presented in prior articles [1],[6].

Another example would be finding the relationship between the receiver current and the voltage source at the transmitter. This can be achieved by expressing the voltage V_2 as a function of the current I_s (see right branch in Fig. 3.11),

$$V_2 = I_s \left(Z_{Lm2} + Z_O \right). \tag{3.8}$$

Substituting (3.8) into (3.5) yields:

$$\frac{I_s}{V_p} = \frac{1}{Z_O(1+jQ)}. \tag{3.9}$$

The expression in (3.9) attests to current sourcing behavior (gyrator) of the system again, as has been shown in previous publications [1],[6].

3.4 Model Realization in Simulation Platforms

Fig. 3.12 shows the implementation of the series model in two popular simulation platforms – PSpice and PSIM. In Pspice implementation (Fig. 3.12a), the input and output voltages are constructed by series connection of the capacitors C_1 and C_2 with the dependent voltage sources E_1 and E_2 in accordance (the capacitors' values, C_p and C_s, are defined as global variables). C_m is emulated by the voltage that is set by the output of the dependent voltage source E_3. This voltage (V(Cm)) is then used in the expressions of E_1 and E_2, which are defined according to Fig. 3.8.

Similarly, in PSIM implementation (Fig. 3.12b), V_3 and V_4 are used as dependent voltage sources, whose behavior is controlled by the computational blocks F_1 and F_2. Both of them have two inputs: the first (x1) is fed from a differential amplifier AMP1 and AMP2 that sense the voltages V_1 and V_2, respectively, and the second input (x2) is connected to voltage node "*Cm*", which emulates the coupling capacitance C_m by the computational block F_3.

Aside from the traditional time-domain simulation run where the "end-time" (e.g., TSTOP simulation time period) is defined explicitly, some simulation platforms offer a "free-run" mode, where the simulation does not end until it is manually interrupted. In this mode, the user can change a variety of the circuit's parameters during the simulation run while examining the circuit's waveforms. This might be a useful way to examine the system's response to mutual capacitance variations. In the PSIM platform, for example, this can be done by replacing the block F_3 in Fig. 3.12b with a DC voltage source, setting its magnitude to the value of the expected mutual capacitance C_m, and changing it then during the simulation run.

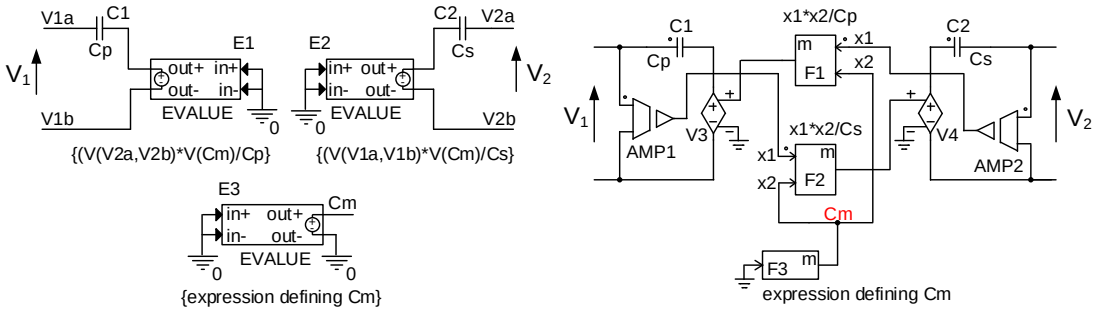

Fig. 3.12 CC series Thevenin model implementation in simulation platforms: (a) SPICE, (b) PSIM.

The models and simulation-compatible framework introduced in this section will be used in the following sections throughout practical use cases and systems.

CHAPTER 4:
Soft-Switching in Capacitive-Coupled Wireless Power Transfer with *LCLC* Compensation Networks

4.1 Introduction

In the last few years a double-sided *LCLC* compensation network structure for CPT (Fig. 4.1) has been widely studied [37],[46],[47]. There, each side of the converter incorporates a T-type network consisting of an *LCL* branch [47]. Combined with the parallel capacitance of the medium (or additional parallel capacitance), this results in a cascaded *LC* structure. The double-sided *LCLC* configuration assures that the output power is proportional to the coupling coefficient, which is also loosely coupled from the components' values [46],[47]. This is a significant benefit compared to other network setups employed in CPT [36],[37],[48]. In addition, the voltage and current stresses on the components are lower than in other methods, in particular, when increasing the distance between the transmitting and receiving sides [36],[37],[46]-[48]. In spite of the considerable advantages this configuration provides, operation at high frequencies is strongly associated with significant switching losses. Thus, to further improve *LCLC*-based CPT systems without compromising on system efficiency, a mechanism that assures soft-switching for wide operation range, covering all loading cases is mandatory, in particular, in the context of CPT systems where the parameters dynamically vary due to changes in distance or misalignment between the transmitting and receiving sides.

The objective of this chapter is to introduce a detailed analysis on the conditions for soft-switching in an *LCLC*-compensated resonant-capacitive WPT system oriented for resistive loads on the receiving side. The analysis methodology is to explore the affecting factors on the current at the turn-off instance, and consequently, to outline the requirements for soft-switching at turn-on and turn-off. This is achieved without compromising the overall performance of the system. In addition, simulation-compatible models of the capacitive coupler (as discussed in Chapter 3) are utilized for the *LCLC* configuration and time-continuous variable inductor that enable evaluation of the system under (and through) variations of the various parameters.

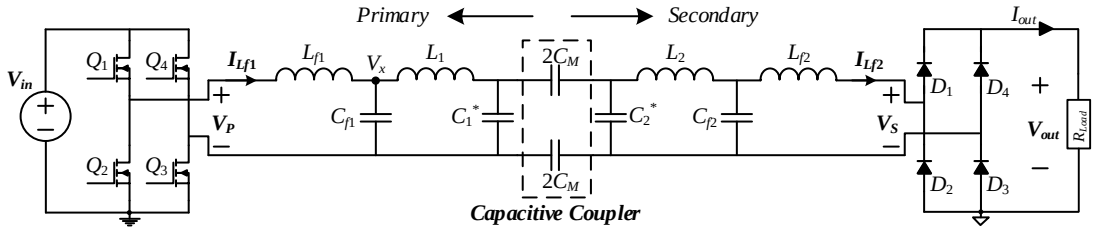

Fig. 4.1 Schematic diagram of an *LCL*-compensated capacitive WPT system with resistive load on the receiving side.

4.2 Analytical Model and Soft-Switching Analysis

A resonant-capacitive *LCLC* WPT system is shown in Fig. 4.1. The system is driven by a full-bridge inverter (Q_1-Q_4). The load, which is represented by a resistor, R_{Load}, is fed through a diode rectifier (D_1-D_4). Both the primary and secondary side are compensated by *LCLC* resonators (L_{f1}, C_{f1}; L_1, C_1^*; L_{f2}, C_{f2}; L_2, C_2^*). The capacitive coupler in this study is implemented by two pairs of plates [36] ,[47]. Assuming that the two pairs are placed sufficiently far from each other, the interconnection and fringe capacitances between the pairs can be neglected. Therefore, the capacitive coupler can be represented by two series capacitors as shown in Fig. 4.1, where C_M is the mutual coupling capacitance.

As discussed in detail in Chapters 2 and 3, the capacitive coupler can be modeled as a two-port network (Fig. 4.2a). With the aid of this two-port representation, assuming a high quality factor of the input and the output filters L_{f1}, C_{f1} and L_{f2}, C_{f2}, respectively, and by applying fundamental harmonics approximation (FHA) method [99], the system can be further simplified, as shown in Fig. 4.2b. There, V_{P1} represents the first harmonics source of the square wave V_P (Fig. 4.1), whereas $V_{P1} = 4V_{in}/\pi$, and $Zo = 8R_{Load}/\pi^2$. It should be noted that in the equivalent circuit model of Fig. 4.2, the capacitances C_1 and C_2 are defined as $C_1^* + C_M$ and $C_2^* + C_M$, respectively.

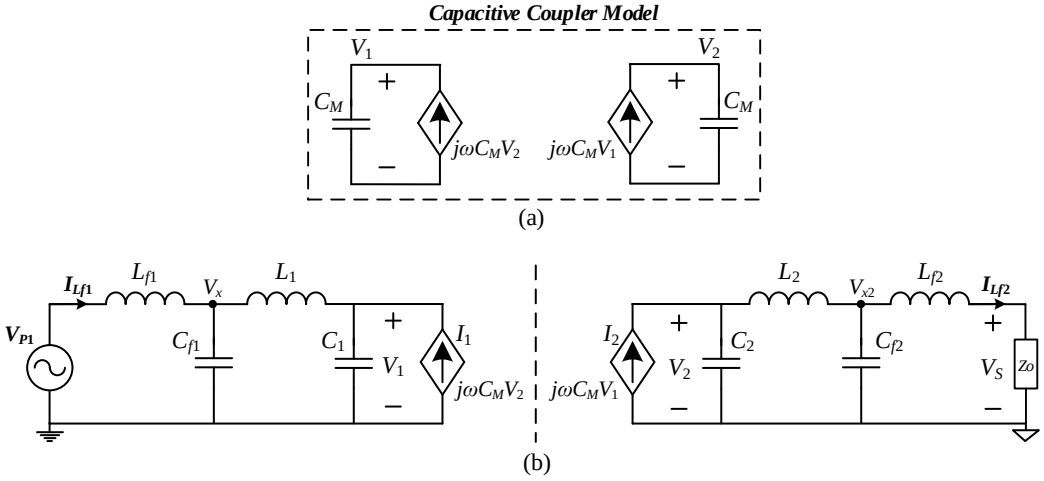

Fig. 4.2 (a) Two-port model of the capacitive coupler; (b) Simplified electrical model of an *LCLC*-compensated CPT system by applying FHA analysis.

By applying Thevenin's theorem to C_1 and I_1 on the input side and to C_2 and I_2 on the load side, the electrical model of the *LCLC*-based CPT system can be further modified, as shown in Fig. 4.3. The signals' relationships of the modified electrical model have been derived assuming that the resonant frequencies of the compensation

networks' resonators at the input and on the load sides, except for L_1 and C_1, are tuned to the switching frequency, such that:

$$f_r = f_{sw} \Rightarrow \begin{cases} Z_{Lf1} + Z_{Cf1} \approx 0 \\ Z_{Lf2} + Z_{Cf2} \approx 0 \\ Z_{L2} + Z_{C2} \approx 0 \end{cases}, \tag{4.1}$$

where f_r and f_{sw} are the resonant and switching frequencies, respectively, and Z_{Cx} and Z_{Lx} are the impedances of the corresponding capacitors and inductors in Fig. 4.3 (x denotes the index number).

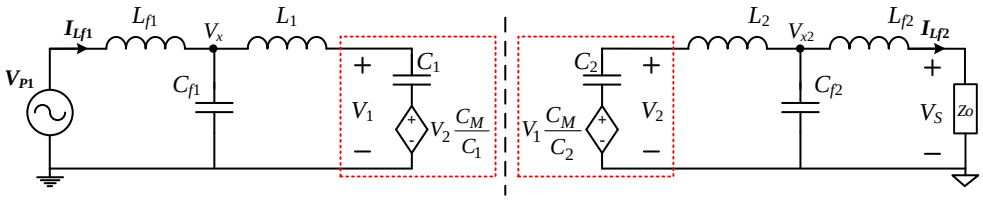

Fig. 4.3 Modified electrical model of an *LCLC*-compensated CPT system.

Using the relationships given in (4.1), and by applying Kirchhoff's voltage and current laws, the circuits in Fig. 4.3 can be described by the following expressions:

$$V_x\left(\frac{1}{Z_{Lf1}} + \frac{1}{Z_{Cf1}} + \frac{1}{Z_{L1}}\right) = \frac{V_{p1}}{Z_{Lf1}} + \frac{V_1}{Z_{L1}}, \tag{4.2}$$

$$V_1 = V_x \frac{Z_{C1}}{Z_{C1} + Z_{L1}} + V_2 \frac{C_M}{C_1} \frac{Z_{L1}}{Z_{C1} + Z_{L1}}, \tag{4.3}$$

$$V_{x2} = V_1 \frac{C_M}{C_2} = \frac{V_s}{Z_o}\left(Z_o + Z_{Lf1}\right), \tag{4.4}$$

$$V_s = \frac{\left(Z_o + Z_{Lf2}\right) \| Z_{Cf2}}{\left(Z_o + Z_{Lf2}\right) \| Z_{Cf2} + Z_{L2}} \cdot \frac{Z_o}{Z_o + Z_{Lf2}} V_2, \tag{4.5}$$

and since the resonators L_{f1}, C_{f1} and L_{f2}, C_{f2} are operated at the resonant frequency, equations (4.2) and (4.5) can be respectively simplified as follows:

$$\frac{V_x - V_1}{Z_{L1}} = \frac{V_{P1}}{Z_{Lf1}}, \tag{4.6}$$

$$V_s = \frac{Z_{Cf2} Z_o}{Z_{Lf2} Z_{Cf2} + Z_{Cf2} Z_o + Z_{L2} Z_o} V_2, \tag{4.7}$$

and substituting (4.6) into (4.3) yields:

$$V_s = \frac{Z_{C1}}{Z_{Lf1}} V_{P1} + \frac{C_M}{C_1} V_2, \tag{4.8}$$

by rearranging (4.7) and (4.8) and after some manipulations, the secondary-to-primary voltage ratio is obtained as follows:

$$\frac{V_s}{V_{P1}} = -\frac{C_{f1}}{C_m}\left(\frac{1}{k^2}-1\right)\frac{1}{(1+jQ)+L_{ratio}} \quad , \tag{4.9}$$

where $k = C_M/\sqrt{C_1 C_2}$ is the coupling coefficient of the capacitive coupler, $Q=Z_{Lf2}/Zo$, and $L_{ratio}=L_2/L_{f2}$. It can be observed from (4.9) that the voltage gain is independent of inductor L_1. Thus, changing the inductance of L_1 does not alter the input-to-output voltage gain, and consequently, this can be controlled by a standalone control loop which does not involve sensing of the output voltage.

The ZVS of the full-bridge switches depends on the current I_{Lf1} at the commutation instances. To obtain the ZVS, two conditions have to be met. The first and the necessary one is for the current I_{Lf1} to be positive while turning off the switches Q_1 and Q_3 (the negative transition of V_P), or negative while turning off the switches Q_2 and Q_4 (the positive transition of V_P). The second is that the current magnitude at the switching instance, I_{sw}, needs to be sufficient to recharge the body capacitors of the switches during the switching transition. The current I_{Lf1} can be obtained from Fig. 4.3 as follows:

$$\frac{dI_{Lf1}(t)}{dt} = \frac{V_P(t)-V_x(t)}{L_{f1}} \;;\; \begin{cases} V_P(t) = |V_{P1}|\sin(2\pi\, f_r t) \\ V_x(t) = |V_x|\sin(2\pi\, f_r t+\gamma) \\ |V_{P1}| = V_{in}\cdot \pi/4 \end{cases} \quad , \tag{4.10}$$

where $|V_x|$ and γ are the magnitude and the phase of V_x, respectively.

To find V_x, first the voltage V_2 is found from the load side (see Fig. 4.3) by inspection:

$$V_2 = V_1\frac{C_M}{C_2}\frac{\left(Z_o+Z_{Lf2}\right)\|\, Z_{Cf2}+Z_{L2}}{\left(Z_o+Z_{Lf2}\right)\|\, Z_{Cf2}+\underbrace{Z_{L2}+Z_{C2}}_{Z_2}} \;;\; f_{sw}=f_r \Rightarrow Z_2 = 0 \quad , \tag{4.11}$$

then by rearranging (4.6) and (4.11), and substituting them into (4.2) yields the following ratio:

$$\frac{V_x}{V_{P1}} = \alpha\frac{C_{f1}}{C_1}\frac{(1+jQ)\left(1-k^2-1/\alpha\right)+k^2 L_{ratio}}{(1+jQ)\left(1-k^2\right)+k^2 L_{ratio}} \quad , \tag{4.12}$$

where $\alpha = L_1/L_1^*$ is the normalized inductor's factor, and L_1^* is the normalized inductance which tunes the resonance frequency of the resonant tank L_1, C_1 to f_{sw}, i.e., L_1=1/(2π $f_{sw}C_1$). Substituting (4.9) into (4.7) yields:

$$I_{Lf1}(t) = \frac{1}{L_{f1}}\left(V_{in} \cdot t + \frac{|V_x|}{2\pi \cdot f_r}\cos(2\pi \cdot f_r + \gamma) - \frac{V_{in} \cdot \pi}{4\pi \cdot f_r} \right) . \tag{4.13}$$

Finally, the current at the switching event, I_{sw}, is obtained from (4.13) at t = π/ω (half a switching period as follows:

$$I_{sw} = \frac{1}{L_{f1}}\left(\frac{V_{in} \cdot \pi}{2\omega} - \frac{|V_x|}{\omega}\cos\gamma \right) . \tag{4.14}$$

Fig. 4.4 depicts the switching current, I_{sw}, as a function of the normalized inductance factor, α, for several coupling coefficients. For some predefined inductance value (α is constant, Fig. 4.4), the current I_{sw} decreases as the coupling coefficient, k, increases. This implies that if the switching current, I_{sw}, is designed to be positive for the highest expected coupling coefficient (highest C_M, smallest air gap), soft-switching is obtained over the entire air-gap range. However, to guarantee that the switches' body capacitors are recharged during the switching transition, I_{sw} needs to be kept high enough, regardless of variations in the input voltage and/or in the load. This can be done, as seen in Fig. 4.4, by changing the normalized inductance factor α. That is, if I_{sw} decreases (for example, at a lower power level operation), it can be reverted to its initial value by decreasing α (i.e., by decreasing L_1).

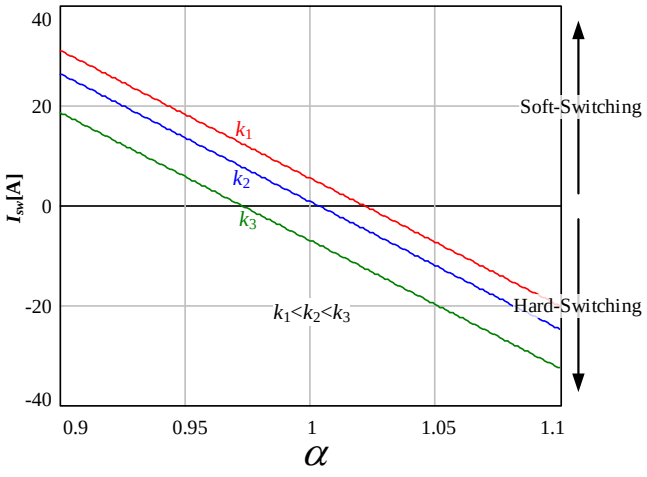

Fig. 4.4 Current I_{sw} as a function of the normalized inductance factor α.

4.3 Simulation-Compatible Models

To further investigate the implications of the coupling capacitance and L_1 on *LCLC* CPT system behavior, based on the approaches covered in Chapter 3, the two-port

network model of the capacitive coupler was simulated using a PSIM platform (PowerSim, Inc.). The capacitive voltage-dependent current source I_1 at the primary side of the coupler (Fig. 4.2) was generated as shown in Fig. 4.5a. There, an auxiliary capacitor, which emulates the coupling capacitor C_M, was exposed to the voltage V_2, and its current was replicated by a voltage-dependent current source to create I_1. Similarly, the capacitive voltage-dependent current source I_2 on the secondary side of the coupler (Fig. 4.2) was generated by replicating the current of another auxiliary coupling capacitor C_M which was exposed to the voltage V_1. In addition, to further verify the analysis and observations made in Section 4.2, a continuous-time simulation model of a variable inductance was designed in an approach similar to the one described in Chapter 2. The model, illustrated in Fig. 4.5b, comprises dependent voltage and current sources, which emulate a non-linear transformer, loaded by some reference inductor L_{ref}. The relationship between the voltages and the currents at the transformer's terminals are defined by the following relationships:

$$\begin{aligned} V_1 &= V_2 K_{ind} \\ I_2 &= I_1 \end{aligned}, \tag{4.15}$$

where K_{ind} is a variable transformer's ratio. From (4.15), the impedance of the inductor L_{ref}, reflected to the primary side, is found as follows:

$$\begin{cases} Z_L = j\omega L = \dfrac{V_1}{I_1} = \dfrac{V_2 K_{ind}}{I_2} \\ Z_{Lref} = j\omega L_{ref} = \dfrac{V_2}{I_2} \end{cases} \Rightarrow Z_L = Z_{Lref} K_{ind}, \tag{4.16}$$

where Z_L is the impedance measured at the transformer's primary. Therefore, the inductor's value, reflected to the primary side is obtained to be:

$$L = K_{ind} L_{ref}, \tag{4.17}$$

To simplify control over the variable inductor, the inductance of L_{ref} was set to 1H. In this case, the effective inductance that was reflected to the primary of the transformer (terminals L+ and L- in Fig. 4.5b) was set by the transformer's ratio K_{ind}.

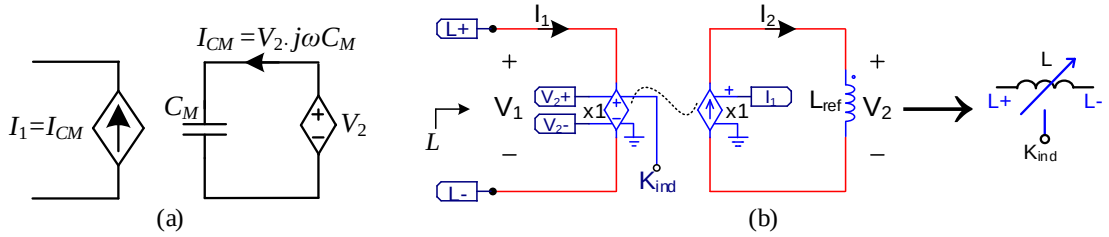

Fig. 4.5 Simulation-compatible models in a PSIM platform: (a) Capacitive coupler; (b) Continuous-time variable inductor.

With a two-port capacitive coupler model of Fig. 5a and continuous-time behavioral model of a variable inductor (Fig. 4.5b), a cycle-by-cycle simulation test bench for an *LCLC*-compensated capacitive WPT system was constructed, as shown in Fig. 4.6. It was assumed that the coupling capacitance C_M was negligible compared to the values of C_1^* and C_2^* (see Fig. 4.1). The simulation model was fed from 10 V, i.e., V_P toggles between -10 and 10 V, the operating frequency is f_{sw} =1.5 MHz, and the load resistance is 10 Ω. Based on the outlines that were established earlier in the analysis in Section 4.2, to guarantee ZVS conditions over the entire coupling range, L_1 was calculated to be 59.2 µH, and the rest of the compensation networks' values were L_{f1}= L_{f2}=1.25 µH, C_{f1} =C_{f2} =9 nF, and L_2=59.2 µH, C_1 =C_2 =190 pF.

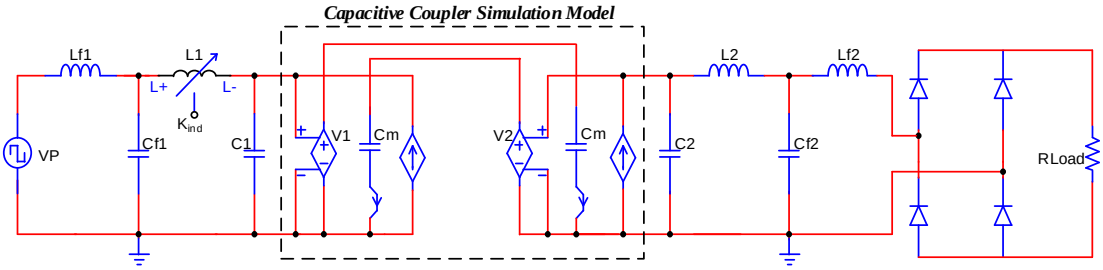

Fig. 4.6 Schematic simulation test bench of the *LCLC* WPT system with a two-port capacitive coupler model and variable inductor on the primary side.

The first set of simulations was carried out by varying the coupling capacitance of the capacitive coupler from 2 pF up to 7 pF. Fig. 4.7a shows the primary side voltage V_P, whereas the current I_{Lf1} for the minimum and the maximum coupling capacitances is shown in Fig. 4.7b and Fig. 4.7c, respectively. It can be seen that for both cases, ZVS is obtained. The current at turn-off for 2 pF is 1.2 A, whereas it is 0.2 A for 7 pF. The second set of measurements was carried out while adjusting the inductor L_1 over different values of C_M to obtain a constant turn-off current of I_{sw} =0.2 A. This is according to the soft-switching analysis presented in Section 4.2. The results for these simulations are summarized in Table II. Fig. 4.7d shows the simulation waveform of I_{Lf1} for a coupling capacitance of 2 pF, while L_1 is set to 60.3 µH (see Table II).

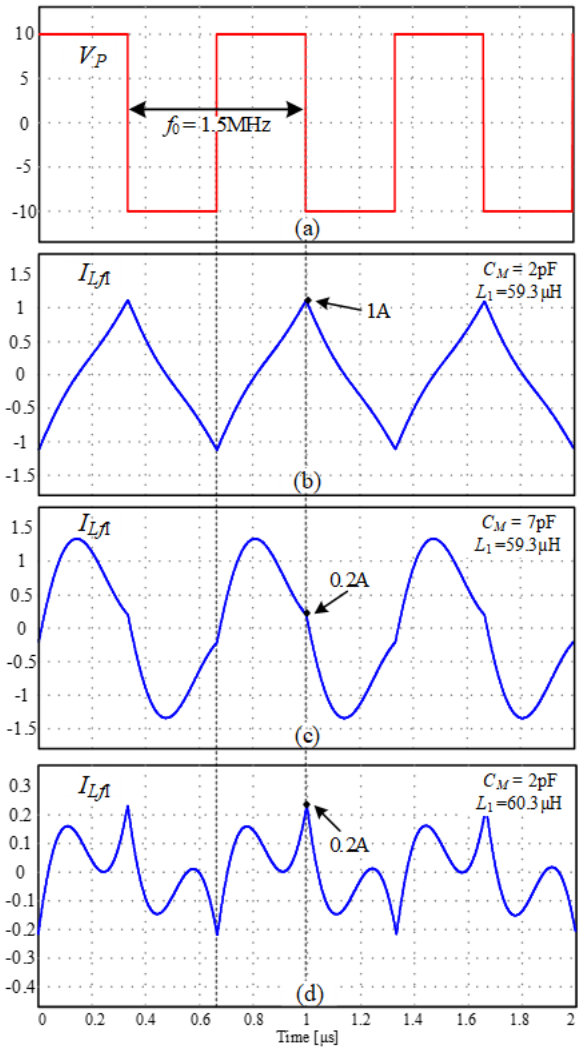

Fig. 4.7 Simulation waveforms on the primary side demonstrating ZVS: (a) voltage V_P, (b) current I_{Lf1} for C_M=2 pF and L_1=59.3 µH, (c) current I_{Lf1} for C_M=7 pF and L_1=59.3 µH, and (d) current I_{Lf1} for C_M=2 pF and L_1=60.3 µH.

TABLE II ADJUSTED INDUCTOR L_1 VALUES TO OBTAIN SOFT-SWITCHING AT CONSTANT CURRENT FOR VARIOUS C_M.

C_M [pF]	**2**	**3**	**4**	**5**	**6**	**7**
L_1 [µH]	60.3	60.2	60.1	59.9	59.6	59.2
I_{sw} [A] Simulation	0.2	0.2	0.2	0.2	0.2	0.2
V_{out} [V]	2.5	3.8	5.1	6.4	7.6	8.8

Fig. 4.8 depicts the switching current, I_{sw}, as a function of the capacitive coupling C_M obtained analytically and by simulation. The simulation results verify that the switching current decreases when increasing the coupling capacitance, as predicted by the theoretical analysis.

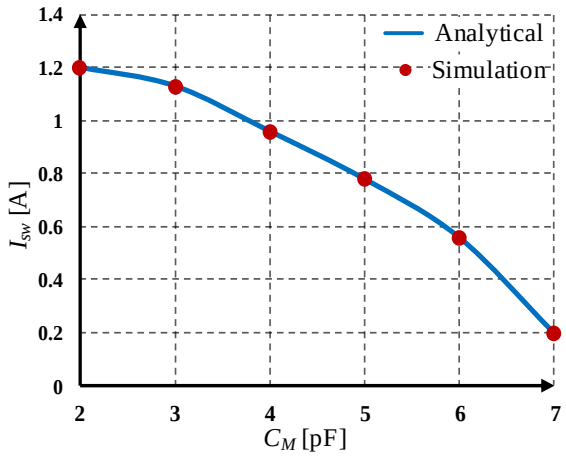

Fig. 4.8 The switching current, I_{sw}, as a function of the capacitive coupling (air gap).

4.4 Experimental Verification

To validate and examine the theoretical predictions, an experimental *LCLC*-capacitive WPT prototype was constructed (Fig. 4.9). The capacitive coupler was designed symmetrically with four copper plates, where each plate is 25x25 cm. To achieve more degrees of freedom throughout the experiments, based on prior articles reported in [110]-[112], a variable inductance was designed for L_1. The realized custom-designed variable inductor comprises an *E*-core type ETD49-3F3 magnetic element (discussed in detail in Section 5.4.1). All other inductors of the prototype were constructed with a litz wire wrapped on an air core. High-voltage multilayer SMD ceramic capacitors were used in parallel to form the matching capacitors. The full-bridge inverter was realized with GaN power modules that were operable at several MHz [103], and the gate drive control signals for the full-bridge were generated using a DE0-Nano-Altera Cyclone IV FPGA [113], at an operating frequency of $f_r \approx 1.5$ MHz. The overall experimental prototype parameters and values are summarized in Table III.

TABLE III EXPERIMENTAL PROTOTYPE SPECIFICATIONS AND PARAMETERS

Parameter	***Design Value***
Input voltage V_{in}	10 V
Coupling plates	25x25 cm
Full-bridge transistors	LMG5200
Operating frequency f_r	1.5 MHz
Load resistance R_{Load}	10 Ω
Lf_1 , Lf_2	1.25 µH
L_1 , L_2	40-62 µH, 60 µH
Cf_1 , Cf_2	9 nF
C_1 , C_2	190 pF
C_M / *Air-Gap*	~ 2-7 pF / 35-120 mm

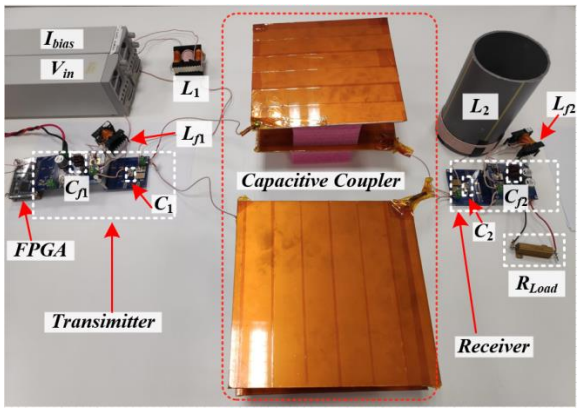

Fig. 4.9 Experimental setup of an *LCLC*-compensated capacitive WPT prototype.

The first step of the experimental validation was carried out by characterizing the inductance of the variable inductor as a function of the bias current. Fig. 4.10 shows the measured results for varying the bias current in the range of 0.3 to 0.5 A, which provides a 1.5X inductance variation covering the required tuning range, as summarized in Table I. It should be noted that to obtain the desired inductance for L_1 throughout the experiments, I_{Bias} was manually regulated by a power supply.

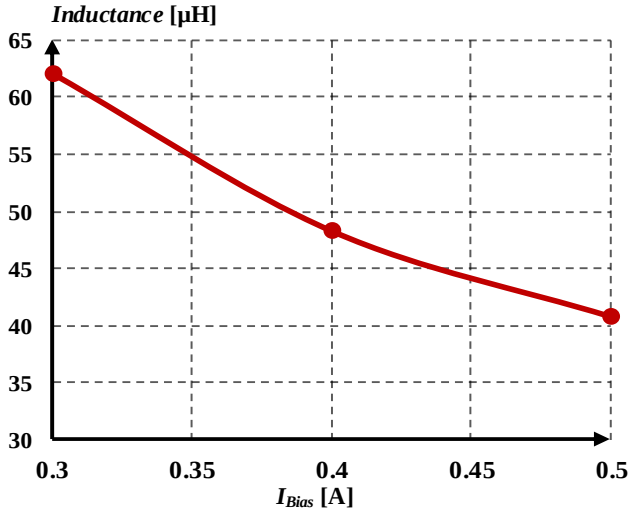

Fig. 4.10 Inductance of the variable inductor L_1 as a function of the bias current.

Next, the inductor L_1 was adjusted to satisfy ZVS conditions over the entire coupling range, that is, adjusting L_1 according to the highest C_M (7 pF). Fig. 4.11 shows experimental waveforms of the primary side voltage V_P and current I_{Lf1} for two different coupling capacitances (2 pF and 7 pF). As can be observed, in both cases, ZVS is obtained. In the conditions for 2 pF, the current at turn-off is 1 A, whereas it is 0.2 A for 7 pF. To further validate the soft-switching analysis, by adjusting the inductor L_1 according to the realtionships given in (4.14), the current at turn-off was calibrated to be in the vicinty of 0.2 A over the entire coupling operating range. The resulting

inductor L_1 values for the entire given C_M range were as summarized in Table II. Fig. 4.12 depicts experimental waveforms of the primary for $C_M \approx 2$ pF, while $L_1 = 60.3$ µH. As can be observed, the soft-switching conditions are satisfied such that the current at turn-off $I_{sw} \approx 0.2$ A. The experimental results tightly follow the results obtained by the simulations in Section 4.3, as well as the theoretical predictions.

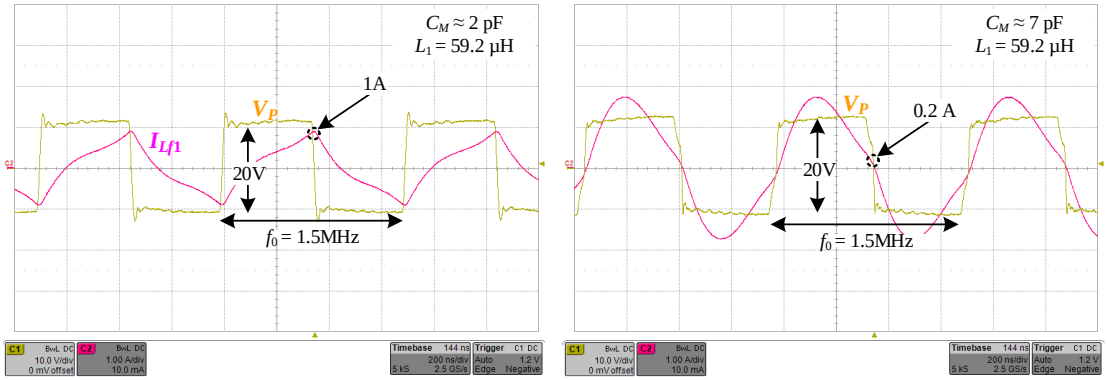

(a) (b)

Fig. 4.11 Waveforms of the primary side voltage V_P (yellow curve – 10V/div) and current I_{Lf1} (pink curve – 1A/div) for $L_1 = 59.2$ µH: (a) $C_M \approx 2$ pF, and (b) $C_M \approx 7$ pF. [Time scale 200ns/div.

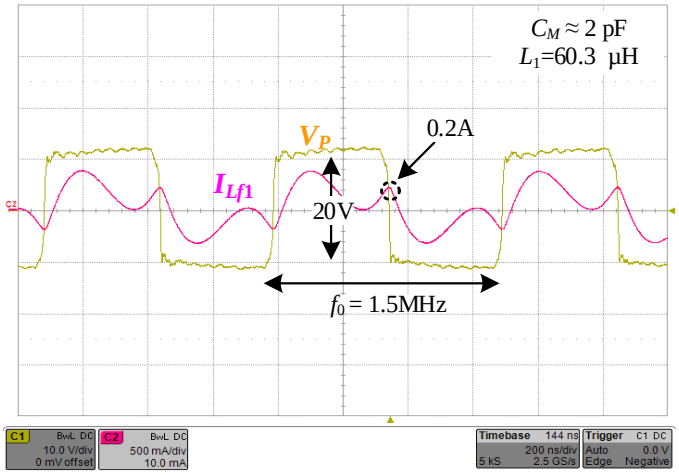

Fig. 4.12 Experimental waveforms of the primary side voltage V_P (yellow curve – 10V/div) and current I_{Lf1} (pink curve – current scale 0.5A/div) for $C_M \approx 2$ pF and $L_1 = 60.3$ µH. Time scale 200ns/div.

CHAPTER 5:
Multi-Loop Control for Power Transfer Regulation in Capacitive Wireless Systems by Means of Variable Matching Networks

5.1 Introduction

Several methods to reduce the effects of components and medium variations of WPT systems have been proposed for general power transfer, which can also be adapted to CPT [60],[61],[78],[82],[114]-[116] such as: frequency tuning, compensation networks impedance matching, and post-regulation DC-DC conversion. In the frequency tuning approach, the operating frequency is adjusted to track the resonant frequency. This results in optimal operating conditions [83],[84],[115]; however, the allowed frequency range for energy transfer is quite narrow, for example at 6.78 MHz operation, the frequency band is ±15 kHz [85]. Thus, for distance, misalignment, and load variations, this solution alone does not accommodate power transfer regulation. In [84], utilization of frequency adjustment in capacitive WPT to account for changes in the capacitive medium capacitance has been discussed. There, the resulting range compensation is quite narrow and requires a relatively wide frequency range. This poses a limitation on the design of the system hardware in terms of the magnetics and other components which translates into a rather bulky system overall. In impedance matching methods, the resonant inductor and capacitor can be adjusted at a fixed frequency [86],[87]. Thus, the output voltage/current can be regulated by actively adjusting the matching network impedance [61]-[63]. The latter provides flexibility for regulating the transferred power to the load, but comes at the cost of potential additional control circuitry and potential degradation of the overall efficiency [62],[63]. It should be noted that although existing closed-loop methods enable some system variations to be overcome and the power delivery range (power levels and distance) to be extended, a single control method is not sufficient to guarantee reliable operation of WPT systems. On the topic of magnetic field-based WPT and, in particular, magnetic resonance, combined control methods have been investigated [82],[89],[117]; however, a closed-form control mechanism for CPT has not been addressed hitherto. It would be extremely beneficial if a multi-loop controller for capacitive-based WPT systems that compensates for the variations of multiple cross-coupling interactions between the transmitting and receiving sides, electrical circuits, and medium characteristics is utilized.

Therefore, the objective of this chapter is to introduce an adaptive multi-loop controller for CPT technology that compensates on-the-fly for variations in the source and load circuits, coupling interface (distance and/or alignment), and matching networks, as detailed in Fig. 5.1. The new control approach effectively disengages the

power delivery capabilities from drifts or variations, which enables spatial freedom of the transferred energy to the receiving side. It relies on continuous tuning of the operating frequency to the resonant one, and adjusts both the transmitter's and receiver's matching networks such that the best power transfer conditions are obtained for any given combination of distance, displacement misalignment, or component values. It is a further objective of this chapter to present a tuned network realization that is based on a variable inductor, i.e., it is not based on relays or semiconductor switches and, therefore, enables continuous self-tuned impedance matching.

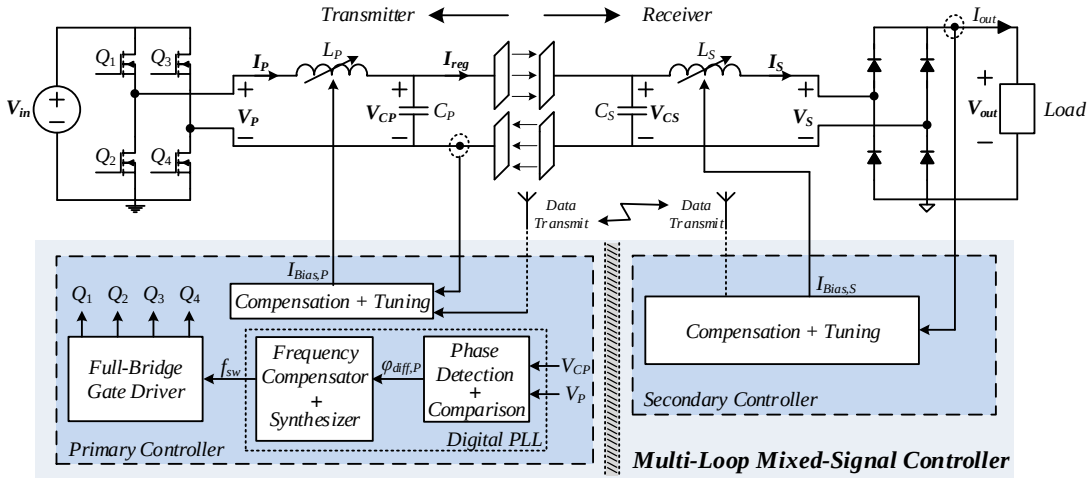

Fig. 5.1 Simplified schematic diagram of a double-sided *LC* capacitive WPT system with an adaptive multi-loop controller.

5.2 Closed-Loop Tuning of a Capacitive WPT System

The principle of operation of the adaptive multi-loop controller is described here through a resonant double-sided *LC* matching network [37],[48], as delineated in Fig. 5.1. It should be emphasized, however, that the core of the control algorithm is applicable for any CPT system, and with minor modifications to any resonant-based WPT method. To establish definitions that are used throughout the chapter and to simplify some of the topology intricate features (e.g., dynamic behavior), the following subsection briefly reviews the double-sided *LC* resonant converter configuration.

5.2.1 Double-sided *LC* matching network

The equivalent electrical representation of the capacitive-based medium is shown in Fig. 5.2. There, C_M is the equivalent mutual coupling capacitance, and C_{M1} and C_{M2} are the self-capacitances of the coupling plates [37],[47],[52],[55]. The system is driven by a full-bridge inverter on the primary side, and the load is fed via a diode rectifier that is

connected to the secondary's network. Provided that the self-capacitances and the mutual coupling capacitance C_M are lower than the total parallel matching capacitances C_P and C_S [37],[48], and the drive frequency, f_{sw}, is near the matching networks' resonant frequency (i.e., $f_0 = 1/(2\pi\sqrt{L_P C_P}) = 1/(2\pi\sqrt{L_S C_S})$, then the currents as well as voltages of the reactive elements are virtually sinusoidal [99][100]. This is because high-Q operation is naturally facilitated, as the output impedance of the network in the primary side is relatively high. In [1],[6],[37], it was established that when the resonant operation is satisfied, the primary current, I_P, depends on the output voltage, and the secondary current, I_S, depends on the input voltage and, thus, with the aid of system parameters, the currents can be expressed as

$$I_P = \underbrace{\frac{\omega_0 C_P C_S}{C_M}}_{G} V_S \quad ; \quad I_S = \underbrace{\frac{\omega_0 C_P C_S}{C_M}}_{G} V_P \,, \tag{5.1}$$

where ω_0 is the angular resonant frequency, and V_P and V_S are the voltages of the primary and secondary, respectively. Typical waveforms of this CPT system are shown in Fig. 5.3. As described, while the primary and secondary voltages V_P and V_S are square waves, the currents are sinusoidal due to high-Q operation of the circuit. Since a full-bridge inverter is used at the front end, the primary voltage V_P toggles between V_{in} and $-V_{in}$. It can be also seen, that for both the primary and secondary sides, the current is in phase with the voltage, whereas the secondary voltage V_S lags the primary voltage V_P by 90º.

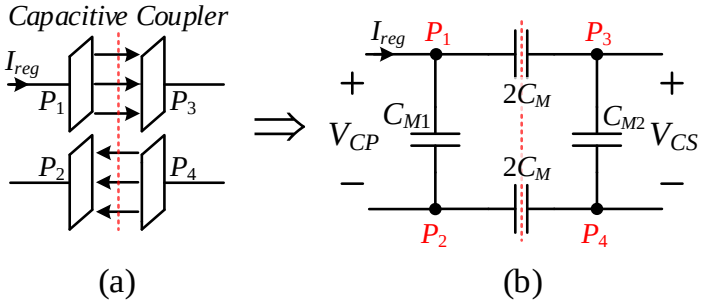

Fig. 5.2 Capacitive medium: (a) Simplified mechanical illustration. (b) Equivalent capacitance lumped model.

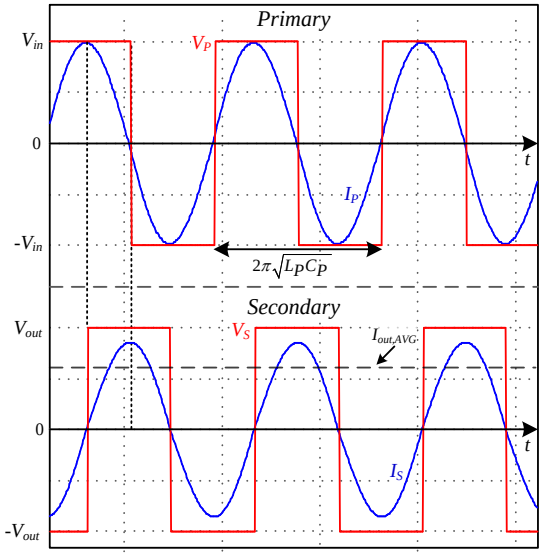

Fig. 5.3 Typical current and voltage waveforms of a *LC* capacitive WPT configuration: upper signals – primary, bottom signals – secondary.

From (5.1), it can be seen that the double-sided *LC* CPT system can be described by a two-port network with gyrator characteristics (and as discussed in detail in the previous chapters), with a trans-conductance gain *G*. This implies that the dynamic behavior for the output side of the system can be characterized as a voltage-dependent current source, I_{out}, which represents the rectified current of I_S as illustrated in Fig. 5.4. It should be noted that a detailed derivation of the network relationship of the circuit, as well as the existence criteria of gyrator conversion have been thoroughly described and can be found in [1],[6]. Therefore, only the essential in-context details have been brought up here in order to establish the foundations for power regulation control.

Employing a fundamental harmonics approximation method [99] on (5.1), the average value of the output current I_{out} is expressed as a function of the input voltage V_{in} as follows:

$$I_{out,AVG} = \frac{8}{\pi^2}\frac{\omega_0 C_P C_S}{C_M} V_{in}\,; \tag{5.2}$$

thus, the average output power P_{out} can be expressed as:

$$P_{out} = \left(\frac{8}{\pi^2}\frac{\omega_0 C_P C_S}{C_M} V_{in}\right)^2 R_{Load}\,. \tag{5.3}$$

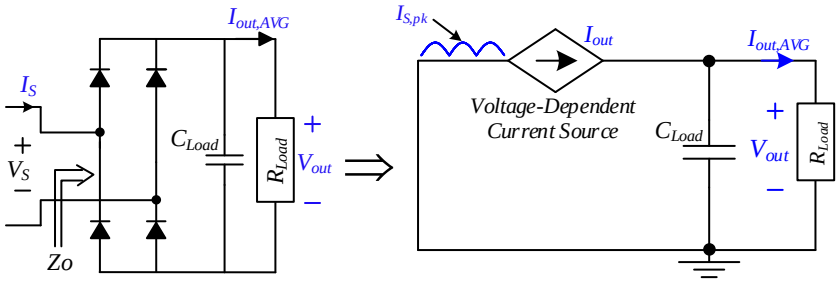

Fig. 5.4 Simplified behavioral model for the output side of the CPT system.

5.2.2 Controller operation

Following the analysis and observations made in the previous subsection, an adaptive controller that monitors, tunes, and enables to continuously deliver constant current to the receiving side is addressed. Power regulation is facilitated by three major control loops, as shown in Fig. 5.1, with two control loops on the primary side, while a third loop is located at the secondary circuit. The control loops are distinguished by their control objectives and bandwidth requirements, such that the operating characteristics of the WPT system are satisfied. In structure, the first loop resembles a digital phase-locked loop (DPLL) that synthesizes a switching frequency, f_{sw}, which continuously follows the resonant frequency, $f_{0,}$ even under variations of the system parameters. In this *LC* configuration, this self-driving concept ensures that the power conversion characteristics of the matching networks are optimized. Compensating for changes in the coupling medium requires variation in the drive frequency off the specific optimized point and correcting the network parameters accordingly. This can be achieved by adjusting the network's inductor, capacitor, or both. In this study, an approach based on a variable inductor is employed. The second control loop comprises a current compensator and a tuning unit (current driver, as will be detailed later) that adjusts the inductance value of L_P such that a constant current is regulated to the capacitive plates. This transforms the primary circuit into a self-tuned architecture in which the drive frequency tracks the resonant frequency on-the-fly, and the transmitted power is regulated by the resonant network's characteristics. A third compensation loop, located on the receiver side, is a tuning unit that adjusts the inductance value of the secondary side inductance, L_S, according to the desired output current (as well as power). It should be emphasized that, in general, controlling only one parameter may suffice for constant power delivery for static operations; however, to achieve more spatial freedom even for extreme medium and load variations, all three loops are required.

A high-level view of the tuning procedure utilizing the control loops is illustrated in the flowchart in Fig. 5.5. Upon initiation of the tuning procedure, a default set of pre-loaded values are used to determine the switching frequency f_{sw}, and the variable inductors L_P and L_S. These values are determined by the target operating conditions of the system. The adaptive tuning operation is performed independently per feedback loop, with its respected objective and rate. The inner feedback loop applies frequency tuning. There, the switching frequency to drive the full bridge, f_{sw}, is being varied by the DPLL unit to match the resonant frequency of the circuit f_0. This is facilitated by measuring the voltages V_P and V_{CP} (Fig. 5.1), extracting the phase difference between them, and adjusting f_{sw} until the phase difference between the signals reaches 90º. In the case that the detected phase difference between the signals is not 90º, an error signal is generated to the DPLL frequency synthesizer, which in turn generates a new switching frequency until $f_{sw}=f_0$.

The next stage of the tuning operation is facilitated by another feedback loop located on the secondary (receiver) side. In this loop, the inductance value L_S of the secondary's matching network is adjusted according to the operating resonant frequency of the primary side to maximize the energy transfer to the load. This is done by sensing the output current and adjusting L_S according to the current relationships in (5.1) and (5.2). This variation of the inductor value is realized by a current driver that applies dc bias to non-gapped side windings of the inductor, as previously described in [111],41X].

In the third stage of the tuning operation, the plate current I_{reg} (Fig. 5.1) from the primary circuit is sensed and compared to a target/reference one, which is defined by the information from the receiving side. The correction signal that is generated is used to vary the inductance L_P through a bias winding until the required current is achieved. Due to the variation in the inductance value, the resonant characteristics of the system change, and potentially move the system out of its optimized transfer conditions. As a result, the frequency tracking loop needs to search again and lock the switching frequency into the resonant frequency. Therefore, to satisfy proper operation of the multiple feedbacks, and to allow each feedback loop to converge with reasonable dynamics while being virtually decoupled one from another, the compensators are designed with descending bandwidth order. Utilizing this approach, employed in many multiple loop compensation schemes, assures that the faster loop is virtually transparent to its following and by doing so, significantly simplifies the system dynamics and complexity of the compensators. As a result, the interaction, or interference, between

feedbacks is alleviated. The frequency tracking loop (of the primary side) is designed to pair with the highest bandwidth within the controller, i.e., it responds the fastest among the multiple control loops. The second responding loop is the adjustment of the secondary's matching network, as it receives its signal with a defined frequency of the primary. The current/power regulation loop is designed with the slowest bandwidth of the three to assure that once the energy level is set, it is with the optimized transfer conditions given the network parameters and medium settings. The analysis, derivations, and in-detail description of the multi-feedback loops are provided next.

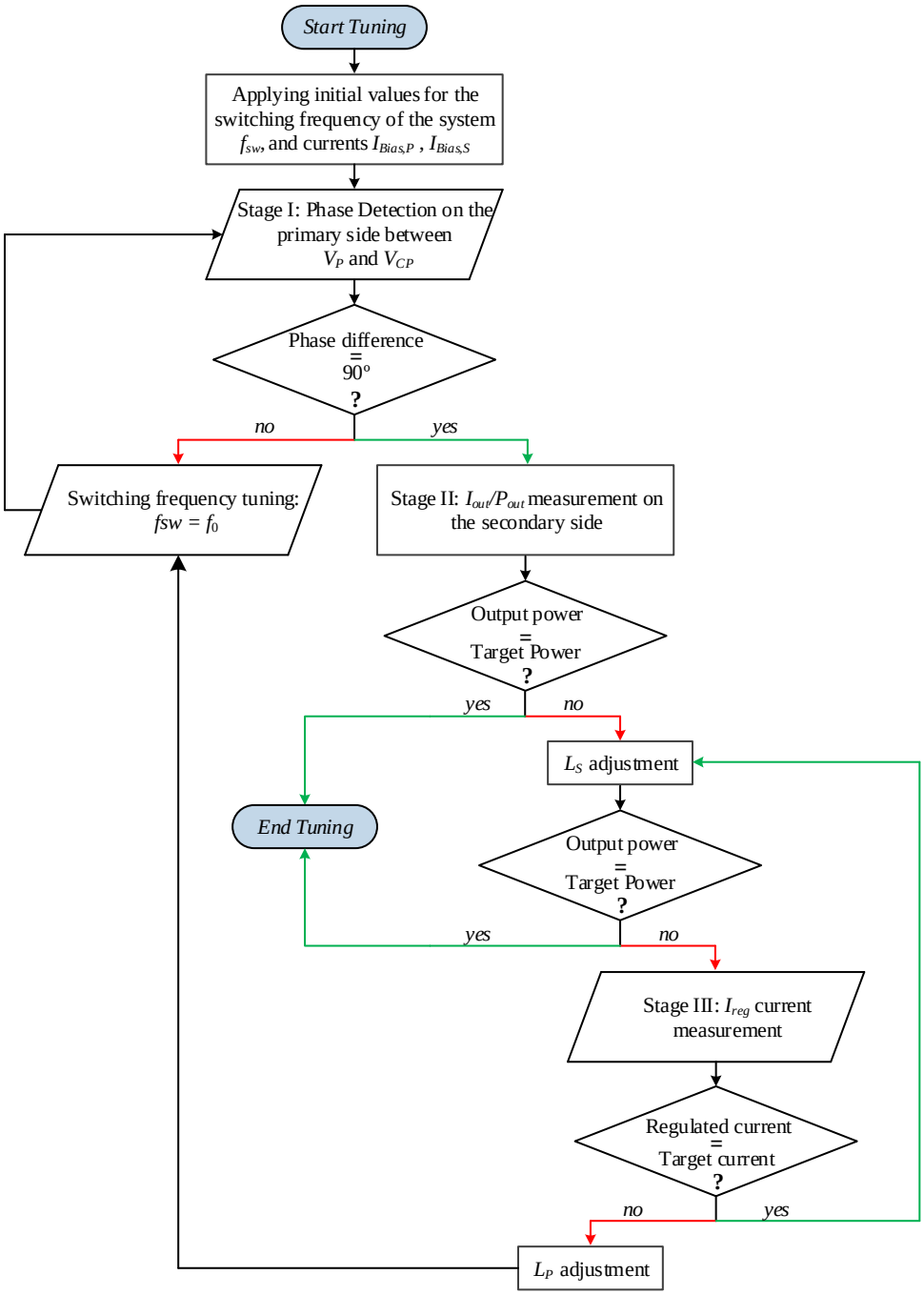

Fig. 5.5 Flowchart of the controller's tuning procedure.

5.3 Controller Architecture

Following the high-level description of the control algorithm given in the previous section, simplified *functional diagrams* that describe the signal flow and behavior of this self-adjusted, self-tuned, system are depicted in Fig. 5.6. The diagrams comprise both linear and non-linear transfer functions to reflect the specific operation of each "transformation unit" (i.e. "block") [110]. It should be emphasized that throughout the functional derivations, small-signal transfer functions are denoted by small letters. The diagram of the control scheme of the primary circuit includes two major loops to satisfy current sourcing behavior to the transfer plates (Fig. 5.6a). A third, independent loop is located on the secondary side to adjust the receiving network to regulate the output current. In addition, for both the primary and secondary circuits, the bias driver of the variable inductors is designed as a closed feedback loop configuration to maintain a forced current control. This enables the order of the outer feedback loop to be reduced, making it simpler to stabilize the overall system. By employing a self-calibrating frequency loop and adjusting the system parameters, regulation of the primary's output current, I_{reg}, can be achieved at the same time that the system is kept at resonance (while soft-switching conditions are met).

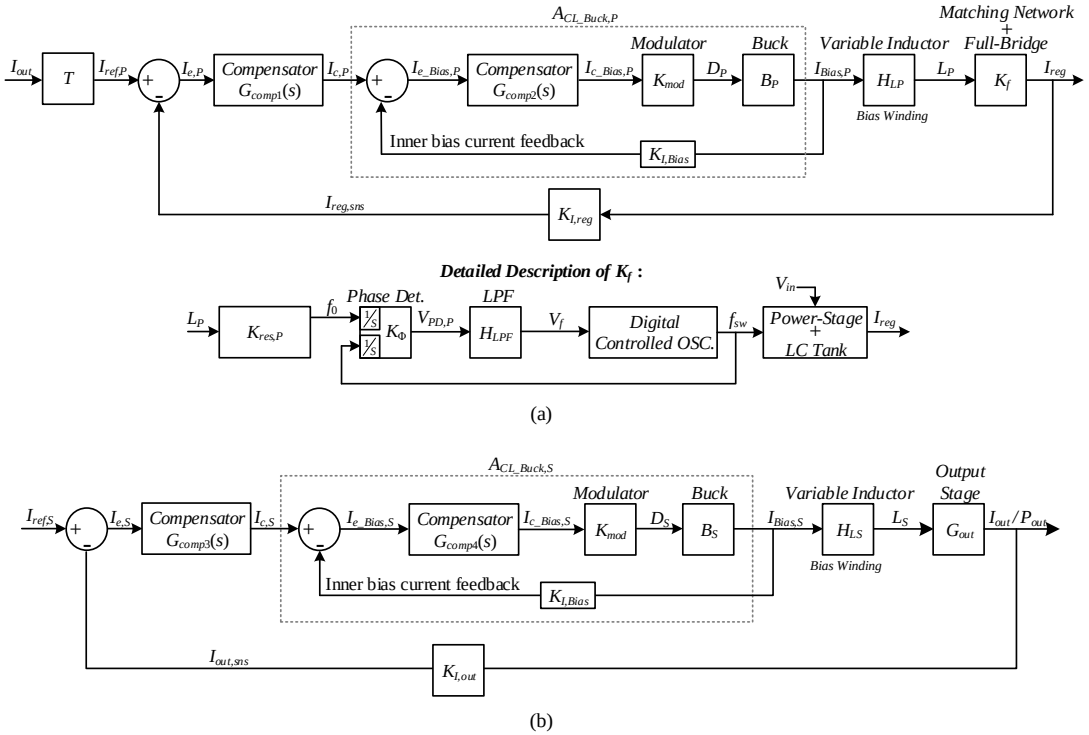

Fig. 5.6 Simplified functional signal flow diagrams of the multi-feedback controller: (a) Primary side control loops, (b) Secondary side control loops.

5.3.1 Primary side control loops

Starting from the left side of Fig. 5.6a, the output current is translated to a reference current level, $I_{ref,P}$, which is a proportional representation of the required regulated current from the primary to the secondary. $I_{c,P}$ represents the correction signal generated by the current compensator, and $I_{e\_Bias,P}$ is the error signal of the inner bias current loop. K_{mod} stands for the modulator's gain, i.e., bias current correction signal, $I_{c\_Bias,P}$ to duty-cycle of the bias current driver. The bias driver in this work has been realized by a buck converter, and its transfer function is represented in the block diagrams by B_P. The bias current for the inductor L_P can be expressed as:

$$I_{Bias,P} = D_P B_P(s) = \frac{D_P V_{Buck}}{sL_{Bias} + R_{DCR}}, \tag{5.4}$$

where L_{Bias} is the inductance value of the bias winding, R_{DCR} is the dc resistance of the inductor, and D_P and V_{Buck} are the duty-cycle and the input voltage of the buck converter, respectively. After linearization, the small-signal transfer function between the duty-cycle and the inductor current $b_P(s)$ is expressed as:

$$b_P(s) = \frac{i_{Bias,P}(s)}{d_P} = \frac{V_{Buck}}{sL_{Bias} + R_{DCR}}, \tag{5.5}$$

where $i_{Bias,P}$ is the small-signal bias current and d_P is the duty-cycle perturbation. Thus, the closed-loop transfer function of the buck converter is:

$$A_{CL\_Buck,P}(s) = \frac{i_{Bias,P}(s)}{i_{c,P}(s)} = \frac{G_{comp2}(s)K_{mod}b_P(s)}{1 + K_{I,Bias}G_{comp2}(s)K_{mod}b_P(s)}, \tag{5.6}$$

where $G_{comp2}(s)$ is the transfer function of the inner compensator and $K_{I,Bias}$ is the gain due to the bias current sensing [110],[118]. By neglecting R_{DCR} and by assuming that the compensator has been designed properly to meet both phase margin and loop gain bandwidth, (5.6) can be further rearranged and simplified to a first order system [110]:

$$A_{CL\_Buck,P}(s) = \frac{1/K_{I,Bias}}{1 + s/\omega_{Buck,P}} \quad ; \quad \omega_{Buck,P} = \frac{K_{I,Bias}K_{p2}K_{mod}}{L_{Bias}}, \tag{5.7}$$

where K_{p2} is the gain due to the compensator. (5.7) implies that for the frequency range $\omega < \omega_{Buck,P}$, the inner current feedback has transformed the bias buck converter (from error signal to bias current) from a first-order system to a zero-order system.

H_{LP} represents the bias winding such that the relationship between the bias current and the primary side inductance is:

$$L_P = H_{LP(I_{Bias,P})}. \tag{5.8}$$

The relationship of $H_{LP}(I_{Bias,P})$ can be obtained by experimental measurements, advanced simulation tools such as Maxwell-Ansys, or analytical analysis which is discussed in detail in Section 5.4.1. Local linearization around the operating point determines the non-linear small-signal response of H_{LP} as follows:

$$h_{LP} = \frac{dL_P(I_{Bias,P})}{dI_{Bias,P}} = \frac{H_{LP}(I_{Bias,P0}) - H_{LP}(I_{Bias,P0} + \Delta I_{Bias,P})}{\Delta I_{Bias,P}}, \tag{5.9}$$

where $I_{Bias,P0}$ is the nearest measure value of the bias current for a given operating point, and $\Delta I_{bias,P}$ is the increment between the two nearest measured values of the bias current around the operating point. Finally, K_f is the response of the matching network combined with the power-stage to the variable inductor generated by H_{LP} (the ratio of the regulated current I_{reg} to a change of the resonant characteristics).

The bottom block diagram in Fig. 5.6a details the transfer characteristics of K_f. The output of H_{LP} dictates the resonant frequency f_0 of the CPT system such that:

$$K_{res,P}(L_P) = f_0 = \frac{1}{2\pi\sqrt{\underbrace{H_{LP}(I_{Bias,P})}_{L_P} C_P}}. \tag{5.10}$$

Considering that $H_{LP}(I_{Bias})$ as constant, due to the relatively slow correction speed of the inductance value, the derivative of the large-signal $K_{res,P}(L_P)$ around the operating point yields the small-signal transfer function of the resonant tank [110]:

$$k_{res,P} = \left.\frac{df_0}{dL_P}\right|_{L_P(I_{Bias,P0})} = -\frac{1}{2L_{P0}} f_0, \tag{5.11}$$

where L_{P0} is the primary's resonant inductor value around the operating point.

Assuming that the frequency tuning is the fastest control loop within the system (as prescribed by the loop settings earlier), then f_0 is continuously compared to the switching frequency f_{sw} of the full bridge to guarantee that $f_{sw}=f_0$. K_Φ represents the gain of the phase detector; consequently, the phase detector can be described as a module that includes two integrators at the input that translates frequencies into phases and a gain block. The outcome of the phase detection operation, $V_{PD,P}$, can be expressed as:

$$V_{PD,P} = K_\Phi \varphi_{diff,P} = \frac{V_{DD}}{\pi} \varphi_{diff,P}, \tag{5.12}$$

where V_{DD} is the supply voltage of the phase detector, and $\varphi_{diff,P}$ is the phase difference between the target resonant frequency and the drive switching frequency signals (which is obtained by the signals V_P and V_{CP}, as discussed in Section 5.2.2). $V_{PD,P}$, which represents a proportional phase mismatch between the inputs of the phase detector for

every switching cycle of the system, is filtered by a lag-lead low-pass filter (LPF) network that is represented in the continuous domain as:

$$H_{LPF}(s) = \frac{1+sCR_2}{1+sC(R_1+R_2)}, \tag{5.13}$$

which simplifies the stability of DPLL [119].

The voltage V_f is translated by a digitally controlled oscillator (DCO) unit to a drive frequency for the power stage combined with the *LC* tank, which, in turn, generates the required I_{reg}. Taking into account the gyrator transfer characteristics of the system as discussed in Section 5.2.1, and after some manipulations, the regulated current to the capacitive coupler can be expressed as follows:

$$I_{reg} = 2\pi f_0 C_P V_P . \tag{5.14}$$

Finally, the transfer function of the outer regulated current loop can be expressed as:

$$A_{CL\_P}(s) = \frac{i_{reg}(s)}{i_{ref,P}(s)} = \frac{G_{comp1}(s)A_{CL\_Buck,P}(s)h_{LP}K_f}{1+K_{I,reg}G_{comp1}(s)A_{CL\_Buck,P}(s)h_{LP}K_f}, \tag{5.15}$$

where $G_{comp1}(s)$ is the transfer function of the outer compensator, and $K_{I,reg}$ is the gain due to the regulated current sensing [120]. Under the bandwidth settings of the feedback loops as prescribed earlier, where the inner frequency-tuning loop has sufficiently faster response compared to the outer current regulation loop, i.e., L_P is continuously adjusted under resonant conditions of the network, the closed-loop transfer function of (5.15) can be simplified to a first-order system and can be expressed as:

$$A_{CL\_P}(s) = \frac{\frac{1}{s}K_{P1}A_{CL\_Buck,P}(s)h_{LP}K_f}{1+\frac{1}{s}K_{I,reg}K_{P1}A_{CL\_Buck,P(s)}h_{LP}K_f} = \frac{\frac{1}{K_{I,reg}}}{1+\frac{s}{\omega_{CL\_P}}}, \tag{5.16}$$

$$\omega_{CL\_P} = K_{I,reg}K_{P1}A_{CL\_Buck,P}(s)h_{LP}K_f$$

where K_{P1} is the gain due to the outer compensator and ω_{CL_P} determines the bandwidth of the outer current loop.

5.3.2 Secondary side control loops

Fig. 5.6b depicts the functional block diagram of the secondary's control loops. There, similar to the relationships carried out earlier for the primary side, the closed-loop transfer function of the secondary's bias driver, $A_{CL\_S}(s)$, is expressed as:

$$A_{CL\_Buck,S}(s)=\frac{i_{Bias,S}(s)}{i_{c,S}(s)}=\frac{1/K_{I,Bias}}{1+s/\omega_{Buck,S}},\qquad \omega_{Buck,S}=\frac{K_{I,Bias}K_{p4}K_{mod}}{L_{Bias}} \tag{5.17}$$

where K_{p4} is the gain due to the secondary's inner bias current loop compensator. As mentioned earlier, utilizing current-mode control for the bias driver, within the specified current regulator bandwidth $\omega<\omega_{Buck,S}$, the bias current loop dynamics are considered as pure gain. Thus, the overall transfer function of the output current can be expressed as:

$$\begin{aligned}A_{CL\_S}(s)&=\frac{i_{out}(s)}{i_{ref,S}(s)}\\&=\frac{G_{comp3}(s)A_{CL\_Buck,S}(s)h_{LS}G_{out}}{1+K_{I,out}G_{comp3}(s)A_{CL\_Buck,S}(s)h_{LS}G_{out}}\end{aligned}, \tag{5.18}$$

where $G_{comp3}(s)$ is the transfer function of the outer compensator, $K_{I,out}$ is the gain due to the current sensing, and G_{out} is the gain of the output stage. Assuming L_S is continuously adjusted to satisfy the required loading conditions of the output, the closed-loop transfer function of (5.18) can be simplified to a first-order system and can be expressed as:

$$A_{CL\_S}(s)=\frac{\frac{1}{s}K_{P3}A_{CL\_Buck,S}(s)h_{LS}G_{out}}{1+\frac{1}{s}K_{I,out}K_{P3}A_{CL\_Buck,S(s)}h_{LS}G_{out}}=\frac{1/K_{I,out}}{1+s/\omega_{CL\_S}},\qquad \omega_{CL\_S}=K_{I,out}K_{P3}A_{CL\_Buck,S(s)}h_{LS}G_{out} \tag{5.19}$$

where K_{P3} is the gain due to the outer compensator, and ω_{CL_S} determines the bandwidth of the output current loop. From the analyses for the secondary controller, it can be seen that the control architecture for the primary and secondary is practically the same with different control objectives. Once satisfied, this implies that the transmitting and receiving sides are tuned to satisfy the required loading conditions, and the system operates under optimal power transfer conditions since resonant power transfer is inherently imposed through the self-tuning procedure.

5.3.3 System bandwidth selection

To assure reasonable dynamics of the multiple feedback loops, and to assure sufficient decoupling of the multiple feedback loops, as well as steady-state convergence per medium settings, the system's bandwidths are assigned with respect to the transmitter's quality factor, Q, (receiver assumed of similar order), and the target

operating frequency, f_{sw}, of the system. It should be noted that in systems, such as double-sided *LC* with capacitive coupling, the response rate to changes in the control (drive frequency) signal might be rather slow, in the order of tens or hundreds switching cycles. This is since the quality factors are typically very high because of the somewhat open-circuit parallel loading of the networks (the plates terminals), as depicted in Fig. 5.7. The quality factor of the *LC*-based transmitter is a factor of the operating frequency, as well as the resonant components, and can be estimated as:

$$Q = {Z_{CM}(f_{sw})}/{Z_R(f_{sw})}, \tag{5.20}$$

where Z_{CM} represents the reflected equivalent impedance to the primary side, which is primarily determined by the coupler, and Z_R is the impedance of the resonator.

The natural slow response of the network should be taken into consideration in the selection of the system bandwidth and overall response rate. Fortunately, the objective of the control is to maintain a regulated current/power under variations of the capacitive coupling or other components drifts, which are the result of either mechanical movements or changes in environmental conditions that typically vary slowly.

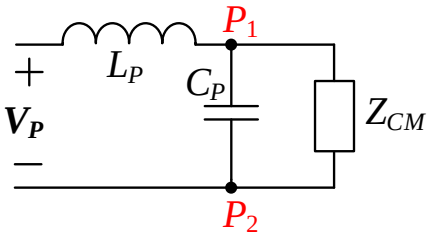

Fig. 5.7 Simplified equivalent circuit of the primary side.

The selection reasoning is as follows; the loop of the fastest bandwidth of the three loops is the DPLL, denoted by BW_1. There, for a given quality factor Q of the resonant networks, and assuming that f_{sw} is locked on f_0, then BW_1 is determined as follows:

$$BW_1 = {f_{sw}}/{2Q}. \tag{5.21}$$

This is set so that the loop has a relatively wide bandwidth, but retains the capability of the resonant network response rate. The secondary's control loop is also a relatively wide bandwidth loop and is set as a fraction of BW_1, typically, in practice, one-third (1/3) to one-tenth (1/10). This is done to assure that the secondary current regulation is carried out on a stable signal, arriving from the primary side. The third, the plate current loop, is set to have a slower response, typically one-ninth (1/9) to one-fiftieth (1/50) of the switching frequency of the system. By doing so, the loops are virtually decoupled,

and the tuning process does not depend on preceding information or data of the system to facilitate closed-loop operation.

5.4 Controller Architecture

5.4.1 Variable inductor

The implementation of variable inductor is inspired by [110]0,[111],[118]. The structure comprises an *E*-core type magnetic element with the primary inductor on the middle, gapped leg, whereas the bias/control windings are formed on the outer, non-gapped legs (Fig. 5.8). If the ac component of the inductor's is small enough so that the permeability change due to the current variations is negligibly small, the inductance value L can be estimated with the aid of several design parameters such as: the number of turns n, air-gap length l_g, and the effective magnetic path length l_e. Hence, the inductance L as a function of the bias current-dependent permeability can be expressed as:

$$L = \frac{n^2 \mu_0 A_e}{l_e} \frac{\mu_r(I_{Bias})}{1 + 2\frac{l_g}{l_e}\mu_r(I_{Bias})}, \tag{5.22}$$

where μ_0 is the air permeability, μ_r is the magnetic core permeability, and A_e is the core area. μ_r depends on the bias current I_{Bias} and can be obtained from either the manufacturer data or by experiment [101],[112]. A simplified expression of μ_r is given by:

$$\mu_r(I_{Bias}) = \frac{\mu_{mi}}{1 + \left(H(I_{Bias}) / H_{\text{pole}}\right)^j}, \tag{5.23}$$

where μ_{mi} is the permeability initial value, i.e., $\mu_{mi} = \mu_r(H = 0)$, H_{pole} is the magnitude of the saturation field, and j sets the permeability slope. The variable H represents magnetic field strength, which is linearly proportional to the bias current. The relationship between H and I_{Bias} is as follows:

$$H(I_{Bias}) = {nI_{Bias}}/{l_e}. \tag{5.24}$$

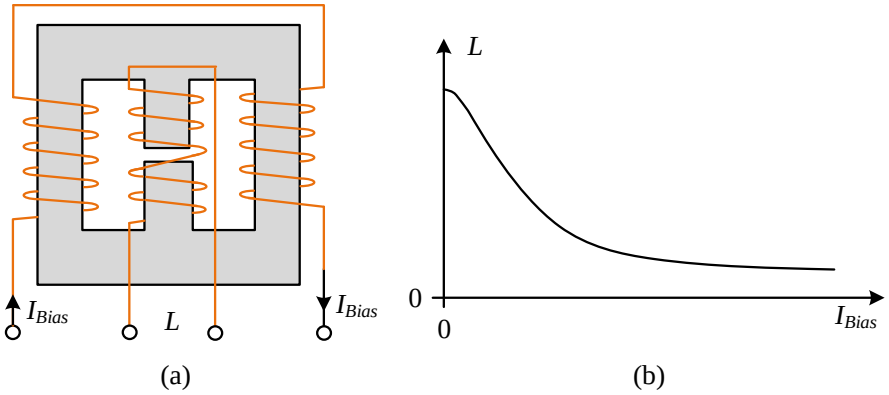

Fig. 5.8 Variable inductor practical implementation, (b) Relationship between the inductance value and the bias current.

5.4.2 Limit-cycle oscillations in digitally controlled resonant converters

A major practical issue that should be considered when designing closed-loop resonant-based WPT systems and, particularly, digitally-controlled resonant WPT are limit-cycle oscillations (LCO). As originally presented in [121], the primary cause for steady-state oscillations is a resolution mismatch of the quantizing units in the controller, i.e., the analog-to-digital converter (ADC) and the DCO (assuming the compensators does not add a quantization error) [121]. In addition to the operating-point dependent gain that exists in resonant converters, the highest sensitivity to gain variations is located around the resonant frequency, a condition that becomes even further emphasized in capacitive WPT systems that operate with very high-quality factors. Since the controller targets the optimal transfer conditions that are obtained at resonance (aside from a slight deviation from the exact target frequency to facilitate ZVS), this calls for extremely sensitive calibration, i.e., a fine-frequency resolution generator at the MHz range to facilitate LCO-free operation. Therefore, to ensure smooth high-frequency drive throughout the operation range (taking into account the worst-case conditions of the highest quality factor), the ADC and DCO units in this study were designed to achieve the required effective acquisition, as well as control resolution such that limit-cycle oscillations are remedied. Fortunately, the slow-response feature of the resonant network due to high-Q aids in this aspect. Since the network takes several cycles to react to changes in the drive frequency, it is utilized as an averaging action. Frequency dithering is embedded to enhance the drive frequency, and to provide an effective frequency (over a few cycles) with finer resolution than the base value.

To determine the existence of LCO in resonant converters, a comparison is carried out between the LSB values (i.e., resolution) of the digitally acquired value by the ADC and the output signal variation due to a one-LSB change of the control [121]-[123]. A necessary condition for no limit-cycles is that the variation of the output ΔS_{out}, due to an LSB change of control is smaller than the ADC resolution Δ_{ADC} [121]:

$$\Delta S_{out} < \Delta_{\mathrm{ADC}} = \frac{V_{\mathrm{ADC}}}{2^{N_{\mathrm{ADC}}}}, \tag{5.25}$$

where V_{ADC} and N_{ADC} are the ADC's reference voltage and number of bits, respectively. Digitally synthesized frequency is normally carried out by timers that are programmed to reset at a desired value, while maintaining a fixed 50% duty ratio [121]. The generated frequency can be expressed as follows:

$$f_{\mathrm{DCO}} = \frac{1}{N_{per} TB}, \tag{5.26}$$

where N_{per} is an integer and TB is the time base of the unit clock. The frequency resolution can be calculated as the LSB change in N_{per}:

$$\Delta f_{\mathrm{DCO}} = \frac{1}{N_{per} TB} - \frac{1}{\left(N_{per} - 1\right) TB} \approx \frac{1}{N_{per}^2 TB} = TB f_{\mathrm{DCO}}^2 . \tag{5.27}$$

From (5.27), it can be well observed that the frequency steps of the DCO are limited by the system clock frequency, and they increase as the square of the operating frequency, i.e., at lower running frequency, the frequency resolution would be finer than what can be achieved at a higher frequency. Since finer resolution than the one obtained by the system DCO is required, an effective fast dynamics and low distortion frequency dithering procedure has been employed as detailed in [124].

5.4.3 Phase detector

The phase detection in this study has been realized as illustrated by Fig. 5.10. Since the voltages of the resonators are significantly higher than the operation voltage levels of the controller and other electronics periphery, the voltages V_P and V_{CP} are scaled down using high-impedance attenuation circuit to voltage levels suitable for logic gates input such as the phase detector unit. Form practical implementation perspective, if a simple resistive divider is used, the input capacitance of the logic gate introduces phase delay between the actual zero-crossing point and the digital signal transition. In the case that the phase shifts of the two measured signals are different (due to different resistive path), a systematical offset exist, and should be calibrated out. Thus, to minimize phase

offset errors, similar voltage scaling should be employed for both signals as much as possible, which might be impractical in high voltage gain systems. At such cases, active attenuation circuits as well as adaptive calibration are required.

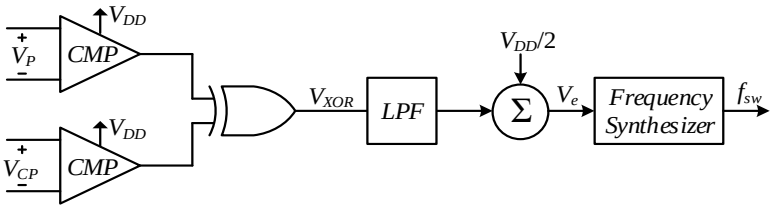

Fig. 5.9 Simplified schematic of the phase-locked-loop: phase detection, filter (and compensation), and frequency synthesizer.

The phase detector is realized by type-I detection circuit, i.e., comparators as digitizers and an exclusive-or operator (XOR) phase comparator. Typical waveforms of the operation are depicted in Fig. 5.10, which shows two cases. Fig. 5.10a exhibits at-resonance operation, with phase difference of 90º and the resulting detector in 50% duty-cycle and averaged output is $V_{DD}/2$ (assuming the voltage supply of logic is V_{DD}). In this case the frequency generated by the synthesizer is stable and fixed. Fig. 5.10b demonstrates a case where the system is not tuned with a duty-ratio of V_{XOR} is 25%. In this case, the output of the filter is lower than $V_{DD}/2$, and the synthesizer varies its frequency until the desired phase difference is obtained and the filter's output is at $V_{DD}/2$.

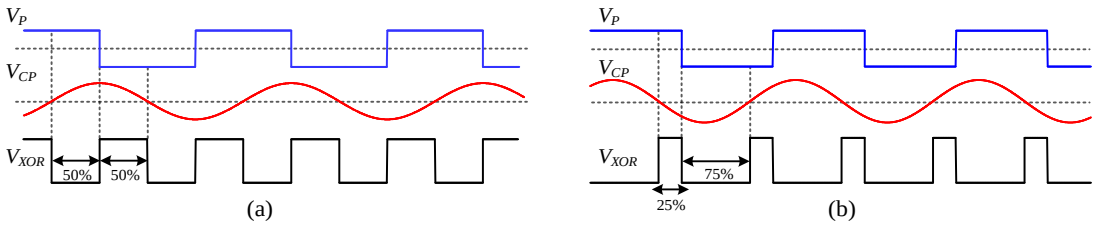

Fig. 5.10 Signals of the phase detector: (a) Tuned CPT system operating in resonance. (b) Example of a non-tuned CPT system reading.

5.4.4 Current-sensing circuitry

The multi mixed-signal controller requires various measurements of the operating conditions in the WPT system. A key measurement of the system is the plates current, I_{reg}, however, this high-frequency current is not trivial to measure and sensing techniques such as current transformer [125] and filter-sense [126] may result in complex sensing circuitry. The current-sensing employed in this study is based on a peak detector mechanism which consists of a simple half wave rectifier configuration as shown in Fig. 5.11. The sensed current converted to a proportional voltage suitable

signal, V_{sns}, by flowing through the resistor R_{sns} [126],[127]. The peak detector is implemented around an operational amplifier to compensate for the voltage drop on the rectifying diode *D*. An active peak detector is employed so that relatively low gain measurement can be obtained (low resistance shunt resistor), and by doing so lowering the gain-bandwidth requirements of the sensor. The time constant of the peak detector is selected approximately ten times the period of the sensed sinusoidal signal to both filter out the ripple, and smoothly follow the peak value of the signal. The peak detector configuration enables reduced sampling rate requirements of the ADC, and therefore reduces the overall power consumption. Another benefit of this sensing circuitry is that it also provides an information for over-current protection (OCP) and can be used for fault protection of the system.

It should be noted that a key feature of the sensors of the implemented CPT system, in particular of the current sensing circuitry is an isolated ground reference level to the sense resistor as well as the peak detector circuit (Fig. 5.11). By doing so, the limitations due to sensing relative to a floating voltage node are eliminated, in addition, this configuration also improves the signal to noise ratio.

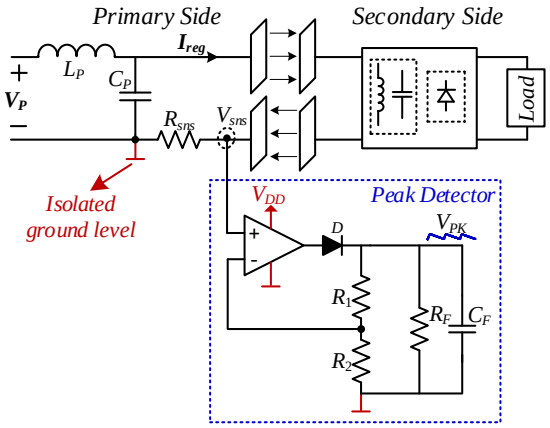

Fig. 5.11 Circuit diagram of the current-sensing setup.

5.4.5 Over-voltage protection

As mentioned in the phase detection procedure, the voltage across the resonating capacitors is very high particularly in such high-Q operation. Thus, to avoid any potential failure risks of the CPT system due to over-voltage in the vicinity of the coupler, an over-voltage protection (OVP) mechanism has been implemented as illustrated by Fig. 5.12. Similar to phase detection process, the voltage V_{CP} is sensed and scaled down by a high-resistance divider network to voltage levels suitable for the comparator operation. The scaling of V_{CP} and the value of the reference voltage, V_{ref},

are determined according to the highest voltage allowed across the capacitor C_P, i.e., across the coupling plates. For a case that V_{CP} is higher than the reference voltage, the comparator output is fed to the primary's controller disabling the gate drive signals (Q_1-Q_4), and as a result the system is turned off, until it is being reset. This also allows undesired safety concerns to be avoided due to arcing and high electric fields around the coupling plates [128].

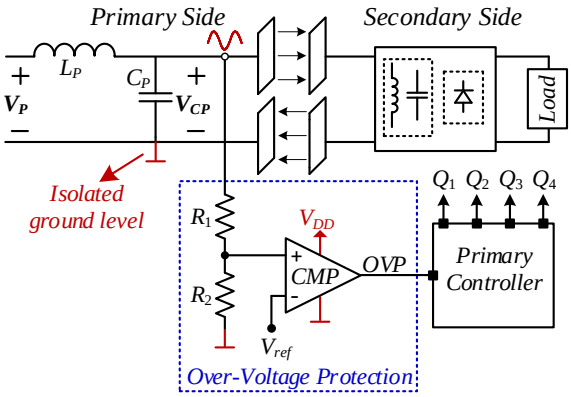

Fig. 5.12 Circuit diagram of the over-voltage protection setup.

5.4.6 Capacitive coupler design

To facilitate reliable estimation of the capacitive coupler for the experimental measurements, estimation of the plates capacitances has been carried out by Maxwell (Ansys) finite element analysis (FEA) tool (Fig. 5.13a). Typically, FEA are generated by defining the geometry of the element and by setting the boundary conditions. In the context of the capacitive coupler in this study, these are four symmetrical copper plates and voltage excitations to the plates. Rigorous simulation procedure over various air-gaps have been carried out to determine the coupling capacitances for symmetrical copper-based capacitive coupler, whereas each plate is 300x300 mm. Additionally, the thickness of the plates has been set to be 2-mm, to assure that it does not affect the coupling. The coupling capacitances of the plates have been calculated based on the equations in [37],[47] and the coupling coefficient, k_C, has been calculated by $C_{M1/2}$. The results for the equivalent mutual coupling capacitance, C_M, and for the self-capacitances (C_{M1} and C_{M2}) as a function of the air-gap are shown in Fig. 5.13b and Fig. 5.13c, respectively. It can be observed that C_M decreases by approximately ten times at an air-gap of 200 mm, while the self-capacitances (C_{M1} and C_{M2}) are in the range of 10 pF and virtually constant when the air-gap is larger than 100 mm. This is due to the fact that for air-gaps larger than 100 mm, the coupler can be characterized at deep loosely-

coupled region as can be observed from the results for the coupling coefficient shown in Fig. 5.13d.

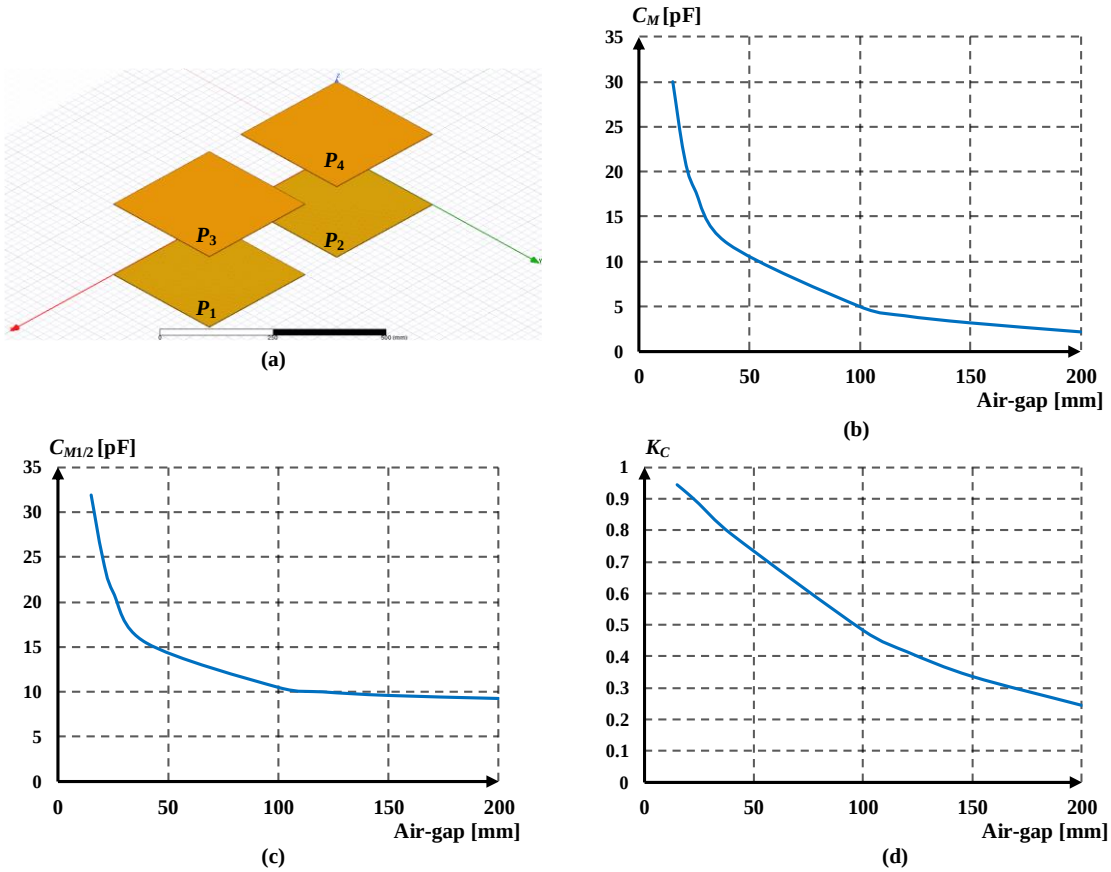

Fig. 5.13 Finite element analysis for the capacitive coupler design: (a) Ansys-Maxwell test-bench, (b) Mutual coupling capacitance, C_M, as a function of air-gap, (c) Self-capacitances, $C_{M1/2}$, as a function of air-gap, (d) Coupling coefficient as a function of air-gap.

5.5 Experimental Verification

To validate and demonstrate the operation of the adaptive multi-loop controller, an experimental double-sided *LC* capacitive WPT prototype with four copper plates that formed the capacitive coupler was constructed, as shown in Fig. 5.14a. To guarantee that the dominant capacitances were due to the coupling plates, the capacitive coupler was designed symmetrically, based on the analysis in Section 5.4.6, where each plate is 300x300 mm. Fig. 5.14b shows the custom-designed variable inductor which comprises an *E*-core type ETD49-3F3 magnetic element, as discussed in detail in Section 5.4.1. The controller core was fully coded in HDL and implemented on a Cyclone IV FPGA [129]. Typically, FPGAs, microcontrollers, and other digital platforms provide time resolution on the order of several hundreds of pico-seconds up to 1 ns. The implemented digital core of the controller is based on an asynchronous

hardware using combinatorial circuits, as previously described in [120]. By doing so, finer resolution can be obtained without a significant penalty of power consumption and hardware complexity. Since the coupler structure is symmetrical, the matching networks were also designed in this way; in nominal operation, the inductors' values are set to $L_P = L_S \approx 75$ µH and the matching capacitors $C_P = C_S = 250$ pF. High-voltage multilayer SMD ceramic capacitors were used in parallel to form the matching capacitors. The operating frequency was slightly above the resonance $f_0 \approx 1.2$ MHz to guarantee soft-switching. The full-bridge inverter was realized with GaN power modules operable in several MHz [103]. The overall nominal operating conditions and parameters of the experimental prototype are summarized in Table IV. It should be noted that the values were chosen such that for all corner scenarios (output power and air-gap) operating conditions are satisfied.

TABLE IV EXPERIMENTAL PROTOTYPE VALUES AND PARAMETERS AT NOMINAL OPERATION

Parameter	***Value/Type***
Input voltage V_{in}	30 V
I_{out} peak-to-peak	1 A
Coupling plates	300x300 mm, copper plates
Air gaps	20-200 mm
Full-bridge transistors	LMG5200, 80 V, 15 mΩ, Dual
Rectifier diodes	5-A/200-V, VSSC520S-M3
Variable inductors L_P and L_S	~75µH
Capacitors C_P and C_S	250 pF, AVX MLLC 5
Output capacitor C_{Load}	47 µF, EEV-EB2C470SM
Operating frequency f_0	1.2 MHz

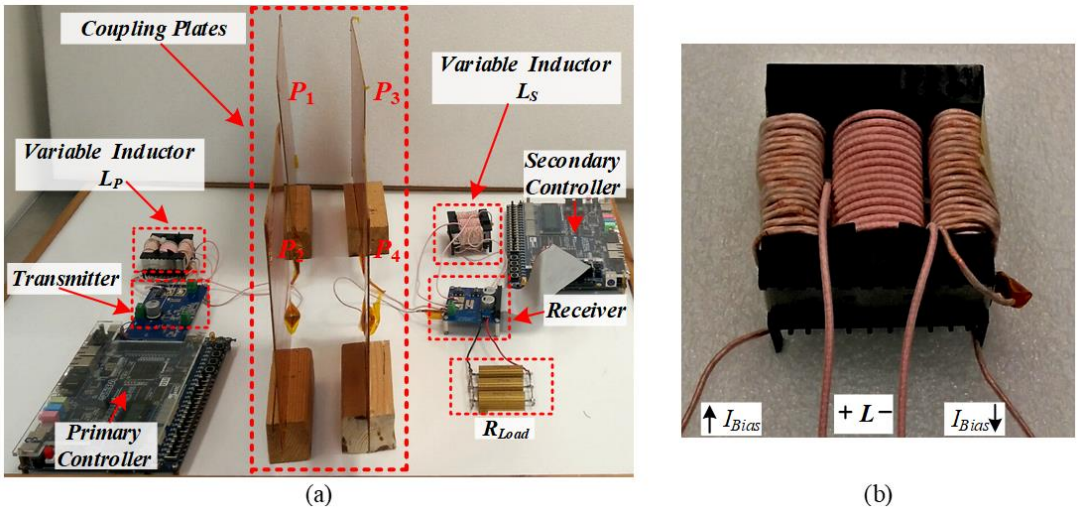

(a) (b)

Fig. 5.14 (a) Experimental setup of a double-sided *LC* capacitive WPT prototype; (b) *E*-core type-based variable inductor.

The first step of the experimental validation was carried out by characterizing the inductance of the variable inductor, and the resulting operating frequency of the CPT

prototype as a function of the bias current. Fig. 5.15 shows the measured results for varying the bias current in the range of 0 to 1 A. It can be seen that in the vicinity of the nominal operating conditions, the inductance and operating frequency f_0 are approximately 75 µH and 1.2 MHz, respectively, for a bias current of 0.25 A. It can be observed that this custom-designed inductor provides a 7X inductance variation, which is translated to a 2.5X frequency variation.

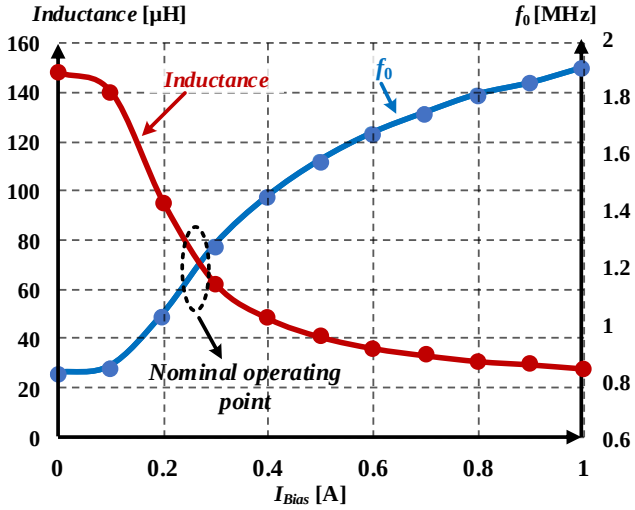

Fig. 5.15 Experimental measured inductance of the variable inductor and the resultant operating frequency of the CPT prototype as a function of the bias current.

Fig. 5.16a shows the behavior of the primary's current I_P and the secondary's voltage V_S during the tuning process for an input voltage V_{in}=30 V and 100 Ω load for an air gap of approximately 200 mm, where the quality factor of the primary side was found to be ~50. It can be observed that initially, the system is not tuned, and the regulated current on the primary side has a higher peak amplitude compared to the one at the end of the tuning procedure. This is due to the fact that at the beginning, the system has some pre-defined values (switching frequency, bias currents, etc.) that are not calibrated for the target operating conditions of this particular experiment, and best operating conditions are not satisfied, thus undesired circulating current is drawn from the source. On the other hand, at the end of the tuning procedure the voltage V_S has a higher peak amplitude, since the system is calibrated to resonance and is operated under (local) optimal power transfer conditions according to the target current. Fig. 5.16b and Fig. 5.16c show a zoomed-in views of the tuning process with the waveforms of the switching nodes voltages and resonant currents upon initialization (Fig. 5.16b) and the end (Fig. 5.16c) of the tuning process. It can be seen that the switching frequency increases from 892 kHz to 1.2 MHz. The output parameters (I_S and V_S) also increase,

delivering more energy to the load by more than 2.5 times, while the transfer efficiency has improved considerably (over four times). In addition, it can also be noticed that the primary current I_P is slightly lagging the primary voltage V_P, which is the necessary condition to enable soft-switching operation.

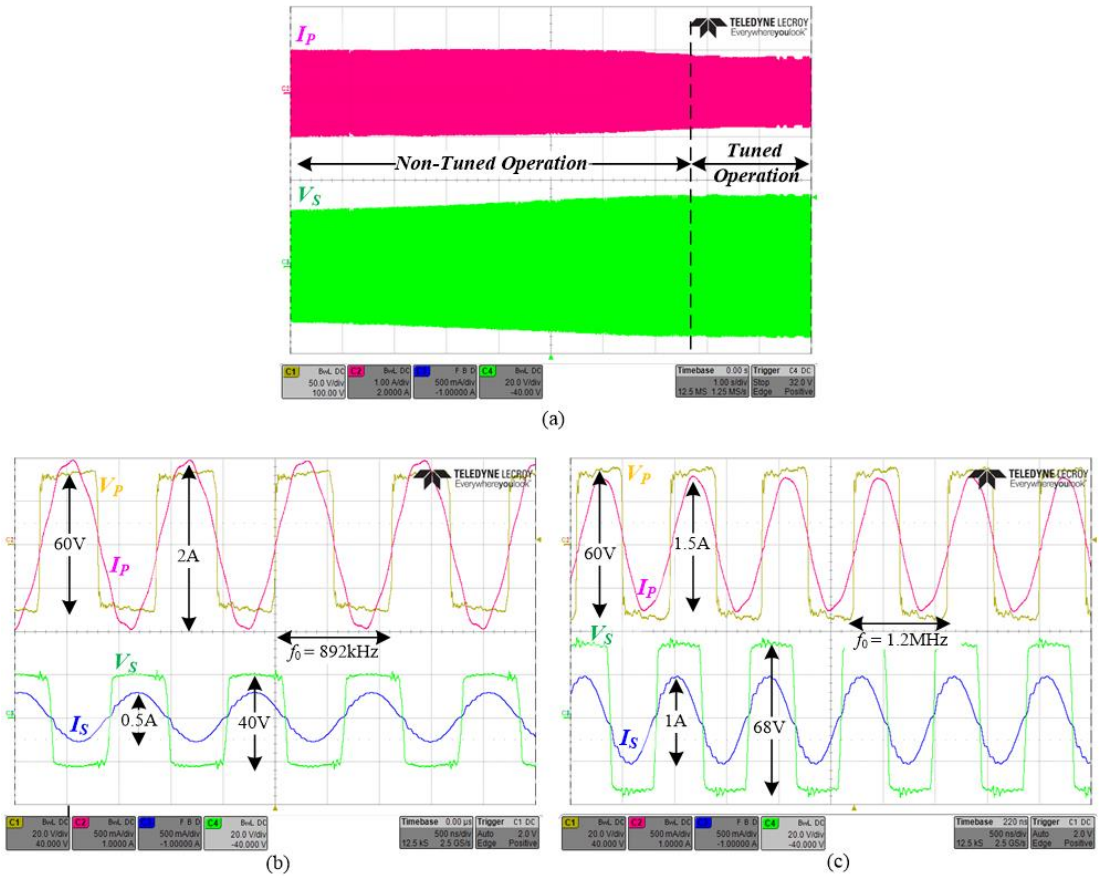

Fig. 5.16 Experimental results of the tuning process: (a) Full view of the envelopes of I_P and V_S, (b) Zoom-in view on the initial stage, (c) Zoom-in view on the final stage. Voltage scale 20V/div; Current scale 500mA/div; Time scale 500ns/div.

To demonstrate the effectiveness of the new multi-loop controller for capacitive WPT systems and showcase of the quality of the performance in closed-loop, the experimental prototype has been also tested for a target power of 10 W over various output load resistances, whereas the coupling capacitance $C_M \approx 2$ pF, as shown in Fig. 5.17a. A virtually constant power delivery is obtained throughout the load range. In the experiment of Fig. 5.17b the coupling capacitance has been varied to demonstrate the closed-loop operation under variations in the distance or displacement of the coupling plates. The experiments have been conducted with constant load resistance of R_{Load} =100 Ω, and varying the air-gaps up to the range of 200 mm, this translates to capacitance range of approximately 2–to-22 pF. Similar to the variable load test, it can be seen that, aside from measurement deviation, the output power is well regulated at a

constant value. These two measurements validate the closed-loop operation of the self-tuned CPT system, which provides regulated power delivery regardless the medium or load variations. From these experiments, it can be observed that for various output loads and air-gaps the controller provides 10X regulation capabilities. Fig. 5.17c shows the efficiency curve as a function of the various loads, it can be observed that at the range of 25 Ω the highest efficiency is achieved, which implies that for this experiment this is the matched load resistance to maximize efficiency. Efficiency analysis of a double-sided *LC* CPT system is not a key objective in this study, and comprehensive efficiency analysis on this configuration is detailed in [37]. It should be emphasized that to achieve constant output power, these measurements have been performed by manually adjusting the reference current in the primary side, $I_{ref,P}$, emulating wireless communication between the transmitter to the receiver.

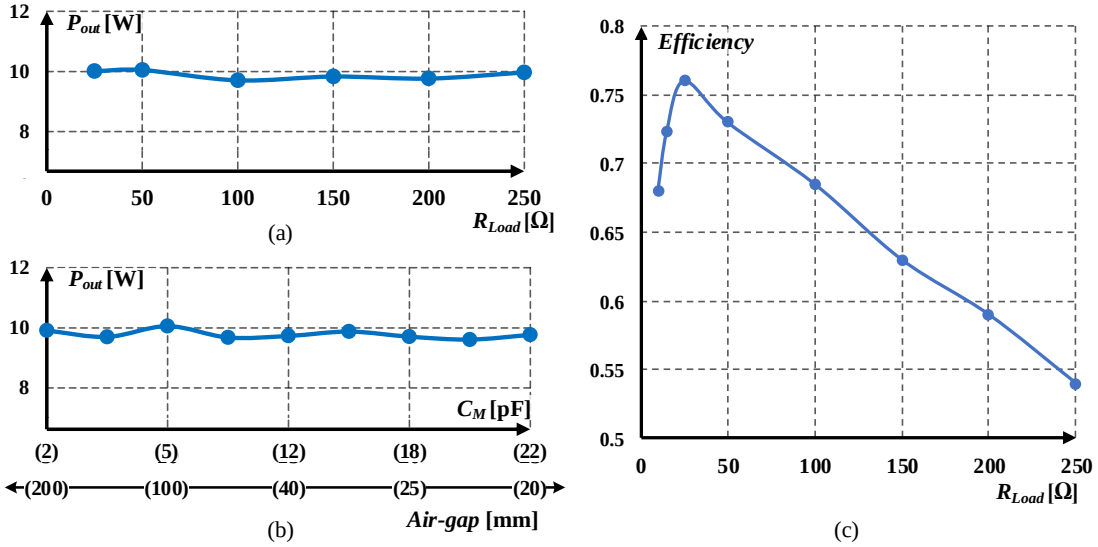

Fig. 5.17 (a) Measured output power for various loads, (b) Measured output power for various air-gaps, (c) Efficiency as a function of the load.

To further validate the controller approach and demonstrate the operation for higher output power and larger air-gap, the input voltage has been increased to 50 V at an air-gap of 250 mm. Demonstrated in Fig. 5.18 are load transients of 100 Ω to 200 Ω, for approximately 45 W output power. It can be seen in Fig. 5.18a that for a load of 100 Ω the average output current, $I_{out,AVG}$ is 0.66 A, voltage V_S toggles between 68 V to -68 V, and the output returns to power regulation within 50 ms. Fig. 5.18b shows a zoomed-in view of the waveforms of the switching nodes voltages and resonant currents at steady-state, it can be noticed that the operating frequency is 1.78 MHz, and the peak current of the secondary side is 1 A. For loading event from 0.47 A to 0.66 A (Fig. 5.18c), it can be seen that the system settles down back to the steady-state conditions within 60

ms. Fig. 5.18d depicts a zoomed-in views of the voltages and currents, there V_S toggles between 95 V to -95 V, I_S peaks at 750 mA, and the operating frequency is tuned to 1.1 MHz.

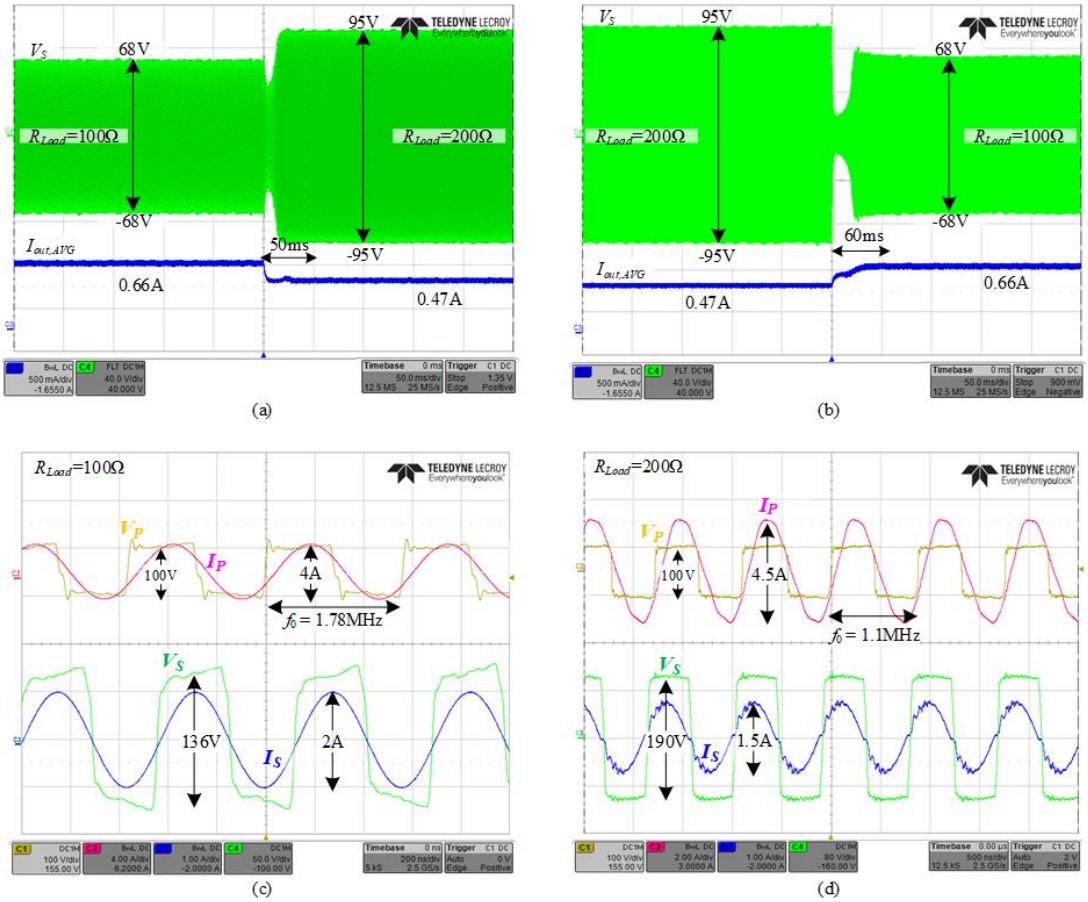

Fig. 5.18 Experimental results of the tuning process in response to a load step from 100 Ω to 200 Ω: (a) Full view of the envelopes of V_S and $I_{out,AVG}$ for unloading; (b) Full view of the envelopes of V_S and $I_{out,AVG}$, for loading; (c) Zoom-in view on the voltages and current of the primary and secondary on steady-state for 100 Ω; (d) Zoom-in view on the voltages and current of the primary and secondary on steady-state for 200 Ω.

CHAPTER 6:
Adaptive Self-Tuned Mixed-Signal Controller IC for Resonant-Based Wireless Power Transfer Systems

6.1 Introduction

Several methods to achieve resonant-frequency control for RWPT have been reported in the literature [60],[61],[82],[83],[86],[114]-[116],[130]-[133]; Tunable impedance matching techniques have been widely adopted in RWPT to adjust the resonant characteristics to a target fixed frequency [60],[61],[82],[86]. To obtain fine-tuning of the matching networks, in particular at high frequencies, a considerable number of passive components and bi-directional switches are required; thus, the overall system will be quite complex and bulky [61],[82],[86]. Automated frequency tracking methods have also been utilized in RWPT [84],[114],[116],[130],[131]-[133]. Several studies employed frequency tuning by maximum-power point tracking [114],[116],[130],[131]. There, the controller seeks for the peak power obtained at resonance, and tunes the operating frequency accordingly. The latter provides flexibility in power regulation, but comes at the cost of potential slow dynamics of the system and potential degradation of overall efficiency. Another technique for automated frequency tuning has been utilized based on phase detection [83],[84],[115],[132],[133]. Although reasonable dynamics can be obtained, this approach introduces a major tradeoff between frequency resolution and operation range. This can be improved by custom-designed analog-oriented ICs with tailored PLLs and accurate high-frequency generation; however, the design efforts, die area and overall power consumption significantly increases. On the other hand, digital-oriented architectures are very attractive in terms of design effort and integration [41],[120]. The main limiting factor of digital-based frequency synthesizers is that commonly used FPGAs, microcontrollers, and other digital platforms provide time resolution on the order of several hundreds of picoseconds up to nanoseconds [120],[134]-[136]. Therefore, to obtain a wide range high-frequency operation while maintaining high resolution, without significant penalty on power consumption and silicon area, *dedicated ASIC with specifically tailored hardware that can be realized through a simple design flow is required*. This has been pursued in this study.

The objective of this chapter is therefore to introduce an adaptive high-frequency high-resolution self-tuned controller IC (Fig. 1.4) for resonant-based WPT systems that has been developed on the basis of an all-digital standard-cell approach. The new controller IC relies on continuous tuning of the operating frequency to the resonant one, regardless of system variations and component drifts. It should be noted that although

existing closed-loop methods enable some system variations to be overcome and to extend the power delivery range (power levels and distance), a single control method is not always sufficient to guarantee reliable power delivery of WPT systems, particularly for dynamic WPT systems. Several works on the topic of multiple control loops have been investigated [82],[115],[137], and demonstrate the effectiveness of multi-loop controllers in the context of wireless power. Therefore, it was a further objective of this study to realize a digital architecture for controlling a continuous self-tuned variable inductor that is not based on relays or semiconductor switches, that enables more degrees of freedom on power regulation in the transmitter. The mixed-signal IC architecture is based on two independent control loops that include the following key building blocks: a wide-range high-resolution phase detector, high-resolution digital controlled oscillator (DCO), DPWM for the bias driver of the variable inductor, custom designed sigma-delta analog-to-digital converter (SD-ADC) programmable dead-time unit, and serial communication interface (SPI).

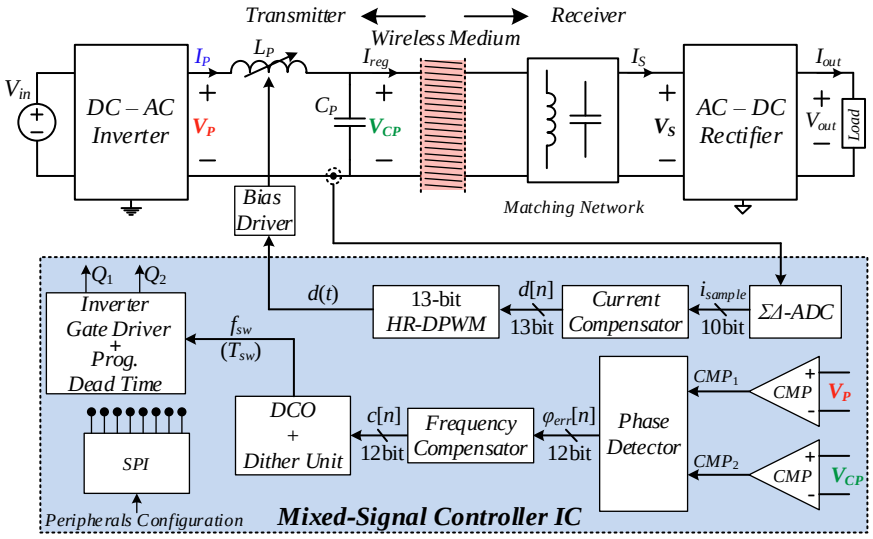

Fig. 6.1 Simplified schematic diagram of a WPT system with the adaptive self-tuned mixed-signal controller IC.

6.2 Control of RWPT Transmitters

6.2.1 Review of L-type based resonator

The principle of operation of the adaptive RWPT controller IC is described here, without losing generality, through a L-type series-parallel (*LC*) matching network [37],[48],[57], as delineated in Fig. 1.4. It should be further emphasized that the core of the control algorithm is applicable for various near-field resonant-based WPT configurations. Assuming loosely-coupled operation [46]-[48], the drive frequency, f_{sw},

is near the matching networks' resonant frequency (i.e., $f_0 = 1/(2\pi\sqrt{LC})$), then the currents as well as voltages of the passive components are virtually sinusoidal [99]. This is because high-Q operation is naturally facilitated as the effective output impedance of the *LC* matching network in the transmitter is relatively high. Fig. 6.2 depicts typical waveforms of resonant L-type-based transmitters. For a full-bridge DC–AC inverter as the front end, the inverter voltage, V_P, toggles between V_{in} and $-V_{in}$, whereas for a half-bridge configuration, V_P toggles between 0 and V_{in}. In both configurations the sinusoidal current, I_P, is in phase with V_P. Additionally, it can be seen that at resonance the phase difference between V_P and the sinusoidal voltage across the matching capacitor, V_{CP}, is 90°.

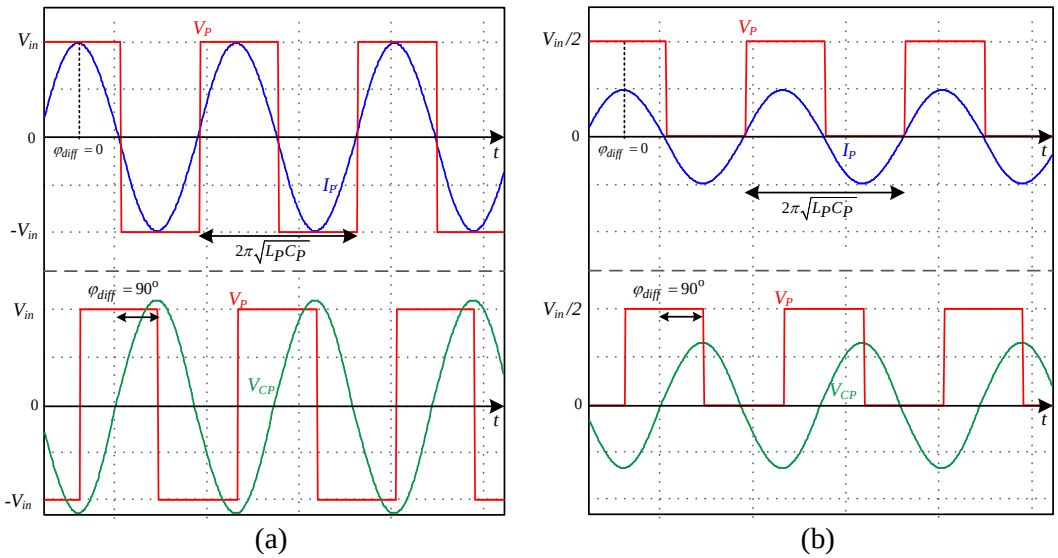

Fig. 6.2 Typical waveforms of a L-type based WPT transmitter operating at resonance: (a) Driven by a full-bridge inverter. (b) Driven by a half-bridge inverter.

6.2.2 Controller operation

Following the observations made in the previous section, an adaptive controller that monitors, tunes, and enables the system to be continuously kept at optimal power transfer conditions is addressed. The controller operation is facilitated by two major control loops, as shown in Fig. 1.4. The adaptive tuning operation is performed independently per feedback loop, with its respective objective and rate. In structure, the first loop resembles a digital controlled oscillator (DCO) that synthesizes a switching frequency, f_{sw}, which continuously follows the resonant frequency, f_0, even under variations of the system parameters. In a WPT system, this self-driving concept ensures that the power conversion and transfer characteristics of the transmitter are optimized. The second control loop comprises a current compensator and a tuning unit that adjusts

the inductance value of L_P such that a target current (as well as power) is regulated from the transmitter side to the wireless medium. This transforms the transmitter side into a self-tuned architecture in which the drive frequency spontaneously tracks the resonant frequency, and the transmitted power is regulated by adjusting the resonant network's characteristics. It should be noted that the control loops can operate independently to facilitate a specific objective out of the controller.

The principle of operation of the new mixed-signal controller IC that was realized in this study is described with the aid of Fig. 6.3, which shows a high-level flowchart of the tuning procedure utilizing the control loops and a functional block diagram of the controller, respectively. Since the controller IC should function as a stand-alone module, the hardware architecture includes a small volatile memory as a part of the serial communication interface (custom-designed SPI) that is preprogrammed with a set of default values for the main parameters of the controller. On startup, the default values can be used or a new set can be loaded to the controller through the SPI. Then the SPI internally communicates with the main units and loads the set of values per block. A benefit of this embedded feature is that the same controller hardware can be used with different power stages, matching network configurations, and parameters.

Upon initiation of the tuning procedure (Fig. 6.3), a default set of pre-loaded values are used to determine the switching frequency, f_{sw}, variable inductor, compensators, parameters, etc. The inner feedback which is the fastest loop, applies frequency tuning. There, the switching frequency, f_{sw}, to drive the DC–AC inverter is varied by the DCO unit to match the resonant frequency of the circuit f_0. This is facilitated by measuring the voltages V_P and V_{CP} (Fig. 1.4), extracting the phase difference between them, and adjusting f_{sw} until the phase difference between the signals reaches 90º. In the case where the detected phase difference between the signals is not 90º, an error signal is generated to the DCO, which in turn synthesizes a new switching frequency until $f_{sw}=f_0$. In the next stage of the tuning operation, the transmitter's current, I_P, is sensed and compared to a target/reference one (Fig. 1.4), which is pre-defined by the SPI unit. It should be noted that for a WPT system with multiple loads, it is essential that the controller be able to maintain a constant current operation [85]. The correction signal that is generated is used to vary the inductance L_P through a bias winding until the required current is achieved. This variation of the inductor value is realized by a buck converter current driver that applies dc bias to non-gapped side windings of the inductor, as described in the previous subsection. Due to variation in the inductance

value, the resonant characteristics of the transmitter change, and potentially move the system out of its optimized transfer conditions. As a result, the frequency tracking loop needs to search again and lock the switching frequency into the resonant frequency.

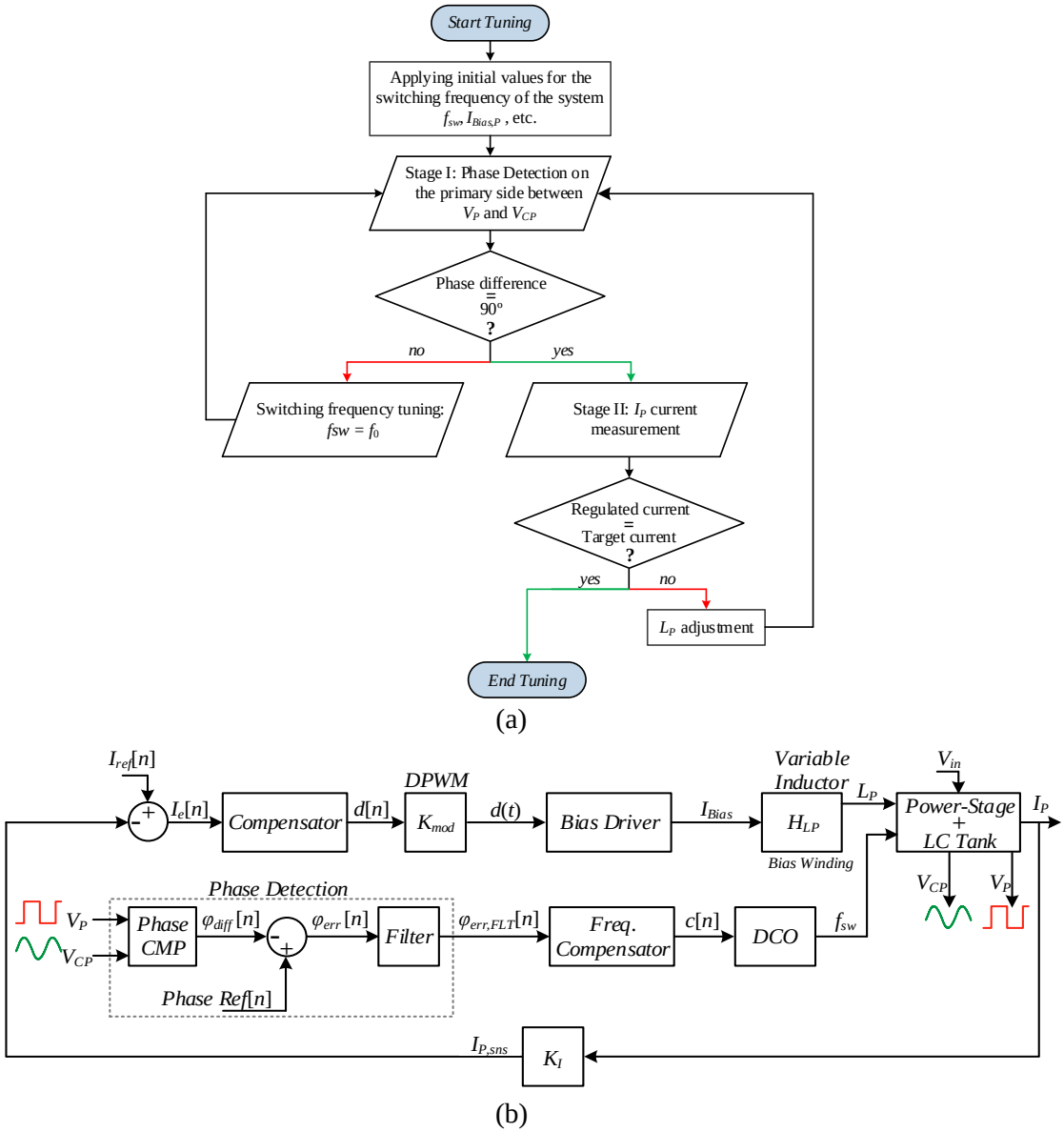

Fig. 6.3 Tuning procedure flowchart of the controller IC; (b) Functional signal flow diagrams of the controller IC.

6.3 Adaptive RWPT Controller IC Architecture

The realization of the adaptive mixed-signal controller IC relies on three key enabling blocks: 1) an 11-bit high-resolution wide range phase detector, 2) a 12-bit enhanced dither-based high-resolution DCO, and 3) a 13-bit high-resolution digital PWM (HR-DPWM) that generates a gate drive signal for the bias current driver of the variable inductor. Each of the fundamental units was implemented as an asynchronous hardware using delay-lines (DL) [138],[139] and combinatorial circuits. By doing so, a

significant portion of complex and power-hungry hardware for timing and high-speed synchronization is eliminated. Since some of the units are still based on a synchronized process, a system governor is employed to provide a time base to the switching cycle and to trigger the sequential operation of the functional blocks within the switching cycle.

6.3.1 Phase detector

Accurate wide-range phase detection is one of the key factors necessary to achieve high-performance frequency control in RWPT systems. Thus, conventional methods for phase detection which consist of a type-I detection circuit, i.e., comparators as digitizers and an exclusive-or (XOR) phase comparator [140], are not sufficient since they have a narrow dynamic range of operation. Additionally, there is no direct information about whether the phase difference is positive or negative.

The phase detector in this study is based on a time-to-digital conversion (TDC) using a DL string built of digital buffers with a fixed propagation time [120],[138],[139], as shown in Fig. 1.4. The phase difference is translated by the time difference between the signals CMP_1 and CMP_2 (which are the digitized representations of V_P and V_{CP}), and obtained by the combination of a few basic operators (Fig. 1.4). The signal, *TRG*, triggers the DL string and starts the conversion process such that seven LSBs of the output registers are a direct Wallace–Tree translation [120] of the DL. A counter, triggered both at the rising and falling edges, is connected to the end of the string to count the repetitions of full DL string propagations, and the result is conjugated as the five MSBs of the output register. Once the *TRG* returns to a low logic level, the counter holds the number of cycles that the DL propagates throughout the pulse width of the *TRG*, while the DL holds the residual time difference with higher time resolutions, due to the partial propagation of the last run. An 11-bit result of the phase difference, $\varphi_{diff}[n]$, is generated together with $T_{sw}[n]$, which represents the switching period (time representation of the 360º phase range) with respect to the operating frequency of the system. This is essential since the phase difference and the phase reference must be normalized to the time base of the synthesized operating frequency. The phase error, $\varphi_{err}[n]$, is obtained by subtraction between the phase reference and $\varphi_{diff}[n]$, where the MSB of $\varphi_{err}[n]$ is a sign bit. Finally, to obtain a noise-clean phase error signal, $\varphi_{err}[n]$ is filtered.

It should be further noted that since the voltages of the resonator are significantly higher than the operation voltage levels of the controller and other electronics periphery, the voltages V_P and V_{CP} are scaled down using a high-impedance attenuation circuit to voltage levels suitable for logic gate input, such as the phase detector unit. From a practical implementation perspective, if a simple resistive divider is used, the input capacitance of the logic gate introduces a phase delay between the actual zero-crossing point and the digital signal transition. In the case where the phase shifts of the two measured signals are different (due to different resistive paths, a systematical offset exists, and should be calibrated out. This can be solved by setting the phase reference slightly higher (or lower) than the target one, compensating for undesired offsets due to the voltages sensing paths. Another approach to minimize phase offset errors is to employ similar voltage scaling for both measured signals as much as possible; however, this might be impractical in high voltage gain systems. In such cases, active attenuation circuits, as well as adaptive calibrations are required.

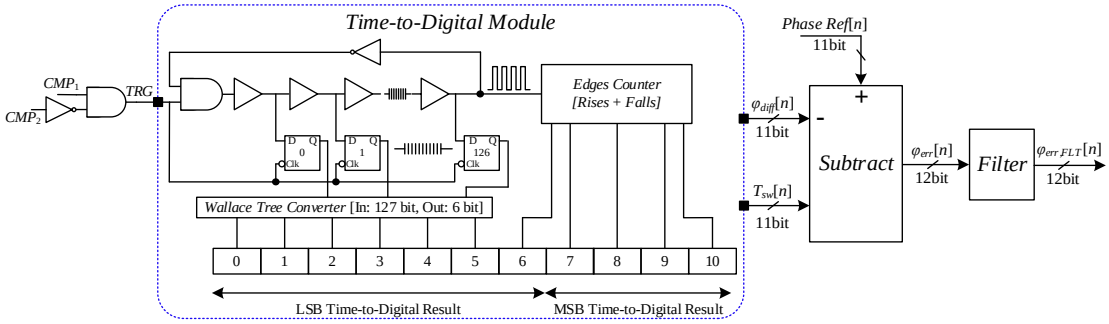

Fig. 6.4 Schematic diagram of the high-resolution phase detector.

6.3.2 High-resolution digital controlled oscillator

The core of the DCO in this study is based on an adaptive variable ring oscillator combined with counter-comparator units, as delineated in Fig. 6.5 a[141],[142]. To obtain both a wide-range and high-frequency operation while maintaining a single delay-cell resolution, without sacrificing overall efficiency and the silicon area, the DCO's output signal is generated based on coarse, fine, and ultra-fine-tuning of the ring oscillator. The coarse tuning (also denoted as CNT_{per}) defines how many ring-oscillator cycles are needed for generating the output period. Next, a fine-tuning value controls the delay ring size, i.e., how many extra delay elements should be added to the basic ring-oscillator string to improve the resolution. Finally, an ultra-fine value defines how many ring cycles should have an additional delay element within the output period. Based on the ultra-fine and coarse signals, a counter-comparator unit is responsible for

enabling the additional delay. For a case in which finer resolution of the output signal is further required, a frequency dithering feature [124],[144] was embedded in the DCO. The enhancement signal defines and enables an extra delay element to be added to the ring-oscillator string (see Fig. 6.5b), further improving the resolution of the output period effectively finer than a single cell resolution.

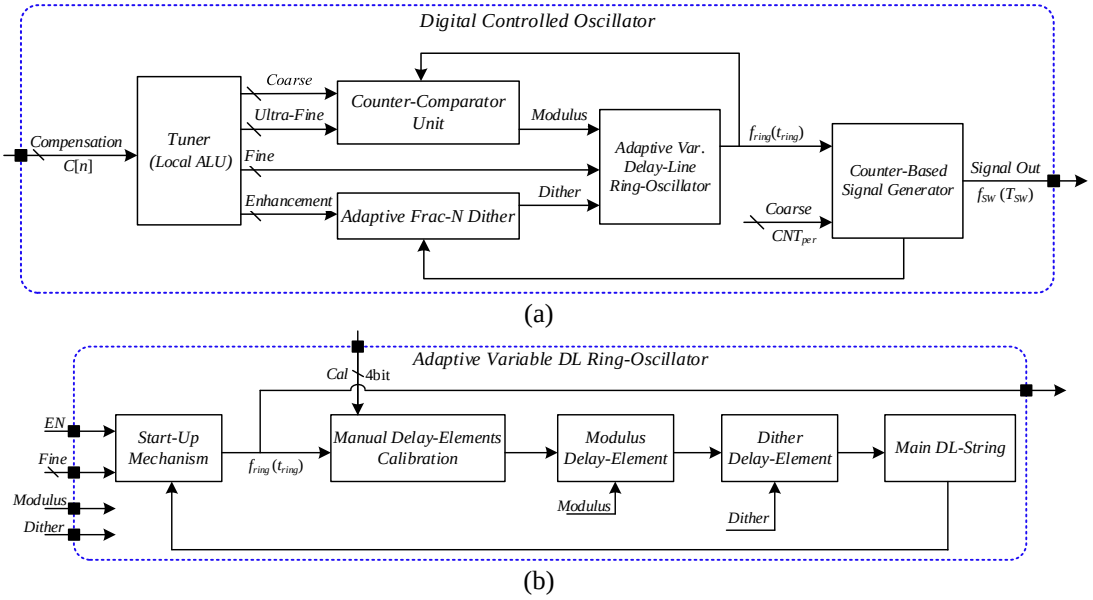

Fig. 6.5 Block diagram of the DCO; (b) Simplified block diagram of the adaptive variable ring-oscillator.

The DCO in this study was designed to generate frequencies of approximately 1–10 MHz, and the general frequency relationships of the DCO can be expressed as follows:

$$f_{ring} = \frac{1}{\underbrace{Nt_{DE}}_{t_{ring}}} \Rightarrow f_{sw} = \frac{f_{ring}}{CNT_{per}} = \frac{1}{CNT_{per}t_{ring}}, \tag{6.1}$$

where f_{ring} is the frequency of the ring oscillator, t_{DE} is the delay of a single delay-element within the ring oscillator, N is adjustable overall number of the delay elements in the ring, and CNT_{per} is an integer that represents the coarse value of the counter for generating the target output frequency f_{sw} (period-T_{sw}). It should be noted that due to possible process, voltage, and temperature (PVT) variations, and other potential post-fabrication mismatches, t_{ring} can also be manually calibrated by adding or removing delay elements within the ring oscillator (see Fig. 6.5b). The frequency resolution of the DCO, f_{res}, can be calculated as the LSB change in CNT_{per}

$$f_{res} = \Delta f_{sw} = \frac{1}{CNT_{per}t_{ring}} - \frac{1}{\left(CNT_{per}+1\right)t_{ring}} \approx \frac{1}{CNT_{per}^2 t_{ring}} = t_{ring} f_{sw}^2 . \tag{6.2}$$

From (6.2), it can be observed that the frequency steps of the DCO are limited by the module's base frequency, and increase as the square of the operating frequency, i.e., at

a lower operating frequency, the frequency resolution would be finer than what can be achieved at a higher frequency.

Since finer resolution is desired over the entire operating range, an effective, fast dynamic and low distortion frequency enhancement dithering procedure was employed. An adaptive 3-bit Frac-N dithering method (Fig. 6.6 Block diagram of a 3-bit Frac-N dithering module.) is facilitated by dithering the DCO between CNT_{per} and CNT_{per}+1 at a defined rate, varied by the required accuracy. The dither factor, n, is the number of DCO cycles needed to achieve the desired fractional frequency. Dithering is accomplished by keeping a constant period over (n-1) DCO cycles (referred to as the base period), and then changing the last slot (n) to another period. The resultant (average) frequency using this method can be calculated by a general expression as follows:

$$f_{sw\_dither} = \frac{1}{\left[(n-1)CNT_{per} + (CNT_{per}+1)\right] / nt_{DE}} = \frac{1}{\left(CNT_{per} + 1/n\right)t_{DE}} \; ; n = 1, 2, 3 \ldots , \tag{6.3}$$

and the enhanced frequency resolution

$$f_{res\_dither} = \frac{1}{\left(CNT_{per} + 1/n+1\right)t_{DE}} - \frac{1}{\left(CNT_{per} + 1/n\right)t_{DE}} \approx \frac{1}{n(n+1)CNT_{per}^2 t_{DE}} = \frac{t_{DE} f_{sw}^{\;2}}{n(n+1)} . \tag{6.4}$$

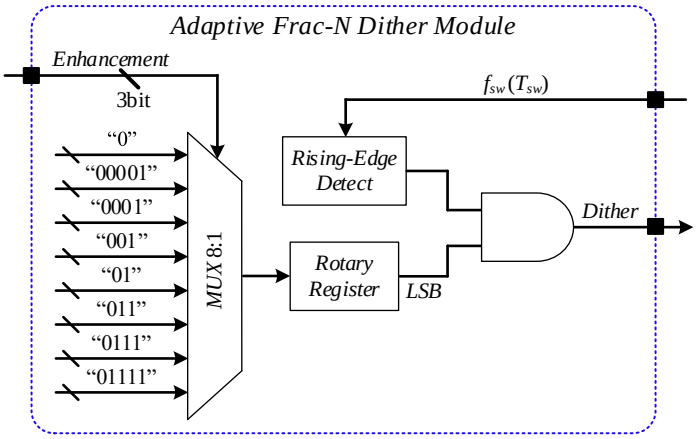

Fig. 6.6 Block diagram of a 3-bit Frac-N dithering module.

Fig. 6.7a shows an illustrative example of a frequency fraction of 0.25f_{res} where the DCO generates one (CNT_{per}+1) period every 4th cycle. Additionally, Fig. 6.7b shows a comparison between ideal infinite frequency states, a Frac-N dithering method for a 3-bit frequency resolution enhancement (i.e., eight additional frequency fractions between two base DCO values), and a typical DCO operation.

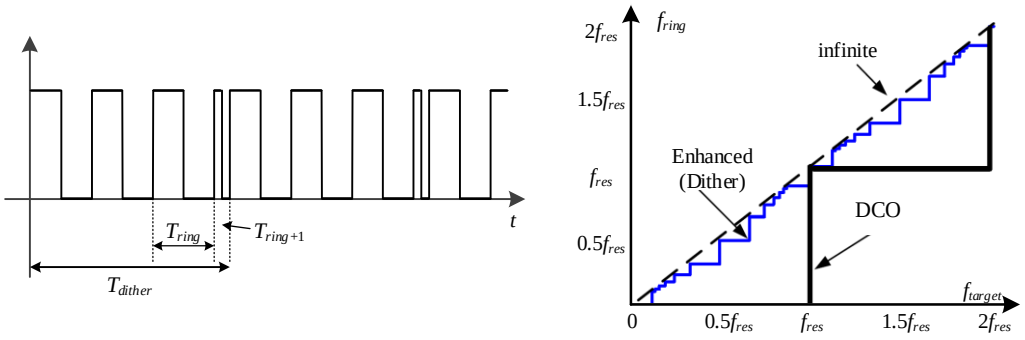

(a) (b)

Fig. 6.7 (a) Dithered output signal with a frequency fraction of 0.25fres; (b) Output frequency versus desired frequency for typical DCO and 3-bit resolution enhancement.

6.3.3 High-resolution digital pulse width modulator

To accurately control the variable inductor and to avoid undesired oscillations, a high-resolution modulator is required. The conventional approach to implement HR-DPWM is by a fast-clocked counter-comparator scheme [142],[143]. In this way, n-bit resolution at a switching frequency of f_{bias} requires a reference clock frequency of $2^n \cdot f_{bias}$. This translates to increased power consumption and more complex design to realize the high-speed circuitry. Another approach to realize a HR-DPWM is based on a tapped DL scheme [138],[139]. In this method, the power consumption is reduced, but the required silicon area of the design grows exponentially with the number of resolution bits.

The HR-DPWM in this study was realized based on a combined coarse–fine digital counter concept [120]. Fig. 6.8 shows the conceptual architecture of the unit. As can be seen, it is composed of two main functional units: a counter-based coarse resolution PWM generator and a fine-tuning delay chain combined with an OR operator. The 13-bit digital word for the duty-cycle command d[12-0] is distributed within the units. The coarse resolution PWM block is fed by a reference clock (generated by the system governor), which is counted and compared with 7 upper bits of the duty-cycle command d[12-6]. The resulting signal PWM_{Coarse} can be expressed by:

$$PWM_{\text{Coarse}} = \begin{cases} d[12-6] > cnt[6-0] \ , \ '1' \\ d[12-6] < cnt[6-0] \ , \ '0' \end{cases}. \tag{6.5}$$

The fine resolution PWM unit generates a string of 6-bit long DL that finely adjusts PWM_{Coarse} by the number of delay elements, as specified by d[5-0]. The latter combined with the OR operator generates the high-resolution PWM output signal, $d(t)$. The switching frequency of the HR-DPWM, f_{bias}, can be expressed as a function of the

number of bits and the propagation time of a single delay element t_{DE} (of the fine-delay module) as:

$$f_{bias} = \frac{1}{t_{DE}\, 2^{N+M}}; \begin{cases} N - \text{ number of coarse bits} \\ M - \text{ number of fine bits} \end{cases}, \tag{6.6}$$

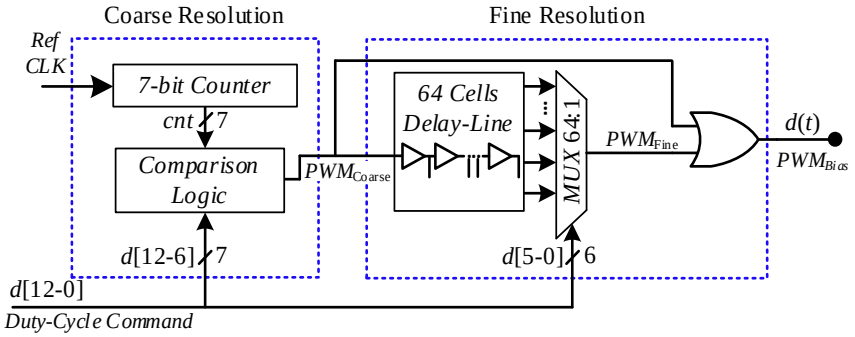

Fig. 6.8 Simplified architecture of the 12-bit HR DPWM.

6.3.4 Sigma-delta analog-to-digital convertor

Analog-to-digital conversion of the current control loop is facilitated in this study by a Sigma-Delta ADC [11]. The SD-ADC has been realized with simplified hardware to reduce complexity, power consumption, and effective silicon area. As can be seen in Fig. 1.4a, the modulator front end is realized by a digital inverter, with i_{sample} as the high logic level (supply). The integrator is realized by a simple RC network with a corner frequency of at least one order of magnitude lower than the clock frequency. The quantizer is realized by a digital inverter-based configuration, whereas the result is then held by a D-type flip-flop to facilitate a clocked bitstream at the oversampling frequency of the ADC. The layout of the SD-ADC with overall dimensions is shown in Fig. 1.4b. The implemented ADC may come at the cost of the conversion rate; however, since at resonant power conversion, in particular at high-Q operation, the response of the system to variations is rather slow and carries on over several switching cycles. The overall architecture of the ADC is well suited to the control specifications of the current loop.

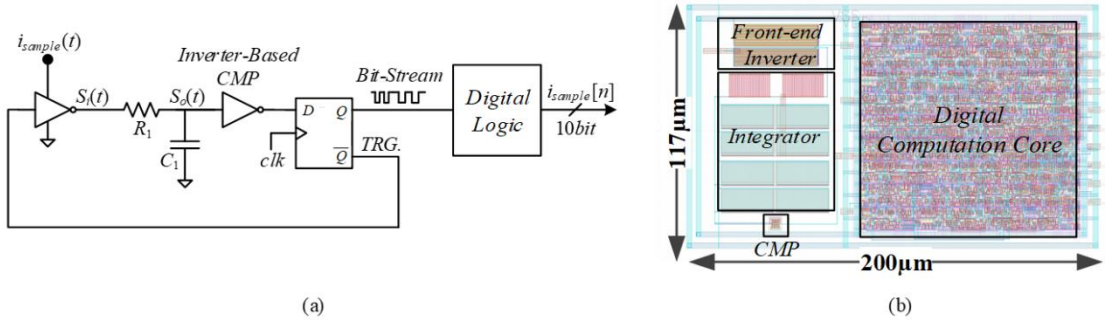

Fig. 6.9 (a) SD-ADC architecture. (b) Layout of the SD-ADC.

The resultant SD-based ADC is a hardware-efficient voltage level translator in which the average voltage at node $S_o(t)$ can be expressed as:

$$\overline{S_o(t)} = V_{ref} = i_{sample}(t)\frac{CNT}{2^n}, \tag{6.7}$$

where V_{ref} is the reference value for the modulation process (the threshold voltage of the inverter-based comparator), and *CNT* is the number of logic-high occurrences in the bitstream for 2^n clock cycles. An illustration of the voltage at the input of the inverter-based comparator, $S_o(t)$, is shown in Fig. 1.4, along with the resultant bit-stream and the oversampling clock. The bitstream is the input to a computational digital logic which counts the number of "ones" (equal to *CNT*) with a dedicated counter that acts as a sinc LPF, and resets at pre-defined intervals to perform decimation. In this study, the sampled signal applied on the front-end inverter is translated to a digital representation every 1,024 clock cycles, which results in a 10-bit representation of the measured current.

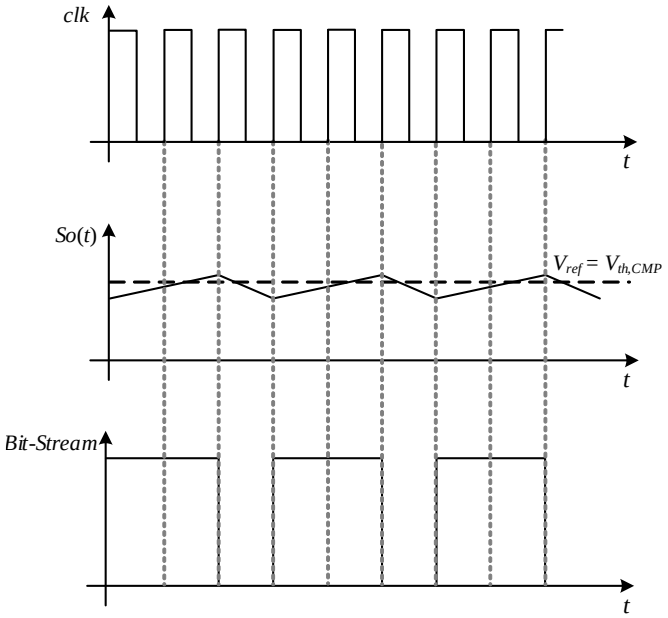

Fig. 6.10 Typical waveforms of the SD-ADC.

6.3.5 Programmable dead time

Resonant-based WPT systems are typically designed at multi-MHz switching frequencies to reduce the overall size of the wireless link and passive components. In addition to shoot-through issues of the DC-AC inverters [148], maintaining zero-voltage switching (ZVS) while controlling the power delivery is of a great importance in such MHz range power conversion systems [149],[150]. Therefore, a programmable dead-time module was developed and realized in the controller IC, making it more

robust for various operating conditions. The dead-time unit consists of a string of 256 delay elements connected to an 8-channel multiplexer, as shown in Fig. 1.4. In a similar manner to the other pre-defined values, the dead-time period, t_{DT}, is set within the SPI memory register with an initial default value, and can be programmed from approximately 5 ns up to 50 ns.

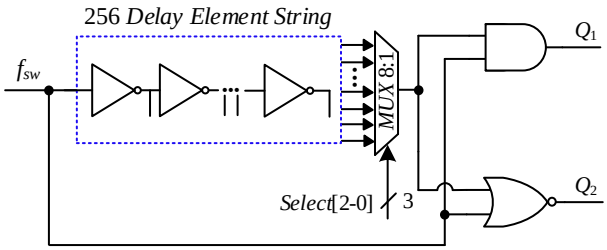

Fig. 6.11 Schematic diagram of a programmable dead-time module.

6.4 System Level Considerations

6.4.1 Limit-cycle oscillations in digitally controlled RWPT

As discussed in detail in Section 5.4.2, limit-cycle oscillations (LCOs) should be taken into consideration when designing digitally controlled RWPT systems. Therefore, to ensure a smooth high-frequency drive throughout the operation range, the DCO in this study was designed to achieve the required effective acquisition, as well as to control resolution such that limit-cycle oscillations are remedied.

As discussed in Section 6.3.2, frequency dithering was embedded to enhance the drive frequency, and to provide effective frequency (over a few cycles) with finer resolution than the base value. The effect of frequency resolution in resonant converter drives is depicted in Fig. 6.12, which is the simulated output response of a series-parallel resonator (L-type) driven by a typical 8-bit DCO and by the presented dithered-DCO with 3-bit resolution enhancement. In addition, slow-response characteristics of resonant networks due to high-Q also aids with LCO in the context of RWPT systems. Since it takes the resonator several cycles to react to changes in the drive frequency, it is utilized as an averaging action. To demonstrate this characteristic, a cycle-by-cycle simulation at a resonant frequency of 4 MHz with steps of 5 kHz was utilized. It can be observed from Fig. 1.4 that the convergence time, t_{step}, to ±5 kHz step was approximately 100 switching cycles.

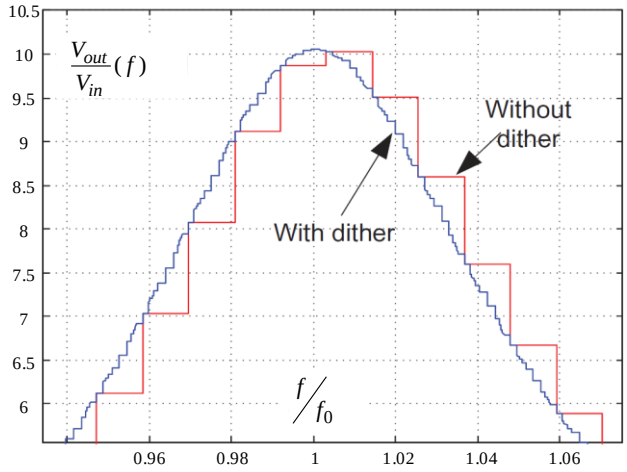

Fig. 6.12 Simulated frequency response (sweep) of an L-type resonant network. Comparison between typical DCO frequency steps and 3-bit resolution dithered-based DCO.

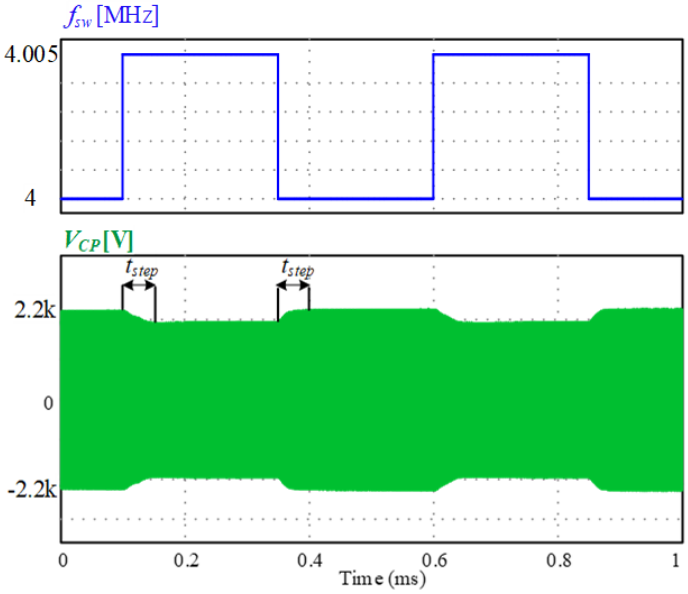

Fig. 6.13 Simulation results showing the convergence of the resonator's sinusoidal voltage, VCP, to frequency steps of ±5 kHz.

6.4.2 Phase detection averaging

In addition to stability issues due to frequency resolution and LCO, noises due to the phase detection process might also result in unstable operation. Noise sources such as quantization of the time-to-digital unit, sensing, or thermal noises may also affect the accuracy of the phase detection, which is then translated to inaccurate frequency compensation. To remedy this, synchronous averaging of samples was employed to average out the phase error signal. This was carried out by an 8 word-long auto-regressive moving average (ARMA) filter [151],[152]. Although, this averaging process might extend the duration of the self-tuning routine, it enables the phase error to be smoothen, which results in better frequency compensation. It should be noted that

the averaging window can be programmed to lower lengths in case faster responses are desired.

6.5 Experimental Verification

A RWPT mixed-signal controller IC was designed and fabricated in a 0.18-μm 5-V CMOS process. The IC micrograph is depicted in Fig. 1.4a, and the fabricated IC on an evaluation board is shown in Fig. 1.4b. The overall chip area is 4 mm^2, while the effective silicon used is 0.6 mm^2. The delay of the buffer-based delay element used for the asynchronous architecture of the controller is ~200 ps, which is translated to an operating frequency range of 1.25–10 MHz. The main characteristics of the controller IC are summarized in Table V. It should be emphasized that the controller's design scales with the technology such that its overall area and performance can be further improved by implementing it to a more advanced process without a significant penalty on power consumption.

TABLE V MIXED-SIGNAL IC MAIN CHARACTERISTICS

IC Block / Parameter	***0.18-µm CMOS***
Package	28 pins 5x5 QFN
Supply voltage	5-V
Single cell delay t_{DE}	200 ps
Phase detector resolution	11-bits
Phase detector+Compensator Si area	0.225 mm^2
DCO resolution	12-bits
DCO frequency range f_{SW}	1.25-to-10 MHz
DCO Si area	0.097 mm^2
DPWM resolution	13-bits
DPWM nominal frequency	625 kHz
DPWM Si area	0.03 mm^2
ADC resolution	10-bits
ADC Si area	0.025 mm^2
Dead-time range	6.5-51 ns
Dead-time Si area	0.01 mm^2
Effective Si area	0.6 mm^2
*including analog peripherals and SPI	
Total chip Si area (pad limited)	4 mm^2

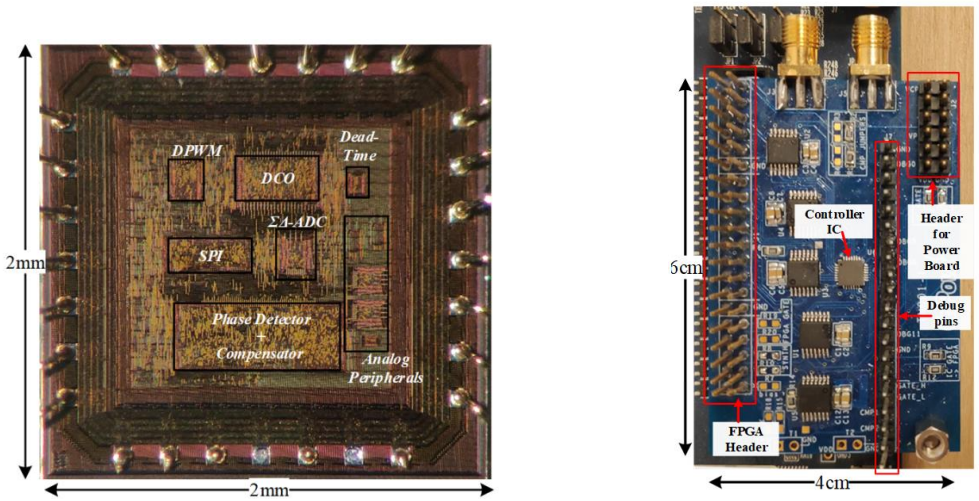

Fig. 6.14 (a) Micrograph of the fabricated RWPT controller IC. (b) Evaluation board of the IC.

The operation of the controller IC was verified prior to fabrication with a post-layout analysis using Cadence Virtuoso, where the IC drives a full-bridge inverter at the front end, with an external L-type resonator (see Fig. 6.15a); L_P=11 µH, C_P=50 pF for 6.78-MHz operation, and L_P=45 µH, C_P=35 pF for 4-MHz operation. Using a high-impedance resistive divider, the voltages V_P and V_{CP} are scaled down to voltage levels suitable for the chip operation. Fig. 6.15b depicts results for resonant operation at 6.78 MHz. As can be seen, the target phase reference (90º) is translated to a decimal representation of "1864", and a phase difference of "1860"; thus, the error is equal to "4" (with respect to 11-bits). The dead time between the generated gate drive signals is 6.5 ns. Fig. 6.15c demonstrates resonant operation at 4 MHz. It can be noticed that although a phase difference of 90º is obtained, the values are translated to different decimal representations since the values are normalized with respect to the switching period, as discussed in Section 6.3.1. In addition, Fig. 1.4 shows frequency resolution measurements at 6.78 MHz and 4 MHz, respectively. As can be seen, the effective frequency resolution at 4 MHz is ±1.25 kHz, whereas for 6.78 MHz, the effective resolution is approximately ±4 kHz, which satisfies the allocated frequency bandwidth according to the AirFuel Alliance [85].

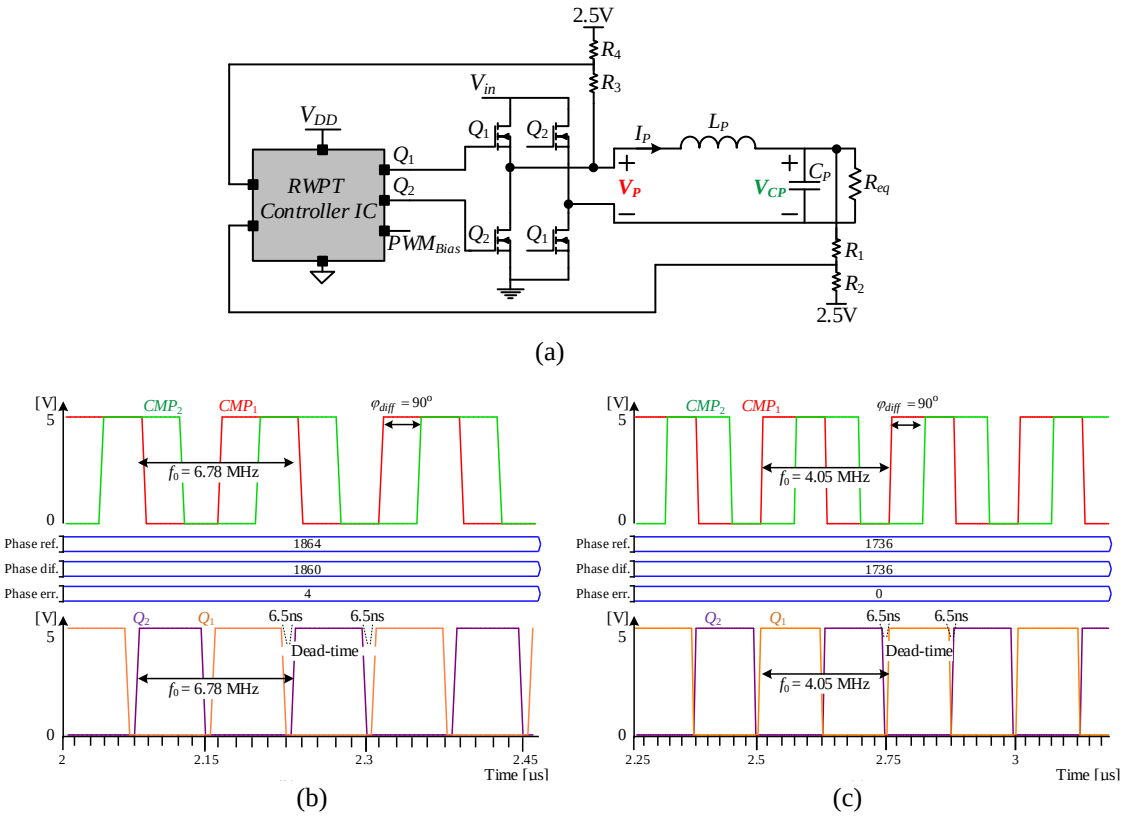

Fig. 6.15 Simplified equivalent circuit for the transmitting side.

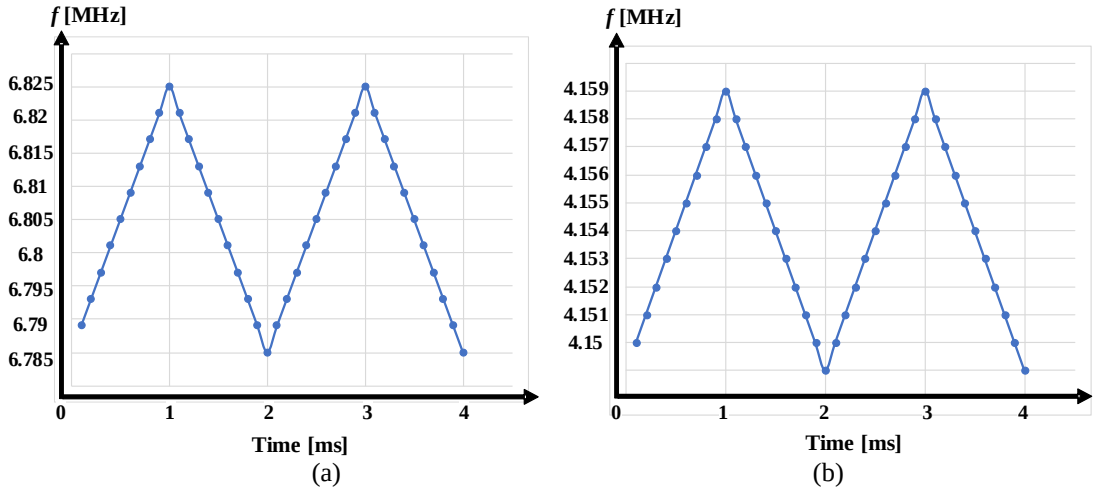

Fig. 6.16 Frequency resolution at the vicinity of resonant operation at: (a) 6.78 MHz, (b) 4 MHz.

To validate the new adaptive RWPT controller IC and to demonstrate operation for a complete resonant-based WPT system, a resonant capacitively-coupled experimental setup was constructed, as shown in Fig. 1.4a. The capacitive coupler was designed to be symmetrical, where each coupling plate is made of copper with overall dimensions of 30x250 mm. In addition, the capacitive coupler was constructed to be dynamic, such that the wireless medium can be simply varied to different misalignments. Zoom-in views on the capacitive coupler for aligned and fully-misaligned couplers are shown in Fig. 1.4b and c, respectively.

Both the transmitter and receiver consist of an L-type network, resonating in the vicinity of 4 MHz. The variable inductor was designed to vary between 1 and 4 μH, which translates to a frequency variation of 4–4.2 MHz. For biasing the variable inductor, TI's buck current regulator esd used [153]. Fig. 6.18a shows the custom-designed variable inductor which comprises an E-type EFD20-PC200 magnetic element. Fig. 6.18b shows the measured inductance as a function of the bias current up to 0.35 A, which is translated to 8X variation of inductance. The full-bridge inverter was realized with GaN power modules suitable for multi-MHz operation [103]. The overall nominal operating conditions and parameters of the experimental prototype are summarized in Table VI.

TABLE VI EXPERIMENTAL PROTOTYPE VALUES AND PARAMETERS

Parameter	***Value/Type***
Input voltage V_{in}	35-V
Transmitter's current peak-to-peak	2-A
Load resistance	100 Ω
Nominal output power	20 W
Nominal efficiency	83%
Coupling plates	30x250 mm, copper plates
Medium variation	20-200 mm
Full-bridge inverter	TI-LMG5200
Rectifier diodes	Vishay-VSSC520S-M3
Bias driver	TI-TPS92512DGQR
Inductors L_P and L_S	~45 μH
Variable inductor	1-4 μH
Capacitors C_P and C_S	35 pF
Operating frequency f_0	4-4.2 MHz

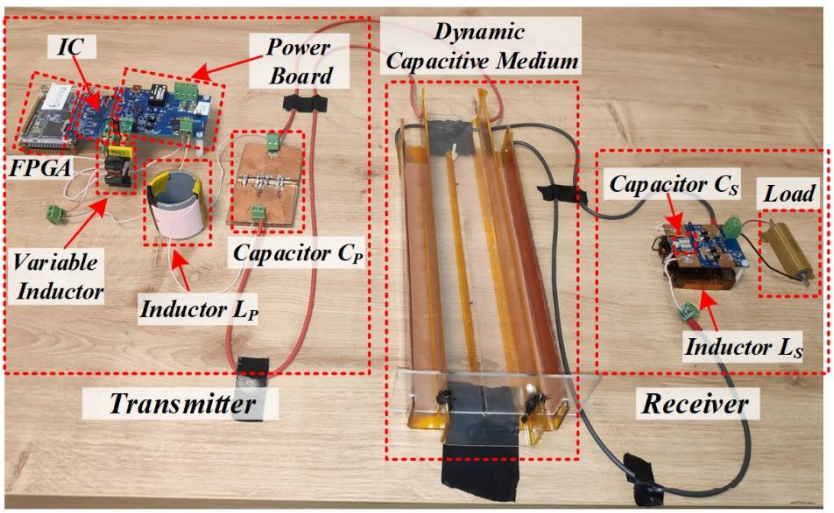

(a)

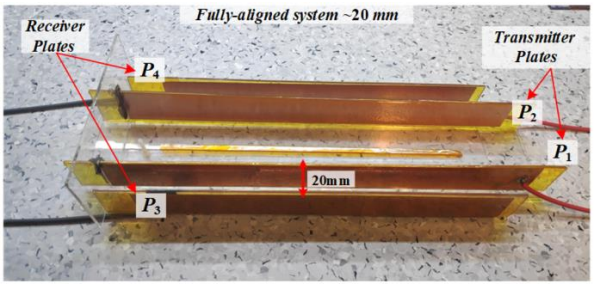

(b)

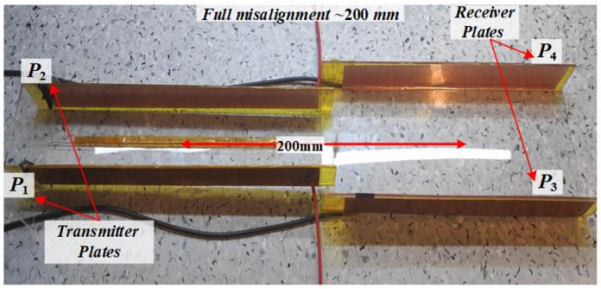

(c)

Fig. 6.17 Resonant capacitively-coupled WPT experimental system integrated with the controller IC board. (b) Zoom-in view of the capacitive-coupler for nominal orientation ~20 mm misalignment. (c) Zoom-in view on the capacitive-coupler for ~200 mm misalignment.

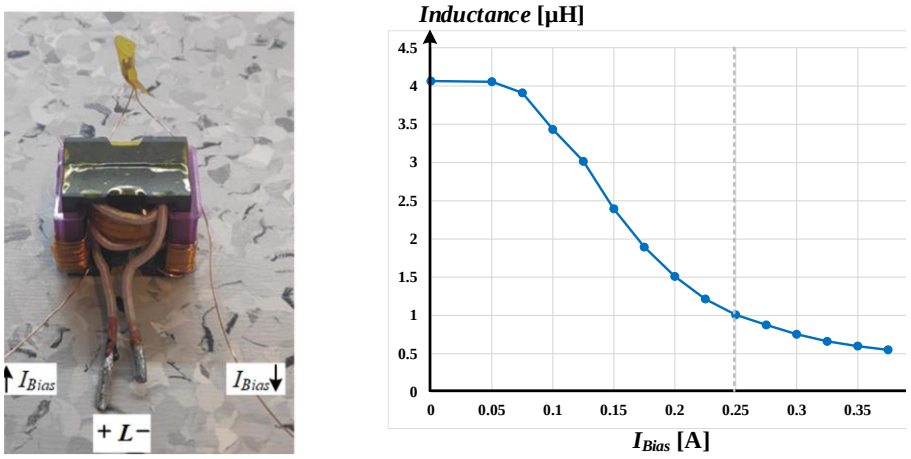

(a) (b)

Fig. 6.18 (a) Variable inductor. (b) Measured variable inductance as a function of the bias current.

Fig. 6.19 shows closed-loop steady-state measurements of the system, where the receiver and the transmitter are fully aligned. As can be seen, the input voltage fed to the transmitter's resonator toggles between 35 and -35 V, and the resonant current peaks at 1 A. To obtain soft-switching throughout the entire operating range and to compensate for phase offsets due to the voltage sensors, the phase reference for the phase detection was programmed to 115° (translated to a 25° phase difference between V_P and I_P), which results in operation slightly above the resonance. The average output current, $I_{out,AVG}$, on the receiver side is 0.45 A, which corresponds to an output power of 20-W with a peak efficiency of 83%. It should be emphasized that detailed analysis of ZVS operation was not a key objective in this study, and comprehensive soft-switching analysis for high-frequency amplifiers have previously been covered in the literature [133],[149],[150].

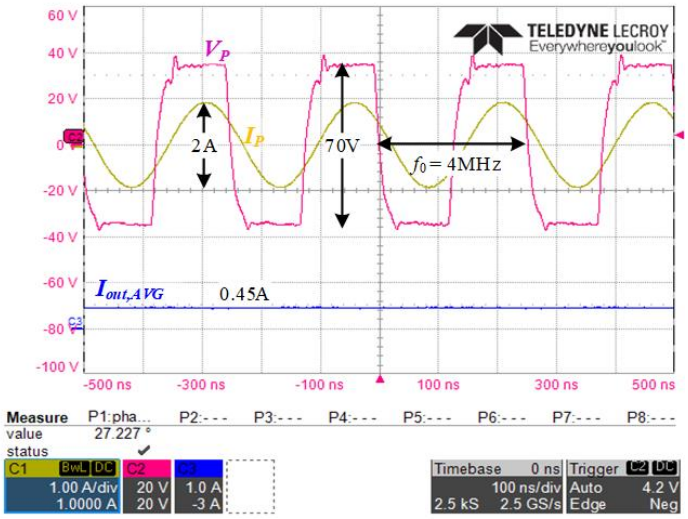

Fig. 6.19 Closed-loop operation waveforms at nominal conditions: V_{in}= 35 V, f_0=4 MHz, R_{Load}= 100 Ω, $I_{out,AVG}$ = 0.45 A. Voltage scale 20V/div, Current scale 1A/div; Time scale 100ns/div.

To further validate and demonstrate the effectiveness of the controller IC, the wireless system was tested for different medium variations, as depicted in Fig. 6.20. It can be noticed that the measured phase difference between the signals CMP_1 and CMP_2 over the entire medium range is 115°, as pre-defined for the phase detector. In addition, it can be observed that at full misalignment, the receiver's resonant current, I_S, decreases due to low coupling between the transmitter and receiver. On the other hand, the transmitter is kept at resonance over the entire variation range, where its resonant current, I_P, remains virtually at 1-A peak as targeted. The latter is accomplished by the adaptive tuning of the resonator inductance and self-frequency tracking mechanism, in which for the given set of measurements, it can be seen that the frequency increases as the misalignment increases. Main parameters and values for the various misalignment experiments are summarized in Table VII, including the coupling coefficient, k_C, and mutual coupling capacitance, C_M, per operating point.

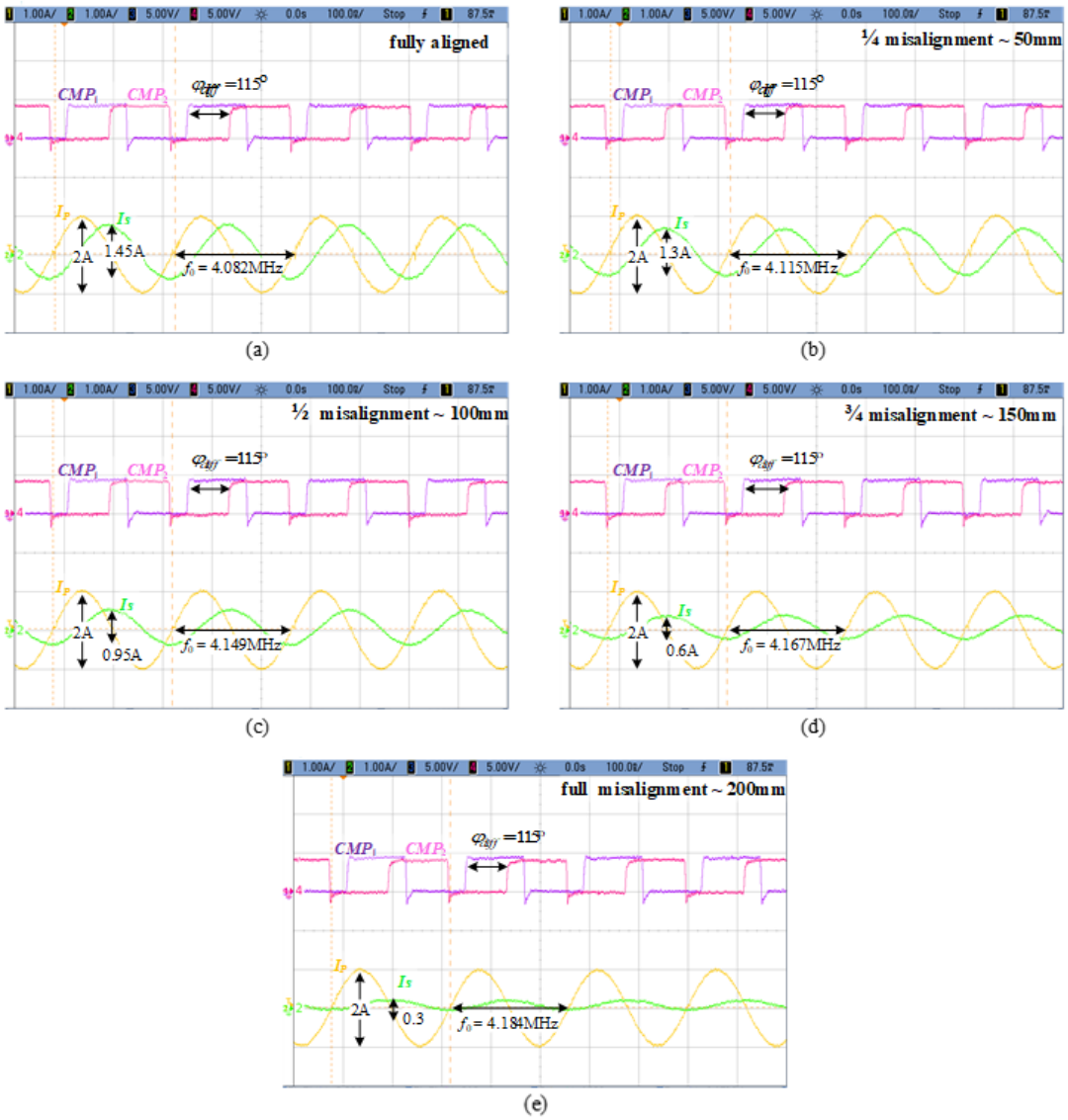

Fig. 6.20 Experimental measurements at closed-loop operation for different medium misalignments. Voltage scale 5V/div; Current scale 1A/div; Time scale 100ns/div.

TABLE VII SUMMARIZED PARAMETERS AND VALUES FOR MISALIGNMENT EXPERIMENTS

***Misalignment* [mm]**	***Kc***	***Cm* [pF]**	***IP* [A]**	***LP* [µH]**	***f0* [MHz]**	***Iout* [A]**
20	0.92	2.2	1.05	45	4	0.45
50	0.69	1.8	1.05	44.1	4.04	0.4
100	0.50	1.4	1.05	43.3	4.12	0.3
150	0.33	1	1.05	42.4	4.16	0.19
200	0.06	0.2	1.05	41.6	4.24	0.08

Fig. 6.21 shows dynamic responses of the WPT system to load changes. It can be seen that for 100 Ω to 50 Ω steps, the transmitter current, I_P, drops from 1 A peak and settles back to a steady-state condition after 2 ms, whereas the load current increases from 0.45 A to 0.6 A (Fig. 1.4a). On the other hand, for a 50 Ω to 100 Ω load change (Fig. 1.4b), the transmitter returns to a steady-state operation with target peak current of 1 A within ~4 ms, and the load current drops to 0.45 A. To further examine the dynamics of the controller, more extreme load steps were performed. Fig. 1.4c shows the measurements for a 100 Ω to 25 Ω load change. There, the average output current increased from 0.45 A to 0.85 – almost twice the nominal current. The transmitter current returns to 1 A within ~2.6 ms, whereas for the inverse load step, i.e., 25 Ω to 100 Ω (Fig. 1.4d), the transition lasts 3 ms. Fig. 6.22 depicts the transmitter's steady-state waveforms for a 0.85 A output current. To achieve better ZVS operation for the higher load steps, the phase reference for the phase detection was programmed to 125° (translated to a 35° phase difference between V_P and I_P). As can be observed, for various load steps, well-regulated responses are obtained with reasonable dynamics. It should be emphasized that by employing the controller IC concept also to the receiver side will enable more degrees of freedom on power regulation and spatial freedom, and can significantly improve overall end-to-end performance.

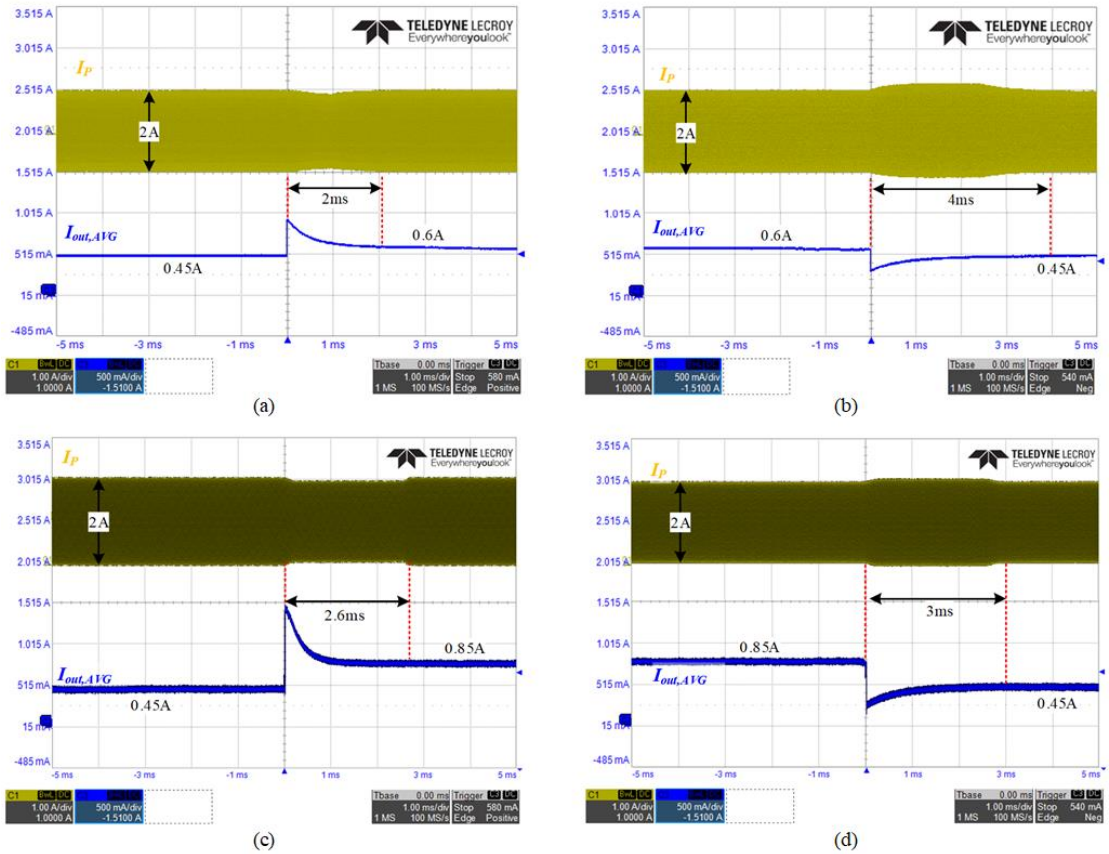

Fig. 6.21 Experimental waveforms for load changes: (a) Changing R_{Load} from 100 Ω to 50 Ω. (b) Changing R_{Load} from 50 Ω to 100 Ω. (c) Changing R_{Load} from 100 Ω to 25 Ω. (d) Changing R_{Load} from 25 Ω to 100 Ω. I_P (yellow trace) 1A/div, $I_{out,AVG}$ (blue trace) 0.5A/div; Time scale 1ms/div.

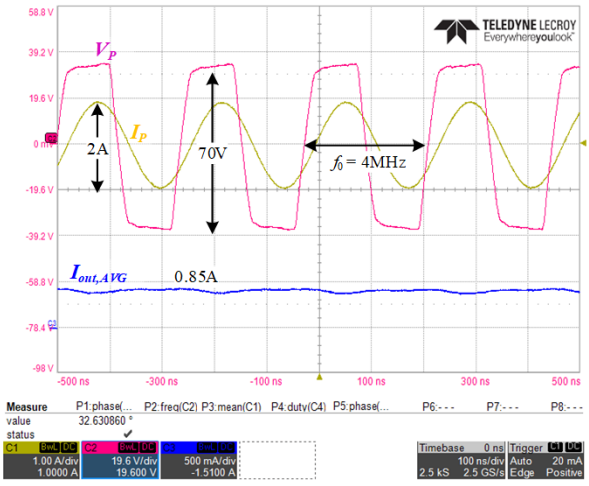

Fig. 6.22 Transmitter steady-state waveforms for 0.85 A average output current. V_P (pink trace) 20V/div, I_P (yellow trace) 1A/div, $I_{out,AVG}$ (blue trace) 0.5A/div; Time scale 100ns/div.

CHAPTER 7: Conclusion

Modeling approach of matching networks for resonant-operating capacitive wireless power transfer – A generic two-port network-based modeling approach for resonant capacitive wireless power transfer (WPT) systems has been presented. Based on the modeling approach, the behavior of resonant-operating capacitive power transfer (CPT) system (or in the vicinity of resonant operation) can be analyzed and described for different system variations such as capacitive coupling interface, resonant frequency and matching networks components. The modeling method provides an insight to the effects of the parameters on the system behavior, the cross-coupling relationships between transmitter and receiver sides, and source features based on the operation mode and settings. The simplicity and generality of the gyrator model as an energy transfer element offers an efficient closed-form alternative to complex analytical approaches or tedious numerical simulations. The presented behavioral model establishes the foundations for overall closed-loop analysis and controller design for capacitive WPT systems. This study also introduced a simulation-compatible variable capacitor model that is applicable for continuous-time analysis of WPT systems. This provides a simulation framework to account for variations of the capacitive medium such as coupling coefficient, dielectric material, alignment and distance between the coupling plates.

Capacitive-coupler modeling, analysis and simulation framework for wireless power transfer systems – Three different modeling approaches of the capacitive coupling in CPT systems: π-model, parallel (Norton), and series (Thevenin); have been overviewed, evaluated and compared. Applicability of the models to simulation platforms has been surveyed. The models have been devised applying a generic approach: first, treating the CC as a 2-port network; then, emulating the characteristic equations according to the circuit configurations.

The π-model is the simplest most intuitive approach. Its main drawback relies with the lack of flexibility to evaluate dynamic variations. It consists of three capacitors, where each of them must be modified for emulating misalignment and displacement of the system. This implies that for dynamic analysis of the system, these capacitors must be implemented by behavioral models, and potentially complicates the overall circuit. Thus, in the context of dynamic analysis the π-model is less attractive approach, however, it is a solid path for static analyses. The parallel (Norton) model is a straightforward representation of the 2-port network's equations. Nevertheless, its implementation is quite cumbersome since it involves time derivative function, that

limits the functionality of the model. This study further presented an alternative form of simulation-compatible Norton model for both time and frequency domains, however, at the cost of two additional capacitors that are represented by behavioral models. Unlike the two first models, series (Thevenin) modeling approach is applicable in its original form for time and frequency domain analyses, providing a generic simulation platform for static as well as dynamic observations of CPT system. This is since with this approach the mutual capacitance, Cm, can be determined by a simple behavioral source or 'constant' element, which can be varied on-the-fly.

Soft-switching analysis in capacitive wireless systems with *LCLC* compensation networks – Detailed soft-switching analysis of a *LCLC*-compensated resonant-based CPT systems has been presented. Based on the comprehensive analysis, it has been established that ZVS is achieved over the entire operating range if the system's parameters are designed for the highest expected coupling capacitor. It follows from the analysis presented in this study, that the current at turn off can be controlled for various operating conditions by altering the inductance of the primary compensation network. This way, sufficient energy to recharge the switches' body capacitances is obtained over the entire operating range further reducing the switching losses. This technique can be of a particular importance in high frequency *LCLC* WPT systems with very fast rise and fall times, where substantial current is required to recharge the capacitors rapidly. It is further shown that controlling the current at the switching instance by the method presented in this study does not affect the voltage gain ratio, therefore, the inductance can be controlled by means of an independent control loop, with no sensing of the output voltage, which significantly simplifies the overall WPT system. An excellent agreement has been found between the theoretical predictions, simulations and experimental results.

Multiloop control method for power regulation in capacitive wireless systems – An adaptive closed-loop mechanism for capacitive-based WPT systems has been detailed, analyzed, and experimentally validated. The controller comprises multiple control loops, which effectively disengages the power transfer capabilities of CPT systems from any drift or variations and further enables spatial freedom of the transferred energy from transmitter to the receiver. The control algorithm, signal flow, and the functional relationships of the multi-mixed-signal controller have been addressed, and all the intricate transfer functions of the key building blocks have been derived. Based on the analysis and intuitive guidelines in this study, the control loops

can be fully decoupled, and the multi-loop operation renders down to the first-order dynamics; thus, the overall electrical circuitries can be quite moderate in complexity (basic PLL, bias drive, few comparators, etc.).

This study also introduced a variable inductor realization that enables continuous self-tuned impedance matching. To demonstrate a closed-loop operation under system variations, an experiential resonant *LC* CPT prototype in the MHz range has been constructed, and with the core of the multi-loop controller has been implemented on an HDL platform. The resultant dynamic performance of the closed-loop CPT system is well validated through experiments up to air-gaps of 250 mm. The new controller concept establishes the foundations for better power delivery in many wireless power applications and may be found very beneficial in the rapidly growing field of capacitive wireless and other resonant-based wireless technologies.

Adaptive self-tuned mixed-signal controller IC for resonant wireless power transfer – An adaptive self-tuned high-performance controller IC for resonant-based WPT transmitters has been detailed, analyzed and experimentally validated. The IC comprises of two main independent control loops, which effectively disengage the power transfer capabilities of RWPT from medium variations and other potential drifts, and further enables spatial freedom. The control algorithm, signal flow and the mixed-signal controller IC architecture have been addressed. The controller has been designed and fabricated in 0.18 µm 5-V CMOS process with effective silicon area of 0.6 mm2. The digital core of the mixed-signal controller IC has been developed on the basis of all-digital standard-cell approach and can therefore be designed using a generic digital flow procedure. In the IC design, several main enabling key building blocks have been developed: DL-based phase detector, high-resolution DCO, and high-resolution DPWM. Post-layout analysis of the controller IC demonstrates high-performance self-tuned system. To further validate the controller, an experiential resonant capacitively-coupled WPT system in the MHz range has been designed and evaluated with the controller IC over various operating conditions. The resultant dynamic performance of the closed-loop system is well validated through experiments up to 200 mm misalignment. The new mixed-signal controller IC concept may be found very beneficial in many resonant-based wireless technologies, particularly in terms scalability and technology advancements.

Appendix-A

This appendix details the analytical derivations and observations required in Section 2.2, to extract the input-output characteristics of the matching networks that have been surveyed earlier. This provides a network perspective to the interaction between the source and load sides.

The relationship of the voltage and current of a series-parallel *LC* matching structure (Fig. 2.1a) can be expressed as

$$\begin{cases} V_{P1} = j\omega L_P I_{P1} + V_{P2} \\ V_{P2} = \dfrac{1}{j\omega C_P}\left(I_{P1} - I_{P2}\right) \end{cases} \Rightarrow \begin{cases} I_{P1} = \dfrac{\left(V_{P1} - V_{P2}\right)}{j\omega L_P} \\ V_{P1} = j\omega L_P I_{P1} + \dfrac{1}{j\omega C_P}\left(I_{P1} - I_{P2}\right) \end{cases}. \tag{1}$$

Assuming that the switching frequency equals the resonant frequency, the currents I_{p1} and I_{p2} are given by

$$\begin{cases} I_{P1} = -j\omega_0 C_P \left(V_{P1} - V_{P2}\right) \\ I_{P2} = -j\omega_0 C_P V_{P1} \end{cases} \quad ; \quad \omega_0 L_P = \frac{1}{\omega_0 C_P}, \tag{2}$$

where ω_0 is the resonant angular frequency.

By modifying the L-type network in Fig. 2.1a with additional series resonator, a T-type network (L_P-C_P-$L_P{}^*$) is obtained as shown in Fig. 2.1b. At the resonant frequency, this modification is effectively a short circuit, and the resulting T-type network has the characteristics of a gyrator as follows,

$$\begin{aligned} V_{P1} &= j\omega_0 L_P I_{P1} + \frac{1}{j\omega_0 C_P}\left(I_{P1} - I_{P2}\right) = \frac{1}{-j\omega_0 C_P} I_{P2} \\ V_{P2}{}^* &= -j\omega_0 L_P I_{P2} + \frac{1}{j\omega_0 C_P}\left(I_{P1} - I_{P2}\right) = \frac{1}{j\omega_0 C_P} I_{P1} \end{aligned}, \tag{3}$$

it should be noted that without losing generality, (3) can be expressed in a matrix representation as

$$\begin{bmatrix} I_{P1} \\ \\ I_{P2} \end{bmatrix} = \begin{bmatrix} 0 & \underbrace{j\omega_0 C_P}_{-G} \\ \underbrace{-j\omega_0 C_P}_{G} & 0 \end{bmatrix} \begin{bmatrix} V_{P1} \\ \\ V_{P2}{}^* \end{bmatrix}. \tag{4}$$

The current I_{P2} can also be expressed as

$$I_{P2} = j\omega_0 C_P \left(V_{P2}{}^* - V_{P2}\right). \tag{5}$$

Rearranging (4) and (5), and after some manipulations, the voltage $V_{P2}{}^*$ can be written as

$$V_{P2}^{*} = V_{P2} - V_{P1}, \tag{6}$$

substituting (6) into (4) results in the same value of the current I_{P1} as given in (2). This implies that the initial current-voltage relationships of the series-parallel LC matching network are preserved through a gyrator or two-port network representation. From the gyrator characteristics and under the constraint of operating at the resonant frequency, Fig. 2.1b can be further modified by reflecting the capacitor C_P^{*} to the first port as an inductor L_P^{*} as depicted in Fig. 2.1c. The original current-voltage relationships shown in (2) can be obtained by applying Kirchhoff's voltage and current laws. This yields

$$\begin{cases} V_{P2} = -j\omega_0 L_P I_{P2} + \dfrac{1}{j\omega_0 C_P}\left(I_{P1}^{*} - I_{P2}\right) \Rightarrow I_{P1}^{*} = j\omega_0 C_P V_{P2} \\ V_{P1} = j\omega_0 L_P I_{P1}^{*} + \dfrac{1}{j\omega_0 C_P}\left(I_{P1}^{*} - I_{P2}\right) \Rightarrow I_{P2} = -j\omega_0 C_P V_{P1} \\ I_{P1} = \dfrac{V_{P1}}{j\omega_0 L_P} + I_{P1}^{*} = -j\omega_0 C_P \left(V_{P1} - V_{P2}\right) \end{cases}. \tag{7}$$

Then, the series-parallel LC matching circuit in Fig. 2.1a can be simplified and represented equivalently with a two-port network by a gyrator element, whereas the transconductance gain is $G = -j\omega_0 C_P$, as shown in Fig. 2.1d.

In a similar manner to the series-parallel LC matching network, the voltage and current relationships of a parallel-series LC matching structure (Fig. 2.2a) are derived as

$$\begin{cases} V_{S1} = \dfrac{\left(I_{S1} - I_{S2}\right)}{j\omega C_S} \\ V_{S2} = V_{S1} - j\omega L_S I_{S2} \end{cases} \Rightarrow \begin{cases} I_{S2} = \dfrac{\left(V_{S1} - V_{S2}\right)}{j\omega L_S} \\ V_{S2} = \dfrac{\left(I_{S1} - I_{S2}\right)}{j\omega C_S} - j\omega L_S I_{S2} \end{cases}, \tag{8}$$

and when operating at the resonant frequency, the currents I_{S1} and I_{S2} are expressed as

$$\begin{cases} I_{S1} = j\omega_0 C_S V_{S2} \\ I_{S2} = -j\omega_0 C_S \left(V_{S1} - V_{S2}\right) \end{cases} ; \quad \omega_0 L_S = \frac{1}{\omega_0 C_S}. \tag{9}$$

The L-type network in Fig. 2.2a can be modified by adding a parallel resonator, whereas $L_S^{*} = L_S$ and $C_S^{*} = C_S$ (Fig. 2.2b). Similarly to the case of the series branch, the parallel resonator is effectively open circuit when operating at resonance and does not change the original characteristics of the circuit in Fig. 2.2a. By applying Kirchhoff's current law on the obtained π-type network (C_S-L_S-C_S^{*}), a two-port network with gyrator characteristics is obtained as follows

$$\begin{aligned} I_{S1} &= j\omega_0 C_S V_{S1} + \frac{(V_{S1} - V_{S2})}{j\omega L_S} = \underbrace{j\omega_0 C_S}_{-G} V_{S2} \\ I_{S2}{}^{*} &= -j\omega_0 C_S V_{S2} + \frac{(V_{S1} - V_{S2})}{j\omega_0 L_S} = \underbrace{-j\omega_0 C_S}_{G} V_{S1} \end{aligned}, \tag{10}$$

or in a matrix representation

$$\begin{bmatrix} I_{S1} \\ I_{S2}{}^{*} \end{bmatrix} = \begin{bmatrix} 0 & j\omega_0 C_S \\ -j\omega_0 C_S & 0 \end{bmatrix} \begin{bmatrix} V_{S1} \\ V_{S2} \end{bmatrix}. \tag{11}$$

The current I_{S2} can be obtained with the aid of $I_{S2}{}^{*}$ from (10) as follows

$$I_{S2} = I_{S2}{}^{*} - \frac{V_{S2}}{j\omega L_S} = -j\omega_0 C_S V_{S1} + j\omega_0 C_S V_{S2} = -j\omega_0 C_S (V_{S1} - V_{S2}). \tag{12}$$

From (10) and (12) it can be observed that the original current-voltage relationships of the parallel-series *LC* matching network are preserved while using a gyrator element. The latter implies that the circuit in Fig. 2.2a can be simply transformed to the circuit in Fig. 2.2c.

The *LCL* π-type network (shown in Fig. 2.3a) can also be analyzed and represented by a two-port model. In resonant operation the input and output currents can be obtained similarly to the analysis of the *CLC* π-type network as given in (10), which can be expressed as follows:

$$\begin{aligned} I_{S1} &= \frac{V_{S1}}{j\omega_0 L_S} + (V_{S1} - V_{S2})\, j\omega_0 C_S = \underbrace{-j\omega_0 C_S}_{-G} V_{S2} \\ I_{S2} &= -\frac{V_{S2}}{j\omega_0 L_S} + (V_{S1} - V_{S2})\, j\omega_0 C_S = \underbrace{j\omega_0 C_S}_{G} V_{S1} \end{aligned}, \tag{13}$$

and in a matrix representation describing Fig. 2.3b as

$$\begin{bmatrix} I_{S1} \\ I_{S2} \end{bmatrix} = \begin{bmatrix} 0 & -j\omega_0 C_S \\ j\omega_0 C_S & 0 \end{bmatrix} \begin{bmatrix} V_{S1} \\ V_{S2} \end{bmatrix}. \tag{14}$$

References

[1] E. Abramov, J. M. Alonso, and M. M. Peretz, “Analysis and behavioural modelling of matching networks for resonant-operating capacitive wireless power transfer,” in *IET Power Electronics*, vol. 12, no. 10, pp. 2615-2625, Aug. 2019.

[2] E. Abramov, I. Zeltser, and M. M. Peretz, “A network-based approach for modeling resonant capacitive wireless power transfer systems,” *CPSS IEEE Trans. on Power Electronics and Applications*, vol. 4, no. 1, pp. 19-28, March 2019.

[3] E. Abramov and M. M. Peretz, “Multi-loop control for power transfer regulation in capacitive wireless systems by means of variable matching networks,” *IEEE Journal on Emerging and Selected Topics in Power Electronics*, vol. 8, no. 3, pp. 2095-2110, Sept. 2020.

[4] E. Abramov and M. M. Peretz, “Adaptive self-tuned controller IC for resonant-based wireless power transfer transmitters,” in *IEEE Transactions on Power Electronics (TPEL)*, vol. 36, no. 11, pp. 12413-12431, Nov. 2021.

[5] E. Abramov and M. M. Peretz, “Modeling and analysis of capacitive wireless power transfer systems: a network approach”, in *proceedings IEEE International Power Electronics and Application Conference and Exposition (PEAC)*, Nov. 2018, pp. 1-6.

[6] E. Abramov, I. Zeltser, and M. M. Peretz, “Behavioral modeling of resonant power transfer systems with capacitive coupling: two-port network approach,” in *Proc. IEEE Applied Power Electronics Conf. (APEC) 2019*, March 2019, pp. 3129-3136.

[7] E. Abramov, I. Zeltser, and M. M. Peretz, “Simulation-compatible capacitive-coupler modeling and analysis for wireless power transfer applications,” in *Proc. IEEE Applied Power Electronics Conf. (APEC) 2022* – submitted.

[8] E. Abramov, I. Zeltser, and M. M. Peretz, “Soft-Switching in capacitive-coupled wireless power transfer with LCLC compensation networks,” in *Proc. IEEE Applied Power Electronics Conf. (APEC) 2020*, March 2020, pp. 3151-3158.

[9] E. Abramov, A. Mindel, and M. M. Peretz, “Regulated power transfer using self-tuned networks for capacitive wireless systems,” in *Proc. IEEE Applied Power Electronics Conf. (APEC) 2019*, March 2019, pp. 3092-3099.

[10] E. Abramov and M. M. Peretz, “Adaptive Self-Tuned Mixed-Signal Controller IC for Resonant Wireless Power Transfer,” in *Proc. IEEE Applied Power Electronics Conf. (APEC) 2020*, March 2020, pp. 805-812.

[11] T. Urkin, E. Abramov, and Mor. M. Peretz “Enhanced Performance Fully-Synthesizable ΣΔ ADC for Efficient Digital Voltage-Mode Control", *IEEE Workshop on Control and Modelling for Power Electronics (COMPEL) 2018*, pp. 1-8, 2018.

[12] Tesla, “The transmission of electrical energy without wires as a means for furthering peace,” *Elect. World Eng.*, pp. 21–24, Jan. 1905.

[13] T. Imura and Y. Hori, “Maximizing air gap and efficiency of magnetic resonant coupling for wireless power transfer using equivalent circuit and Neumann formula,” *IEEE Trans. Ind. Electron*., vol. 58, no. 10, pp. 4746–4752, Oct. 2011.

[14] J. Sallan, J. L. Villa, A. Llombart, and J. F. Sanz, “Optimal design of ICPT systems applied to electric vehicle battery charge,” *IEEE Trans. Ind. Electron*., vol. 56, no. 6, pp. 2140–2149, Jun. 2009.

[15] D. Yin, S. Oh, and Y. Hori, “A novel traction control for EV based on maximum transmissible torque estimation,” *IEEE Trans. Ind. Electron*., vol. 56, no. 6, pp. 2086–2094, Jun. 2009.

[16] C.-S. Wang, O. H. Stielau, and G. A. Covic, “Design considerations for a contactless electric vehicle battery charger,” *IEEE Trans. Ind. Electron*., vol. 52, no. 5, pp. 1308–1314, Oct. 2005.

[17] Y. Kamiya, T. Nakamura, T. Sato, J. Kusaka, Y. Daisho, S. Takahashi, and K. Narusawa, “Development and performance evaluation of advanced electric micro bus equipped with non-contact inductive rapid-charging system,” in *Proc. 23rd Int. EVS, Elect./Hybrid-Elect. Session*, Dec. 2007, pp. 1–14.

[18] L. Mostefai, M. Denai, O. Sehoon, and Y. Hori, “Optimal control design for robust fuzzy friction compensation in a robot joint,” *IEEE Trans. Ind. Electron*., vol. 56, no. 10, pp. 3832–3839, Oct. 2009.

[19] D. Xu, L. Han, M. Tan, and Y. F. Li, “Ceiling-based visual positioning for an indoor mobile robot with monocular vision,” *IEEE Trans. Ind. Electron*., vol. 56, no. 5, pp. 1617–1628, May 2009.

[20] Z. Bingyi, L. Hongbin, Z. Yisong, Y. Yong, and F. Guihong, “Contactless electrical energy transmission system using separable transformer,” in *Proc. 8th Int. Conf. Elect. Mach. Syst*., 2005, vol. 3, pp. 1721–1724.

[21] S. Li and C. Mi, “Wireless Power Transfer for Electric Vehicle Applications,” *IEEE Journal of Emerging and Selected Topics in Power Electronics*, vol. PP, pp. 1-1, 2014.

[22] S. Jaegue et al., "Design and implementation of shaped magnetic resonance-based wireless power transfer system for roadway-powered moving electric vehicles," *IEEE Trans. Ind. Electron*., vol. 61, no. 3, pp. 1179–1192, Mar. 2014.

[23] X. Lu, P. Wang, D. Niyato, D. I. Kim, and Z. Han, "Wireless charging technologies: Fundamentals, standards, and network applications," *IEEE Commun. Surveys Tuts*., vol. 18, no. 2, pp. 1413–1452, 2nd Quart., 2016.

[24] B. L. Cannon, J. F. Hoburg, D. D. Stancil, and S. C. Goldstein, "Magnetic resonant coupling as a potential means for wireless power transfer to multiple small receivers," *IEEE Transactions on Power Electronics*, vol. 24, no. 7, pp. 1819–1825, July 2009.

[25] S. Y. R. Hui, "Wireless power transfer: A brief review & update," *in Power Electronics Systems and Applications (PESA)*, 2013 5th International Conference on, Dec 2013, pp. 1–4.

[26] M. P. Kazmierkowski and A. J. Moradewicz, "Unplugged but connected: Review of contactless energy transfer systems," *IEEE Industrial Electronics Magazine*, vol. 6, no. 4, pp. 47–55, Dec 2012.

[27] Lukic and Z. Pantic, "Cutting the cord: Static and dynamic inductive wireless charging of electric vehicles," *IEEE Electrification Magazine*, vol. 1, no. 1, pp. 57–64, Sept 2013.

[28] J. G. Bolger, L. S. Ng, D. B. Turner, and R. I. Wallace, "Testing a prototype inductive power coupling for an electric highway system," in *Vehicular Technology Conference, 1979. 29th IEEE*, vol. 29, March 1979, pp. 48–56.

[29] C. E. Zell and J. G. Bolger, "Development of an engineering prototype of a roadway powered electric transit vehicle system: A public/private sector program," in *Vehicular Technology Conference, 1982. 32nd IEEE*, vol. 32, May 1982, pp. 435– 438.

[30] S. Y. R. Hui and W. C. Ho, "A new generation of universal contactless battery charging platform for portable consumer electronic equipment," in *Power Electronics Specialists Conference, 2004. PESC 04. 2004 IEEE 35th Annual*, vol. 1, June 2004, pp. 638–644 Vol.1.

[31] S. Y. R. Hui, W. Zhong, and C. K. Lee, "A critical review of recent progress in midrange wireless power transfer," *IEEE Transactions on Power Electronics*, vol. 29, no. 9, pp. 4500–4511, Sept 2014.

[32] M. P. Theodoridis, "Effective capacitive power transfer," *IEEE Trans. Power Electron*., vol. 27, no. 12, pp. 4906–4913, Dec. 2012.

[33] J. Kim et al., "Coil design and shielding methods for a magnetic resonant wireless power transfer system," *Proc. IEEE*, vol. 101, no. 6, pp. 1332–1342, Jun. 2013.

[34] Waffenschmidt, E.: 'Inductive wireless power transmission'. *Technical Educational Seminar, IEEE Energy Conversion Congress & Exposition*, 2011, pp. 1–128.

[35] F. Musavi and W. Eberle, "Overview of wireless power transfer technologies for electric vehicle battery charging," *IET Power Electron*., vol. 7, no. 1, pp. 60–66, Jan. 2014.

[36] F. Lu, H. Zhang, C. Mi, "A two-plate capacitive wireless power transfer system for electric vehicle charging Applications," *IEEE Trans. Power Electron*, vol. 33, no. 2, pp. 946-969, Aug. 2017.

[37] F. Lu, H. Zhang, H. Hofmann, and C. Mi, "A double-sided LC compensation circuit for loosely-coupled capacitive power transfer," *IEEE Trans. Power Electron*., vol. 33, no. 2, pp. 1633 – 1643, Feb. 2017.

[38] A. Kurs, A. Karalis, R. Moffat, J. D. Joannopoulos, P. Fisher, and M. Soljacic, "Wireless power transfer via strongly coupled magnetic resonances," *Science*, vol. 317, no. 5834, pp. 83-86, July 2007

[39] S. Li, W. Li, J. Deng, and C. C. Mi, "A double-sided LCC compensation network and its tuning method for wireless power transfer," *IEEE Trans. Veh. Technol*., vol. 64, no. 6, pp. 1–12, Jun. 2015.

[40] L. Cheng, W.-H. Ki, and C.-Y. Tsui, "A 6.78-MHz single-stage wireless power receiver using a 3-mode reconfigurable resonant regulating rectifier," *IEEE J. Solid-State Circuits*, vol. 52, no. 5, pp. 1412–1423, May 2017.

[41] H. G. Park et al., "A design of a wireless power receiving unit with a high-efficiency 6.78-MHz active rectifier using shared DLLs for magnetic-resonant A4 WP applications," *IEEE Trans. Power Electron*., vol. 31, no. 6, pp. 4484–4498, Jun. 2016.

[42] K.-G. Moh, F. Neri, S. Moon, P. Yeon, J. Yu, Y. Cheon, Y.-S. Roh, M. Ko, and B.-H. Park, "A fully integrated 6W wireless power receiver operating at 6.78 MHz with magnetic resonance coupling," in *Proc. ISSCC*, 2015, pp. 230–232.

[43] J. Shin et al., "Design and implementation of shaped magnetic-resonance-based wireless power transfer system for roadway-powered moving electric vehicles," *IEEE Trans. Ind. Electron*., vol. 61, no. 3, pp. 1179–1192, Mar. 2014.

[44] X. Qu et al., "Wide design range of constant output current using double-sided LC compensation circuits for inductive-power-transfer applications," *IEEE Trans. Power Electron*., vol. 34, no. 3, pp. 2364–2374, Mar. 2019.

[45] Y. Zhang, and M. A. de Rooij, "How eGaN® FETs are Enabling Large Area Wireless Power Transfer," *IEEE Workshop on Wide Bandgap Power Devices and Applications* (*WiPDA*), October 2017, pp 366 – 372.

[46] F. Lu, H. Zhang, H. Hofmann, and C. Mi, “A double-sided *LCLC* compensated capacitive power transfer system for electric vehicle charging,” *IEEE Trans. Power Electron.*, vol. 30, no. 11, pp. 6011–6014, Jun. 2015.

[47] H. Zhang, F. Lu, H. Hofmann, W. Liu, and C. C. Mi, “A four-plate compact capacitive coupler design and LCL-compensated topology for capacitive power transfer in electric vehicle charging application,” *IEEE Trans. Power Electron*., vol. 31, no. 12, pp. 8541–8551, Dec. 2016.

[48] F. Lu, H. Zhang, H. Hofmann, C. Mi, “A loosely coupled capacitive power transfer system with LC compensation circuit topology,” *Proc. IEEE Energy Convers. Congr. Expo. (ECCE)*, pp. 1-5, 2016.

[49] D. C. Ludois, J. K. Reed, and K. Hanson, “Capacitive power transfer for rotor field current in synchronous machines,” *IEEE Trans. Power Electron*., vol. 27, no. 11, pp. 4638–4645, Nov. 2012.

[50] D. C. Ludois, K. Hanson, and J. K. Reed, “Capacitive power transfer for slip ring replacement in wound field synchronous machines,” in *Proc. IEEE Energy Convers. Congr. Expo*., 2011, pp. 1664–1669.

[51] J. Zhu et al., "A novel capacitive coupler array with free-positioning feature for mobile tablet applications," in *IEEE Transactions on Power Electronics*, vol. 34, no. 7, pp. 6014-6019, July 2019.

[52] C. Liu, A.P. Hu, and M. Budhia, “A generalized coupling model for capacitive power transfer systems,” *Proc. 36th Annual Conf. on IEEE Ind. Electron. Society*, Glendale, AZ, pp.274–279, Nov. 2010.

[53] C. Liu, A. Hu, B. Wang, and N. C. Nair, “A capacitively coupled contactless matrix charging platform with soft switched transformer control,” in *IEEE Trans. Ind. Electron*., vol. 60, no. 1, pp. 249–260, Jan. 2013.

[54] B. Regensburger, J. Estrada, A. Kumar, S. Sinha, Z. Popović and K. K. Afridi, “High-performance capacitive wireless power transfer system for electric vehicle charging with enhanced coupling plate design,” 2018 *IEEE Energy Conversion Congress and Exposition (ECCE)*, Portland, OR, 2018, pp. 2472-2477.

[55] L. Huang, A. P. Hu, A. K. Swain, and Y. Su, “Accurate steady-state modeling of capacitive-coupling interface of capacitive power transfer systems with cross-coupling,” *Wireless Power Transfer*, vol. 3, no. 1, pp. 53–62, Mar. 2016.

[56] W. Zhou, Y. Su, L. Huang, X. Qing and A. P. Hu, “Wireless power transfer across a metal barrier by ccombined ccapacitive and inductive coupling,” in *IEEE Transactions on Industrial Electronics*, vol. 66, no. 5, pp. 4031-4041, May 2019.

[57] W. Zhang and C. Mi, “Compensation topologies for high power wireless power transfer systems,” *IEEE Transactions on Vehicular Technology*, vol. 65, no.6, pp. 4768-4778, july 2015.

[58] T. Duerbaum: First harmonic approximation including design constraints, *Telecommunications Energy Conference*, 1998. INTELEC. Pages: 321 – 328

[59] S. De Simone, C. Adragna, C. Spini, and G. Gattavari, “Design-oriented steady-state analysis of LLC resonant converters based on FHA,” in *Proc. Int. Symp. Power Electron., Electr. Drives, Autom. Motion (SPEEDAM)*, 2006, pp. 16–23.

[60] Y. Lim, H. Tang, S. Lim, J. Park, “An adaptive impedance-matching network based on a novel capacitor matrix for wireless power transfer,” *IEEE Transactions on Power Electronics*, vol. 29, no. 8, pp. 4403-4413, August 2014.

[61] T.C. Beh, M. Kato, T. Imura, S. Oh and Y. Hori, “Automated impedance matching system for robust wireless power transfer via magnetic resonance coupling,” *IEEE Transactions on Industrial Electronics*, vol. 60, no. 9, pp. 3689-3698, September 2013.

[62] S. Sinha, A. Kumar, S. Pervaiz, B. Regensburger and K.K. Afridi, “Design of efficient matching networks for capacitive wireless power transfer systems,” *Proceedings of the IEEE Workshop on Control and Modeling for Power Electronics (COMPEL)*, Trondheim, Norway, June 2016.

[63] A. Kumar, S. Sinha, A. Sepahvand, K. K. Afridi, “Improved design optimization for high-efficiency matching networks,” *IEEE Transactions on Power Electronics*, vol. 33, no. 1, pp. 37-50, Jan 2018.

[64] C. Lin and F. Lee, “Design of a piezoelectric transformer converter and its matching networks,” *Proc. IEEE-PESC’94 Conf.*, vol. 1, pp. 607–612, 1994.

[65] M. Evzelman and M.M Peretz “Optimal design of a class-E resonant driver,” *IET Power Electronics*, vol. 8, no.8, pp 1552-1557, Apr. 2015.

[66] F. Lu, H. Zhang, H. Hofmann, C. Mi, “An inductive and capacitive integrated coupler and its LCL compensation circuit design for wireless power transfer,” *IEEE Trans. Industry Applications*, vol. 53, no. 5, pp. 4903–4913, Oct. 2017.

[67] A. Witulski and R. W. Erickson, “Extension of state-space averaging to resonant switches and beyond,” *IEEE Trans. Power Electron.*, vol. 5, no. 1, pp. 98–109, Jan. 1990.

[68] H. Hao, G. A. Covic, and J. T. Boys, “An approximate dynamic model of LCL-T-based inductive power transfer power supplies,” *IEEE Trans. Power Electron*., vol. 29, no. 10, pp. 5554–5567, Oct. 2014.

[69] V. Vorperian, R. Tymerski, and F. C. Lee, “Equivalent circuit models for resonant and PWM switches,” *IEEE Trans. Power Electron*., vol. 4, no. 2, pp. 205–214, Apr. 1989.

[70] D. Maksimovic and S. Cuk, “A unified analysis of PWM converters in discontinuous modes,” *IEEE Trans. Power Electron*., vol. 6, no. 3, pp. 476–490, Jul. 1991.

[71] J. Lu, A. Kumar, K. K. Afridi, “A step-superposition based analysis approach to modeling resonant converters,” *IEEE Trans. Power Electron*., vol. 33, no. 8, pp. 7148-7165, Aug. 2018.

[72] C. J. Anderson and J. A. Lyle, “Technique for evaluating system performance using Q in numerical simulation exhibiting inter symbol interference,” *Electron. Lett*., vol. 30, pp. 71–72, 1994.

[73] L. Chen, S. Liu, Y. Zhou, and T. Cui, “An optimizable circuit structure for high-efficiency wireless power transfer*,” IEEE Trans. Ind. Electron.*, vol. 60, no. 1, pp. 339–349, Jan. 2013.

[74] B. Wang, W. Yerazunis, and K. H. Teo, “Wireless power transfer: Metamaterials and array of coupled resonators,” in *Proc. IEEE*, vol. 101, no. 6, pp. 1359–1368, Jun. 2013.

[75] A. Christ, M. G. Douglas, J. M. Roman, E. B. Cooper, A. P. Sample, B. H. Waters, et al., “Evaluation of wireless resonant power transfer systems with human electromagnetic exposure limits,” *IEEE Trans. Electromagn. Compat*., vol. 55, no. 2, pp. 265–274, Apr. 2013.

[76] Q. Yuan, Q. Chen, L. Li, and K. Sawaya, “Numerical analysis on transmission efficiency of evanescent resonant coupling wireless power transfer system,” *IEEE Trans. Antennas Propag*., vol. 58, no. 5, pp. 1751–1758, May 2010.

[77] S. Cheon, Y. H. Kim, S. Y. Kang, M. L. Lee, J. M. Lee, and T. Zyung, “Circuit-model-based analysis of a wireless energy-transfer system via coupled magnetic resonances,” *IEEE Trans. Ind. Electron*., vol. 58, no. 7, pp. 2906–2914, Jul. 2011.

[78] J. Dai and D.C Ludois, “A survey of wireless power transfer and a critical comparison of inductive and capacitive coupling for small gap applications,” *IEEE Trans. Power Electron*, vol. 30, no. 11, pp. 6017-6029, Nov. 2015.

[79] J. Huh, S. W. Lee, C. B. Park, G. H. Cho, and C. T. Rim, “High performance inductive power transfer system with narrow rail width for on-line electric vehicles,” in *Proc. IEEE Energy Convers. Congr. Expo*., 2010, pp. 647–651.

[80] C. T. Rim, “The difficult technologies in wireless power transfer,” *Trans. Korean Inst. Power Electron*., vol. 15, no. 6, pp. 32–39, Dec. 2010.

[81] J. Huh, S. W. Lee, W. Y. Lee, G. H. Cho, and C. T. Rim, “Narrow-width inductive power transfer system for on-line electrical vehicles (OLEV),” *IEEE Trans. Power Electron*., vol. 26, no. 12, pp. 3666–3679, Dec. 2011.

[82] B. Lee, M. Kiani, and M. Ghovanloo, “A triple-loop inductive power transmission system for biomedical applications,” *IEEE Trans. Biomed. Circuits Syst*, vol. 10, no. 1, pp. 138–148, Feb. 2016.

[83] K. Lu, S. K. Nguang, S. Ji, and L. Wei, “Design of auto frequency tuning capacitive power transfer system based on class-E 2 dc/dc converter*,” IET Power Electronics*, vol. 10, no. 12, pp. 1588-1595, 2017.

[84] M. Kline, I. Izyumin, B. Boser, and S. Sanders, ‘‘Capacitive power transfer for contactless charging,’’ in *Proc. IEEE Appl. Power Electron. Conf. Expo*., 2011, pp. 1398–1404.

[85] R. Tseng, B.V.Novak, S. Shevde, and K. A. Grajski, “Introduction to the Alliance for Wireless Power loosely-coupled wireless power transfer system specification version 1.0,” in *Proc. IEEE Wireless Power Transfer Conf*., Perugia, Italy, May 15–16, 2013, pp. 79–83.

[86] B. H.Waters, A. P. Sample, J. R. Smith, “Adaptive impedance matching for magnetically coupled resonators,” in *Proc. Prog. Electromagn. Res. Symp*., 2012, pp. 694–701.

[87] M. Pinuela, D. C Yates, S. Lucyszn, and P. D. Mitcheson, “Maximizing dc-to-load efficiency for inductive power transfer,” *IEEE Trans. Power Electron.*, vol. 28, no. 5, pp. 2437–2447, May 2013.

[88] S. Sinha, A. Kumar, K. K. Afridi, “Improved design optimization of efficient matching networks for capacitive wireless power transfer systems,” *in Proc. IEEE Appl. Power Electron. Conf. Expo. (APEC)*, Mar. 2018, pp. 3167–3173.

[89] J. Kim and J. Jeong, “Range-adaptive wireless power transfer using multiloop and tunable matching techniques,” *IEEE Trans. Ind. Electron*., vol. 62, no. 10, pp. 6233–6241, Oct. 2015.

[90] L. Cheng, W.-H. Ki, and C.-Y. Tsui, “A 6.78-MHz single-stage wireless power receiver using a 3-mode reconfigurable resonant regulating rectifier,” *IEEE J. Solid-State Circuits*, vol. 52, no. 5, pp. 1412–1423, May 2017.

[91] Y. Zhang, and M. A. de Rooij, “How eGaN® FETs are Enabling Large Area Wireless Power Transfer,” *IEEE Workshop on Wide Bandgap Power Devices and Applications* (*WiPDA*), October 2017, pp 366 – 372.

[92] E. S. Lee, J. Huh, X. V. Thai, S. Y. Choi, and C.-T. Rim, “Impedance transformers for compact and robust coupled magnetic resonance systems,” in *Proc. IEEE Energy Convers. Congr. Expo*. (*ECCE*), Sep. 2013, pp. 2239–2244.

[93] Z. Pantic and S. M. Lukic, “Framework and topology for active tuning of parallel compensated receivers in power transfer systems,” *IEEE Trans. Power Electron.*, vol. 27, no. 11, pp. 4503–4513, Nov. 2012.

[94] Z. Pantic, B. Sanzhong, and S. Lukic, "ZCS LCC-compensated resonant inverter for inductive-power-transfer application," *IEEE Trans. Ind. Electron.*, vol. 58, no. 9, pp. 3500–3510, Aug. 2011.

[95] Y. H. Sohn, B. H. Choi, G. H. Cho, and C. T. Rim, "Gyrator-based analysis of resonant circuits in inductive power transfer systems," *IEEE Transactions on Power Electronics*, vol. 31, no. 10, pp. 6824-6843, Oct. 2016.

[96] D. C. Hamill, "Lumped equivalent circuits of magnetic components: The gyrator–capacitor approach," *IEEE Trans. Power Electron.*, vol. 8, no. 2, pp. 97–103, Apr. 1993.

[97] S. Singer, "Loss-free gyrator realization," *IEEE Transactions on Circuits and Systems*, vol. 35, no. 1, pp. 26-34, Jan. 1988.

[98] S. Singer, "Gyrators application in power processing circuits," *IEEE Trans. Ind. Electron*., vol. IE-34, no. 3, pp. 313–318, Aug. 1987.

[99] R.L. Steigerwald, "A comparison of half-bridge resonant converter topologies," *IEEE Transactions on Power Electronics*, vol. 3, no. 2, pp. 174-182, April 1988.

[100] J.G. Hayes and M.G. Egan, "Rectifier-compensated fundamental mode approximation analysis of the series parallel LCLC family of resonant converters with capacitive output filter and voltage-source load," *Proceedings of the IEEE Power Electronics Specialists Conference (PESC)*, Charleston, SC, July 1999.

[101] S. Ben-Yaakov and M.M. Peretz, "Simulation bits: A SPICE behavioral model of non-linear inductors," *IEEE Power Electron. Soc.Newslett*., vol. 15, no. 4, pp. 9–10, 4th Quarter 2003.

[102] DE2 development and education board user manual, Altera Corporation, 2006.

[103] Texas Instrument: 'LMG5200 80-V, 10-A GaN Half-Bridge Power Stage' available at: http://www.ti.com/lit/ds/symlink/lmg5200.pdf, accessed March 2017.

[104] J. Craninckx and M. Steyaert, "A 1.8-GHz low-phase-noise CMOS VCO using optimized hollow spiral inductors," *IEEE J. Solid-State Circuits*, vol. 32, np. 5, pp. 736–744, May 1997.

[105] M. Bartoli, N. Noferi, A. Reatti, and M. Kazimierczuk, "Modeling litzwire winding losses in high-frequency power inductors," in *Proc. IEEE Power Electronics Specialists Conf.*, Jun. 23–27, 1996, pp. 1690–1696.

[106] J. Dai and D. C. Ludois, "Single active switch power electronics fork Kilowatt scale capacitive power transfer," in *IEEE Journal of Emerging and Selected Topics in Power Electronics*, vol. 3, no. 1, pp. 315-323, March 2015.

[107] A. Kumar, S. Pervaiz, Chieh-Kai Chang, S. Korhummel, Z. Popovic and K. K. Afridi, "Investigation of power transfer density enhancement in large air-gap capacitive wireless power transfer systems," *2015 IEEE Wireless Power Transfer Conference (WPTC)*, Boulder, CO, 2015, pp. 1-4.

[108] L. Huang and A. P. Hu, "Defining the mutual coupling of capacitive power transfer for wireless power transfer," in *Electronics Letters*, vol. 51, no. 22, pp. 1806-1807, 22 10 2015.

[109] I. Zeltser and S. Ben-Yaakov, "On SPICE simulation of voltage-dependent capacitors," in *IEEE Transactions on Power Electronics*, vol. 33, no. 5, pp. 3703-3710, May 2018.

[110] S. Ben-Yaakov and M. M. Peretz, "A self-adjusting sinusoidal power source suitable for driving capacitive loads," *IEEE Trans. Power Electron.*, vol. 21, no. 4, pp. 890–898, Jul. 2006.

[111] S. S. Ahsanuzzaman, T. McRae, M. M. Peretz, and A. Prodic, "Low volume buck converter with adaptive inductor core biasing," in *Proc. IEEE Appl. Power Electron. Conf. Expo. (APEC)*, Feb. 2012, pp. 335–339.

[112] O. Ezra and M. M. Peretz, "Magneto-electro-mechanical modeling of magnetic actuation systems," in *Proc. IEEE Applied Power Electronics Conference and Exposition (APEC)*, 2015, pp. 2628–2634.

[113] DE0-Nano Development and Education Board user manual, terasIC Inc. - Intel, 2016.

[114] H. Li, J. Li, K. Wang, W. Chen, and Y. Xu, "A maximum efficiency point tracking control scheme for wireless power transfer systems using magnetic resonant coupling," *IEEE Trans. Power Electron*., vol. 30, no. 7, pp. 3998–4008, Jul. 2015.

[115] P. Si, A. P. Hu, S. Malpas, D. Budgett, "A frequency control method for regulating wireless power to implantable devices," *IEEE Trans. on Biomedical Circuits and Systems*., vol. 2, no. 1, pp. 22– 29, March. 2008.

[116] T. D. Yeo, D. Kwon, S. T. Khang, and J. W. Yu, "Design of maximum efficiency tracking control scheme for closed-loop wireless power charging system employing series resonant tank," *IEEE Trans. Power Electron*., vol. 32, no. 1, pp. 471–478, Jan. 2017.

[117] Z. Zhang, H. Pang, A. Georgiadis, and C. Cecati, "Wireless power transfer—An overview," *IEEE Trans. Ind. Electron*., vol. 66, no. 2, pp. 1044–1058, Feb. 2019.

[118] D. Medini and S. Ben-Yaakov, "A current-controlled variable inductor for high frequency resonant power circuits," in *Proc. IEEE Appl. Power Electron. Conf*., Feb. 1994, pp. 219–225.

[119] K. Kalita, J. Handique, T. Bezboruah, "Modelling and behavioral simulation of a high-speed phase-locked loop for frequency synthesis," *IET Signal Processing*, vol. 6, no. 3, pp. 195–204, May 2012.

[120] E. Abramov, T. Vekslender, O. Kirshenboim, and M. M. Peretz, "Fully-integrated digital average current-mode control voltage regulator module IC," *IEEE Journal on Emerging and Selected Topics in Power Electronics,* vol. 6, no. 2, pp. 549-562, Jun. 2018.

[121] M. M. Peretz and S. Ben-Yaakov, "Digital control of resonant converters: resolution effects on limit cycles," *IEEE Trans. on Power Electronics*, vol.25, no.6, pp.1652-1661, 2010.

[122] S. R. Sanders, "On limit cycles and describing function method in periodically switched circuits," *IEEE Trans. Circuits Syst*., vol. 40, no. 9, pp. 564–572, Sep. 1993.

[123] H. Peng, A. Prodic, E. Alarcon, and D. Maksimovic, "Modeling of quantization effects in digitally controlled dc–dc converters," *IEEE Trans. Power Electron.*, vol. 22, no. 1, pp. 208–215, Jan. 2007

[124] M. M. Peretz and S. Ben-Yaakov, "Digital control of resonant converters: enhancing frequency resolution by dithering," in *Proc. IEEE Applied Power Electronics Conference and Exposition (APEC)*, Feb. 2009, pp. 1202-1207.

[125] C. Xiao, L. Zhao, T. Asada, W. G. Odendaal, and J. D. van Wyk, "An overview of integratable current sensor technologies," in *Proc. Conf. Rec. Ind. Appl*., 2003, vol. 2, pp. 1251–1258.

[126] H. P. Forghani-zadeh, G. A. Rincon-Mora, "Current-sensing techniques for DC–DC converters," in *Proc. IEEE Midwest Symposium. Circuits and Systems*, vol. 2, pp. 577–580, Aug 2002.

[127] E. Abramov, M. Evzelman, O. Kirshenboim. T. Urkin, and M. M, Peretz, "Low voltage sub-nanosecond pulsed current driver IC for high-resolution LIDAR applications," *in Proc. IEEE Appl. Power Electron. Conf. Expo. (APEC)*, Mar. 2018, pp. 708–715.

[128] IEEE Standard for Safety Levels with Respect to Human Exposure to Radio Frequency Electromagnetic Fields, 3kHz to 300 GHz, IEEE Standard C95.1, 2005.

[129] DE2 development and education board user manual, Altera Corporation, 2006.

[130] N. Y. Kim, K. Y. Kim, J. Choi, and C. W. Kim, "Adaptive frequency with power-level tracking system for efficient magnetic resonance wireless power transfer," *Electron. Lett*., vol. 48, no. 8, pp. 452–454, Apr. 2012.

[131] N. Y. Kim et al., "Automated adaptive frequency tracking system for efficient mid-range wireless power transfer via magnetic resonant coupling," in *Proc. 42nd Eur. Microw. Conf*., 2012, pp. 221–224.

[132] Y. Jiang et al. "Analysis, Design and implementation of WPT system for EV's battery charging based on optimal operation frequency range," in *IEEE Transactions on Power Electronics*, vol. 34, no. 7, pp. 6890–6905, July 2018.

[133] Y. Jiang, L. Wang, Y. Wang, J. Liu, X. Li, and G. Ning, "Analysis, design, and implementation of accurate ZVS angle control for EV battery charging in wireless high-power transfer," *IEEE Trans. Ind. Electron*., vol. 66, no. 5, pp. 4075–4085, May 2019.

[134] M. Rodriguez, Y. Zhang, and D. Maksimovic, "High-frequency PWM buck converters using GaN-on-SiC HEMTs," *IEEE Trans. Power Electron*., vol. 29, no. 5, pp. 2462–2473, May 2014.

[135] Y. Zhang, M. Rodriguez, and D. Maksimovic, "Very high frequency PWM buck converters using monolithic GaN half-bridge power stages with integrated gate drivers," *IEEE Trans. Power Electron*., vol. 31, no. 11, pp. 7926– 7942, Nov. 2016.

[136] Altera (2012, Sep.) Transciever Overview: Stratix IV and Hard-Copy IV. [Online]. Avialable: http://www.altera.com/devices/fpga/stratixfpgas/stratix-iv/transceiver s/stxiv-transceivers.html

[137] J. Kim and J. Jeong, "Range-adaptive wireless power transfer using multiloop and tuneable matching techniques," *IEEE Trans. Ind. Electron*., vol. 62, no. 10, pp. 6233–6241, Oct. 2015.

[138] B. J. Patella, A. Prodić, A. Zirger, and D. Maksimović, "High-frequency digital PWM controller IC for DC-DC converters," *IEEE Trans. Power Electron*., vol. 18, no. 1, pp. 438-446, Jan. 2003.

[139] O. Trescases, A. Prodić, Wai Tung Ng, "Digitally controlled current-Mode DC–DC converter IC," *IEEE Trans. Circuits Syst. I, Reg. Papers*, vol. 58, no. 1, pp. 219-231, Jan. 2011.

[140] R. K. Nandwana, T. Anand, S. Saxena, S. J. Kim, M. Talegaonkar, A. Elkholy, W. S. Choi, A. Elshazly, and P. K. Hanumolu, "A calibration free fractional-N ring PLL using hybrid phase/current-mode phase interpolation method," *IEEE J. Solid-State Circuits*, vol. 50, no. 4, pp. 882–895, Apr. 2015.

[141] Z. Cheng, X. Zheng, M. J. Deen, and H. Peng, "Recent developments and design challenges of high-performance ring oscillator CMOS timeto-digital converters," *IEEE Trans. Electron Devices*, vol. 63, no. 1, pp. 235–251, Jan. 2016

[142] H. Peng, A. Prodić, E. Alarcon, and D. Maksimović, "Modeling of quantization effects in digitally controlled dc–dc converters," *IEEE Trans. Power Electron*., vol. 22, no. 1, pp. 208–215, Jan. 2007.

[143] A. P. Dancy and A. P. Chandrakasan, "Ultra low power control circuits for PWM converters," in *Proc. IEEE Power Electron. Spec. Conf. (PESC)*, Jun. 1997, pp. 21–28.

[144] M. Hovin, A. Olsen, T. S. Lande, and C. Toumazou, "Delta-sigma modulators using frequency-modulated intermediate values", *IEEE Journal of Solid-State Circuits*, vol. 32, no. 1, pp. 13 – 22, Jan. 1997.

[145] A. V. Peterchev and S. R. Sanders, “Quantization resolution and limit cycling in digitally controlled PWM converters,” *IEEE Trans. Power Electron.*, vol. 18, no. 1, pp. 301–308, Jan. 2003.

[146] Z. Lukic, N. Rahman, and A. Prodic, “Multi-bit S-D PWM digital controller IC for DC-DC converters operating at switching frequencies beyond 10 MHz,” *IEEE Trans. Power Electron*., vol. 22, no. 5, pp. 1693–1707, Sep. 2012.

[147] J. M. de la Rosa, “Sigma-Delta modulators: tutorial overview, design guide, and state-of-the-art survey,” *IEEE Transcriptions on Circuits and Systems*, vol. 58, pp. 1-21, 2011.

[148] J. A. Abu-Qahouq, H. Mao, H. J. Al-Atrash, and I. Batarseh, “Maximum efficiency point tracking (MEPT) method and digital dead time control implementation,” *IEEE Trans. Power Electron*., vol. 21, no. 5, pp. 1273-1281, Sep. 2006.

[149] M. de Rooij, “The ZVS voltage-mode class-D amplifier, an eGaN FET enabled topology for highly resonant wireless energy transfer,” in *Proc. App. Power Electron. Conf. Expo*., Charlotte, NC, USA, 2015, pp. 1608–1613.

[150] H. Tebianian, J. Quaicoe, and B. Jeyasurya, “High frequency full-bridge class-D inverter using eGaN FET with dynamic dead-time control,” in *Proc. IEEE PELS Workshop Emerg. Technol.: Wireless Power (WoW)*, Knoxville, Tennessee, USA, 2016, pp. 95–99.

[151] A. M. Aibinu, M. J. E. Salami, A. A. Shafie, and A. R. Najeeb, ‘‘Comparing autoregressive moving average (ARMA) coefficients determination using artificial neural networks with other techniques,’’ *World Acad. Sci., Eng. Technol. J*., vol. 2, no. 6, pp. 157–162, 2008.

[152] T. Vekslender, E. Abramov, O. Kirshenboim and M. M. Peretz, "Hardware efficient digital auto-tuning average current-mode controller," *IEEE 18th Workshop on Control and Modeling for Power Electronics (COMPEL*), Stanford, CA, 2017, pp. 1-8.

[153] Texas Instrument: ‘TPS92512 2.5A Buck LED Driver with Integrated Analog Current Adjust’ available at: https://www.ti.com/lit/gpn/tps92512.pdf, accessed February 2015.

(page intentionally left blank)

Abstract (Hebrew) תקציר

בעשור האחרון, המחקר והפיתוח בטכנולוגיית העברת הספק אלחוטית מקבלים תאוצה משמעותית מאוד הן באקדמיה והן בתעשייה, דבר אשר עזר לקדם ולמנף את טכנולוגיות האנרגיה האלחוטית במגוון תחומים ממילי-וואטים ועד לקילו-וואטים: מכשירים ביו-רפואיים, IoT, אלקטרוניקה נישאת, רכבים חשמליים ועוד. העברת הספק אלחוטית זה הגורם העיקרי אשר יאפשר "להפטר" מהכבל האחרון, ובנוסף, למזער את התלות של מכשירם נישאים בסוללות מסורבלות כמקור האנרגיה העיקרי.

בהקשר של שיטות אנרגיה אלחוטית לטווחים קרובים, השיטות הנפוצות יותר הין שיטות אשר מבוססות על תכונות מגנטיות של התווך כמו inductive power transfer (IPT) ו- magnetic resonance. אלמנטי הצימוד בשיטות אלה הינם סלילים (שנאים מבוזרים). IPT היא השיטה בנפוצה יותר בתעשייה כיום, בשל הפשטות שלה, אמינות ובטיחות. מספר מחקרים ואפליקציות מעשיות הדגימו את היכולות של השיטה הזו בהספקם של כמה קילו-וואטים עבור אפליקציות סטטיות. באופן כללי, על מנת לרכז את השדה המגנטי הנוצר מהסליל המשדר, יש צורך בחומרים פרומגנטיים שיוצרים את ליבת הסליל. המבנה הכולל הופך את אלמנטי הצימוד להיות גדולים, כבדים ומסורבלים. בנוסף, חומרים פרומגנטיים רגישים לרעידות, חשיפה ממושכת עלולה ליצור מפגעים בחומר, ולפגוע ביכולתו לרכז את השדה המגנטי. תופעה בלתי רצויה נוספת של השימוש בשדה מגנטי הם זרמי מערבולת הנוצרים בברזל שנקלע לשדה המגנטי. תופעה זו מביאה להפסדי הספק משמעותיים, כאשר שאריות ברזל מוצאים את דרכם אל קירבת אלמנטי הצימוד. כמו כן, התווך רגיש מאוד למיקום עצמים ויכולת העברת ההספק תלויה בצורה חריפה בכך שהתווך נקי מחסמים.

חלופה הולמת לשיטות המבוססות על שדות מגנטיים, היא העברת אנרגיה בתהודה של המערכת באמצעות שדה חשמליים בתדרים גבוהים . גישה זו מתבססת על אלמנטי צימוד שהם למעשה מהווים לוחות קבל. שדה חשמלי אינו "סובל" מתופעת זרמי מערבולת, והאלמנטים המצמדים הינם לוחות מוליכים פשוטים. המאפיינים האלה מאפשרים להקטין באופן משמעותי נפח, משקל, ועלות של האלמנטים המצמדים. קיימים בפיתוח, בעיקר במסגרת האקדמיה, מספר פתרונות המבוססים על העברת הספק בעזרת שדה חשמלי. הודגמה העברת הספק עם אופי קיבולי ביישום סטטי וברמה של מספר קילוואטים למטרת טעינה של רכב חשמלי. בניסיונות אלה ניתן לראות צעד חשוב בכיוון העברת הספק בקרבת עצמים מתכתיים ללא עירור של זרמי מערבולת.

הבעיה העיקרית של מערכות אנרגיה אלחוטית, היא ירידה דרסטית בהעברת ההספק (כמות ונצילות העברה) בגין סטייה מהמיקום ואוריינטציה של המשדר והמקלט. בנוסף, מקם הצימוד של התווך ותנאי תנאי העברת האנרגיה, מאוד רגישים לשינויים בסביבה, בלאי של רכיבים, סטיות טמפרטורה, שפוגעים באיכות ויכולת העברת ההספק. האתגרים הללו מקשים על טכנולוגית אנרגיה אלחוטית לעשות את קפיצת המדרגה לעבר הטמעה באפליקציות דינאמיות (נמצאות בתנועה ועדיין מקבלות אנרגיה אלחוטית).

מטרת מחקר זה היא לחקור ולפתח פלטפורמה לניתוח עבור מערכות קיבוליות, כך שניתן יהיה לאפיין את התנהגות המערכות הקיבוליות תוך התחשבות בתווך, תדר התהודה והרכיבים הראקטיביים. ידע זה מתורגם לקווים מנחים לתכנון ומימוש של בקרים מתוחכמים בעלי מספר חוגים של פיצוי עבור מערכות קיבוליות להעברת אנרגיה אלחוטית. מטרה נוספת של מחקר זה, היא תכנון, פיתוח ומימוש של בקר בעל ביצועים גבוהים על גבי שבב עבור מערכות העברה אנרגיה אלחוטית תהודתיות.

תוצאות המחקר ל PhD מסכמות תרומה אקדמית של ארבעה מאמרי עיתון [4]-[1] אשר פורסמו ב- IEEE Transactions on Power Electronics (TPEL) וב- Journal of Emerging Selected Topics in Power Electronics (JESTPE) ו-IET Power Electronics; שבעה מאמרים נוספים בכנסים מובילים בתחום [5]-[11] אשר הוצגו ב- IEEE Applied Power Electronics Conference (APEC), וב- Control and Modeling for Power Electronics (COMPEL).

מילות מפתח – מודלים התנהגותיים, העברת אנרגיה אלחוטית, העברת אנרגיה מבוססת תווך קיבולי, בקרה עבור מערכות אנרגיה אלחוטיות, בקרה דיגיטלית.

העבודה נעשתה בהדרכת:

פרופ' מור מרדכי פרץ

המרכז לאלקטרוניקת הספק ומעגלים מוכללים – PEMIC

במחלקה להנדסת חשמל ומחשבים

הפקולטה להנדסה

הצהרת תלמיד המחקר עם הגשת עבודת הדוקטור לשיפוט

אני החתום מטה מצהיר/ה בזאת: (אנא סמן):

_✓_ חיברתי את חיבורי בעצמי, להוציא עזרת ההדרכה שקיבלתי מאת מנחה/ים.

_✓_ החומר המדעי הנכלל בעבודה זו הינו פרי מחקרי מתקופת היותי תלמיד/ת מחקר.

___ בעבודה נכלל חומר מחקרי שהוא פרי שיתוף עם אחרים, למעט עזרה טכנית הנהוגה בעבודה ניסיונית. לפי כך מצורפת בזאת הצהרה על תרומתי ותרומת שותפי למחקר, שאושרה על ידם ומוגשת בהסכמתם.

תאריך 15.08.21 שם התלמיד/ה אלי ולרי אברמוב חתימה _____

מידול ובקרה של מערכות להעברת אנרגיה אלחוטית מבוססות תווך קיבולי

מחקר לשם מילוי חלקי של הדרישות לקבלת תואר "דוקטור לפילוסופיה"

מאת

אלי ולרי אברמוב

הוגש לסינאט אוניברסיטת בן גוריון בנגב

אישור המנחה: פרופ' מור מרדכי פרץ

אישור דיקן בית הספר ללימודי מחקר מתקדמים ע"ש קרייטמן: פרופ' דודי בר-צבי _____

ז' באלול התשפ"א **15.08.2021**

באר-שבע

מידול ובקרה של מערכות להעברת אנרגיה אלחוטית מבוססות תווך קיבולי

מחקר לשם מילוי חלקי של הדרישות לקבלת תואר "דוקטור לפילוסופיה"

מאת

אלי ולרי אברמוב

הוגש לסינאט אוניברסיטת בן גוריון בנגב

ז' באלול התשפ"א **15.08.2021**

באר-שבע